

COSMOGLOBE DR1 results. I. Improved *Wilkinson Microwave Anisotropy Probe* maps through Bayesian end-to-end analysis

D. J. Watts^{1*}, A. Basurov¹, J. R. Eskilt^{1,2}, M. Galloway¹, L. T. Hergt³, D. Herman¹, H. T. Ihle¹, S. Paradiso⁴, F. Rahman⁵, H. Thommesen¹, R. Aurién¹, M. Bersanelli⁶, L. A. Bianchi⁶, M. Brilenkov¹, L. P. L. Colombo⁶, H. K. Eriksen¹, C. Franceschet⁶, U. Fuskeland¹, E. Gjerløw¹, B. Hensley⁸, G. A. Hoerning⁷, K. Lee¹, J. G. S. Lunde¹, A. Marins^{7,9}, S. K. Nerval^{10,11}, S. K. Patel¹², M. Regnier¹³, M. San¹, S. Sanyal¹², N.-O. Stutzer¹, A. Verma¹², I. K. Wehus¹, and Y. Zhou¹⁴

¹ Institute of Theoretical Astrophysics, University of Oslo, Blindern, Oslo, Norway

² Imperial Centre for Inference and Cosmology, Department of Physics, Imperial College London, Blackett Laboratory, Prince Consort Road, London SW7 2AZ, United Kingdom

³ Department of Physics and Astronomy, University of British Columbia, 6224 Agricultural Road, Vancouver BC, V6T1Z1, Canada

⁴ Waterloo Centre for Astrophysics, University of Waterloo, Waterloo, ON N2L 3G1, Canada

⁵ Indian Institute of Astrophysics, Koramangala II Block, Bangalore, 560034, India

⁶ Dipartimento di Fisica, Università degli Studi di Milano, Via Celoria, 16, Milano, Italy

⁷ Instituto de Física, Universidade de São Paulo - C.P. 66318, CEP: 05315-970, São Paulo, Brazil

⁸ Department of Astrophysical Sciences, Princeton University, 4 Ivy Lane, Princeton, NJ 08540

⁹ Department of Astronomy, University of Science and Technology of China, Hefei, China

¹⁰ David A. Dunlap Department of Astronomy & Astrophysics, University of Toronto, 50 St. George Street, Toronto, ON M5S 3H4, Canada

¹¹ Dunlap Institute for Astronomy & Astrophysics, University of Toronto, 50 St. George Street, Toronto, ON M5S 3H4, Canada

¹² Department of Physics, Indian Institute of Technology (BHU), Varanasi - 221005, India

¹³ Laboratoire Astroparticule et Cosmologie (APC), Université Paris-Cité, Paris, France

¹⁴ Department of Physics, University of California, Berkeley, Berkeley, CA 94720, USA

March 9, 2023

ABSTRACT

We present the first joint analysis of *WMAP* and *Planck* LFI time-ordered data, processed within the Bayesian end-to-end Commander framework. This framework builds directly on a similar analysis of the LFI measurements by the BEYONDPLANCK collaboration, and approaches the CMB analysis challenge through Gibbs sampling of a global posterior distribution. The computational cost of producing one complete *WMAP*+LFI Gibbs sample is 812 CPU-hr, including calibration, mapmaking, and component separation, of which 603 CPU-hr is spent on *WMAP* low-level processing; this demonstrates that end-to-end Bayesian analysis of the *WMAP* data is computationally feasible. We find that our *WMAP* posterior mean temperature sky maps are largely consistent with the official maps, and the resulting CMB power spectrum is in excellent agreement with previous results. The most notable difference is a slightly lower CMB quadrupole amplitude of $\sigma_2 = 133 \pm 70 \mu\text{K}^2$, as compared to $\sigma_2 = 229 \pm 97 \mu\text{K}^2$ in the BEYONDPLANCK analysis. In contrast, our *WMAP* polarization maps differ more notably from the official results, and in general they exhibit lower large-scale residuals, most likely attributable to a better constrained gain and transmission imbalance model; it is particularly noteworthy that our *W*-band sky maps appear statistically consistent with the *V*-band maps. For the first time, *WMAP*-minus-LFI frequency map differences appear visually consistent with instrumental noise over most of the sky. Still, we identify three specific issues that require additional work, namely 1) low-level noise modeling, 2) quadrupole residuals in the *V*- and *W*-band temperature maps at the $2 \mu\text{K}$ level; and 3) a strong degeneracy between the absolute *K*-band calibration and the dipole of the anomalous microwave emission component. Nevertheless, we believe that the reprocessed *WMAP* maps presented here are significantly cleaner in terms of systematic uncertainties than the official *WMAP* maps. Both sky maps and the associated code are made publicly available through the COSMOGLOBE web page.

Key words. ISM: general – Cosmology: observations, polarization, cosmic microwave background, diffuse radiation – Galaxy: general

Contents

1	Introduction	2	2.4 Sky model	6	
2	End-to-end Bayesian CMB analysis	3	2.5 Priors and poorly measured modes	6	
2.1	LFI and BEYONDPLANCK	3	2.6 Posterior distribution and Gibbs sampling	8	
2.2	Official <i>WMAP</i> instrument model and analysis pipeline	3	2.7 Sampling algorithms	8	
2.3	COSMOGLOBE instrument model	4	2.7.1 Review of sampling algorithms	8	
			2.7.2 Differential mapmaking	9	
			2.7.3 Transmission imbalance estimation	10	
			2.7.4 Baseline sampling	10	
			3	Data and data processing	10
			3.1	Publicly available <i>WMAP</i> products	10

* Corresponding author: D. J. Watts; duncanwa@astro.uio.no

3.2	TOD preprocessing and data selection	11
3.3	Computational resources and future plans	12
4	Instrumental parameters	
4.1	Markov chains, correlations and posterior mean statistics	13
4.2	Gain and baselines	14
4.3	Transmission imbalance	15
4.4	Instrumental noise	16
4.5	Instrumental corrections in map domain	19
4.6	Instrumental uncertainties in power spectrum domain	21
5	Frequency maps	
5.1	Map survey	21
5.2	Consistency tests through inter-channel difference maps	30
5.3	Efficiency of template-based transmission imbalance uncertainty propagation	33
6	Preliminary astrophysical results	
6.1	Galactic foregrounds	34
6.2	CMB results	37
6.2.1	Solar dipole	37
6.2.2	Angular temperature power spectrum	37
6.2.3	Low- ℓ anomalies	38
6.3	χ^2 and map space residuals	39
6.4	WMAP-versus-LFI signal-to-noise ratio comparison	39
7	Outstanding issues	
7.1	Noise modeling	39
7.2	V- and W-band quadrupole residual	41
7.3	Degeneracy between K-band calibration and AME dipole	42
7.4	Other minor effects	42
7.4.1	Time-variable bandpass modeling	42
7.4.2	Polarized sidelobe modeling	43
8	Conclusions	
A	Survey of instrumental parameters	
B	WMAP frequency map survey	

1. Introduction

The discovery of the cosmic microwave background (CMB) by Penzias & Wilson (1965) marked a paradigm shift in the field of cosmology, providing direct evidence that the Universe was once much hotter than it is today, effectively ruling out the steady-state theory of the universe (Dicke et al. 1965). This discovery spurred a series of ground-breaking cosmological experiments, including the Nobel Prize-winning measurements by COBE-FIRAS that confirmed the blackbody nature of the CMB (Mather et al. 1994) and COBE-DMR that measured temperature variations from the primordial gravitational field (Smoot et al. 1992).

The NASA-funded *Wilkinson Microwave Anisotropy Probe* (WMAP; Bennett et al. 2003a) mission was launched a decade after COBE-DMR, and mapped the microwave sky with 45 times higher sensitivity and 33 times higher angular resolution, and thereby revolutionizing our understanding of early universe physics (Bennett et al. 2003a). As quantified by Bennett et al. (2013), the permissible parameter space volume for a standard

Λ CDM model was decreased by a factor of 68,000 by WMAP, and the best pre-WMAP determination of the age of the universe was $t_0 < 14$ Gyr from Boomerang (Lange et al. 2001), with best-fit values of 9–11 Gyr; the latter values in apparent contradiction with direct measurements of the oldest globular clusters (Hu et al. 2001).

The ESA-led *Planck* satellite (Planck Collaboration I 2020) was developed concurrently with WMAP, and their operation lifetimes briefly overlapped, with *Planck* observing from 2009–2013 and WMAP from 2001–2011. *Planck*'s stated goal was to fully characterize the primary CMB temperature fluctuations from recombination, as well as to characterize the polarized microwave sky on large angular scales. Overall, *Planck*'s raw CMB sensitivity was an order of magnitude higher than WMAP's, and its angular resolution three times higher. Today, *Planck* represents the state-of-the-art in terms of full-sky microwave sky measurements.

Planck comprised two independent experiments, namely the Low Frequency Instrument (LFI; Planck Collaboration II 2020) and High Frequency Instrument (HFI; Planck Collaboration III 2020), respectively. The LFI detectors were based on HEMT (high electron mobility transistor) amplifiers, spanning three frequency channels between 30 and 70 GHz, while the HFI detectors were based on TES (transition edge sensitive) bolometers, and spanned six frequency channels between 100 and 857 GHz. For comparison, WMAP was also HEMT-based, with comparable sensitivity to LFI alone, and spanned five frequencies between 23 and 94 GHz. At the same time, the two experiments implemented very different scanning strategies, and as a result they are highly complementary and synergistic; together they provide a clearer view of the low-frequency microwave sky than either can alone.

Towards the end of the *Planck* analysis phase it became clear that the interplay between instrument calibration and astrophysical component separation represented a main limiting factor in terms of systematic effects for high signal-to-noise measurements (Planck Collaboration II 2020). Specifically, in order to calibrate the instrument to sufficient precision, it became clear that it was necessary to know the true sky to a comparably high precision – but to know the sky, it was also necessary to know the instrumental calibration. The data analysis is thus fundamentally circular and global in nature. The final official *Planck* LFI analysis performed four complete iterations between calibration and component separation (Planck Collaboration II 2020), aiming to probe this degeneracy. However, it was recognized that this was not sufficient to reach full convergence, and this sub-optimality led to the BEYONDPLANCK project (BeyondPlanck 2022), which aimed to perform thousands of complete analysis cycles, as opposed to just a handful. This framework was implemented using the Commander3 (Galloway et al. 2022a) code, a CMB Gibbs sampler that performs integrated high-level and low-level parameter estimation in a single integrated framework. This analysis demonstrated the feasibility of a full end-to-end Gibbs sampling analysis in the CMB framework, while providing the highest-quality LFI maps to date.

Rather than simply probing the degeneracy between instrument calibration and component separation, a better solution is to actually break it. The optimal approach to do so is by jointly analyzing complementary datasets, each of which provide key information regarding the full system. This insight led to the Cosmoglobe¹ initiative, which is an Open Source and community-wide effort that aims to derive a single joint model

¹ <https://cosmoglobe.uio.no>

of the radio, microwave, and sub-millimeter sky by combining all available state-of-the-art experiments. An obvious first extension of the LFI-oriented BEYONDPLANCK project is to analyze the *WMAP* measurements in the same framework. Indeed, already as part of the BEYONDPLANCK suite of papers, Watts et al. (2022) integrated *WMAP* *Q*-band time-ordered data (TOD) into the Commander3 framework, calibrated off of the BEYONDPLANCK sky model.

In this paper, we present the first end-to-end Bayesian analysis of the full *WMAP* TOD, processed within the Commander framework. As such, this paper also presents the first ever joint analysis of two major CMB experiments (LFI and *WMAP*) at the lowest possible level, and it therefore constitutes a major milestone of the COSMOGLOBE initiative. In the future, many more datasets will be added, gradually providing stronger and stronger constraints on the true astrophysical sky. Each new experiment will then also in turn improve the instrumental calibration of all previous experiments.

The rest of this paper is organized as follows. In Sect. 2, we provide a brief review of the Bayesian end-to-end statistical framework used in this work, before describing the underlying data and computational expenses in Sect. 3. The main results, as defined by as expressed by the global posterior distribution, are described in Sects. 4–6, summarizing instrumental parameters, frequency sky maps, and astrophysical results, respectively. In Sect. 7 we address unresolved issues that should be addressed in future work. We conclude in Sect. 8, and lay a path forward for the COSMOGLOBE project.

2. End-to-end Bayesian CMB analysis

The general computational analysis framework used in this work has been described in detail by BeyondPlanck (2022) and Watts et al. (2022) and references therein. In this section, we give a brief summary of the main points, and emphasize in particular the differences with respect to earlier work.

2.1. LFI and BEYONDPLANCK

The BEYONDPLANCK project (BeyondPlanck 2022) was the first true application of end-to-end Gibbs sampling in the framework of CMB data analysis. The *Planck* LFI data had been gradually improved through each *Planck* data release, specifically PR1 (Planck Collaboration II 2016), PR2 (Planck Collaboration II 2016), PR3 (Planck Collaboration II 2020), and PR4 (Planck Collaboration II 2016). Even after PR4, however, the final LFI maps still failed significant polarization null tests (in particular for the 44 GHz frequency channel), in particular due to incomplete characterization of relative gain. Indeed, already the PR3 analysis uncovered a strong degeneracy between the LFI gain solution and the astrophysical foreground model, and to break these the *Planck* LFI Data Processing Center (DPC) implemented an iterative scheme in which the various low-level processing and component separation operations were performed sequentially and repeatedly. However, because these iterations were performed manually with significant amounts of human interactions, this scheme was very slow, and only four full cycles were completed before the *Planck* collaboration ended. A main motivation for the BEYONDPLANCK project was to automate this process, and perform thousands of such iterations, rather than just four.

This work was highly successful, and the BEYONDPLANCK collaboration was able to generate the first LFI maps with true joint

estimation of sky components and underlying instrumental parameters through a statistical process called Gibbs sampling (BeyondPlanck 2022; Galloway et al. 2022a; Basyrov et al. 2022). The code used for this process was called Commander3 (Galloway et al. 2022a). The resulting Gibbs chains allowed for data-driven estimates of the instrumental properties to be determined by exploring the degeneracies between the low-level instrumental parameters themselves and our knowledge of the sky (Andersen et al. 2022; Svalheim et al. 2022b), and in doing so resulted in new state-of-the-art and low-systematics LFI maps.

2.2. Official WMAP instrument model and analysis pipeline

The main goal of the current paper is to perform a similar analysis with the *WMAP* time-ordered data, and thereby solve some of the long-standing unresolved issues with the official maps, in particular related to poorly constrained large-scale polarization modes. Before presenting our algorithm, however, it is useful to briefly review the official *WMAP* instrument model and analysis pipeline, which improved gradually over a total of five data releases, often referred to as the 1-, 3-, 5-, 7, and 9-year data releases, respectively. Unless otherwise noted, we will refer to the final 9-year results in the following. The official *WMAP* results delivered by Bennett et al. (2013) will be referred to as *WMAP9*.

The *WMAP* satellite carried forty differential polarization-sensitive radiometers grouped as differencing assemblies (DAs), where one pair was sensitive to the difference in signal at one polarization orientation and the other pair sensitive to the orthogonal polarization. In total, there were ten DAs, which were distributed as one *K*-band (23 GHz), one *Ka*-band (33 GHz), two *Q*-band (41 GHz), two *V*-band (61 GHz), and four *W*-band (94 GHz) DAs. Each radiometer records a science sample every $1.536/N_{\text{obs}}$ seconds, where N_{obs} is 12, 12, 15, 20 and 30 for *K*, *Ka*, *Q*, *V*, and *W*, respectively. The raw data are recorded as five digit integers with units du (digital unit).

The *WMAP* bandpasses were measured pre-launch on ground, sweeping a signal source through 201 frequencies and recording the output (Jarosik et al. 2003b). The bandpass responses have not been updated since the initial data release. However, as noted by Bennett et al. (2013), there has been an observed drift in the center frequency of *K*, *Ka*, *Q*, and *V*-band corresponding to a $\sim 0.1\%$ decrease over time. In practice, this did not affect the *WMAP* data processing because each year was mapped separately and co-added afterwards. An effective frequency calculator was delivered in the DR5 release as part of the IDL library to mitigate this effect during astrophysical analyses.²

The beams were characterized in the form of maps, with separate products for the near-field and far-field. The main beam and near sidelobes were characterized using a combination of physical optics codes and observations of Jupiter for each horn separately. The maps of Jupiter were then combined with the best-fit physical optics codes to create a map of the beam response (Hill et al. 2009; Weiland et al. 2011; Bennett et al. 2013).

Far sidelobes were estimated using a combination of laboratory measurements and Moon data taken during the mission (Barnes et al. 2003), as well as a physical optics model described by Hinshaw et al. (2009). To remove the far sidelobe in the TOD, an estimate was calculated by convolving the intensity map and the orbital dipole signal with the measured sidelobe signal (Jarosik et al. 2007). Although the sidelobe pickup was modeled by Barnes et al. (2003), it was determined that the results

² https://lambda.gsfc.nasa.gov/product/wmap/dr5/m_sw.html

were small enough to be neglected and have not been explicitly reported in any of the subsequent *WMAP* data releases.

The *WMAP* pointing solution was determined using the bore-sight vectors of individual feedhorns in spacecraft coordinates, in combination with on-board star trackers. Thermal flexure of the tracking structure introduced small pointing errors, as discussed by [Jarosik et al. \(2007\)](#). Using the temperature variation measured by onboard thermistors, the pointing solution was corrected using a model that returns angular deviation per kelvin. The residual pointing errors were computed using observations of Jupiter and Saturn, and the reported upper limit was given as 10'' ([Bennett et al. 2013](#); [Greason et al. 2012](#)).

The *WMAP* data were calibrated by jointly estimating the time-dependent gains, \mathbf{g} , and baselines, \mathbf{b} , as described by [Hinshaw et al. \(2007\)](#), [Hinshaw et al. \(2009\)](#), and [Jarosik et al. \(2011\)](#). The TOD were initially modeled as having constant gain and baseline for a 1–24 hour period, with parameters that were fit to the orbital dipole assuming T_0 from [Mather et al. \(1999\)](#) and a map made from a previous iteration of the mapmaking procedure. Once the gain and baseline solution had converged, the data were fit to a parametric form of the radiometer response as a function of housekeeping data, given in Appendix A of [Greason et al. \(2012\)](#).

One unique feature of the *WMAP* instrument is that it includes differential pointing. That is, *WMAP* had two primary mirrors positioned on opposite sides of the vertical satellite axis, tilted approximately 19.5° towards the Solar shield. Essentially, when horn A was pointed at pixel p_A , horn B was pointed at a pixel p_B approximately 141° away ([Page et al. 2003](#)). The incoming radiation was differenced in the electronics before being deposited on the detectors, essentially recording radiation proportional to $\mathbf{m}_A - \mathbf{m}_B$ and $\mathbf{m}_B - \mathbf{m}_A$ ([Jarosik et al. 2003b](#)). Each pair of radiometers had a partner pair of radiometers that observed the same pixels with sensitivity to the orthogonal polarization direction. Taking all these effects into account, the total data model for a single radiometer is given by

$$d_t^{\text{imbal}} \propto (1 + x_{\text{im}})T_{p_A} - (1 - x_{\text{im}})T_{p_B} \quad (1)$$

$$= (T_{p_A} - T_{p_B}) + x_{\text{im}}(T_{p_A} + T_{p_B}), \quad (2)$$

where T_{p_A} and T_{p_B} are the A- and B-side antenna temperatures, and x_{im} is the differential optical pickup between horns A and B. This effect is taken into account during mapmaking. However, inaccuracies in the determination of x_{im} will yield a spurious polarization component, and create artificial imbalance modes due to coupling with the sky signal, in particular with the bright Solar CMB dipole ([Jarosik et al. 2007](#)). The *WMAP* transmission imbalance factors were fit to the Solar dipole in TOD space, accounting for both common and differential modes ([Jarosik et al. 2003a, 2007](#)).

Data were flagged and masked before the final mapmaking step. In particular, station-keeping maneuvers, solar flares, and unscheduled events caused certain data to be unusable – the full catalog of these events is listed in Table 1.8 of [Greason et al. \(2012\)](#). In addition, data were masked depending on the channel frequency and the planet itself, with the full list of exclusion radii enumerated in Table 4 of [Bennett et al. \(2013\)](#).

To create the sky maps \mathbf{m} , the calibrated data were put into the asymmetric mapmaking equation,

$$\mathbf{P}_{\text{am}}^T \mathbf{N}^{-1} \mathbf{P} \mathbf{m} = \mathbf{P}_{\text{am}}^T \mathbf{N}^{-1} \mathbf{d}, \quad (3)$$

where \mathbf{N} is the noise covariance matrix, and the pointing matrix \mathbf{P} is implicitly defined for each datastream, \mathbf{d}_1 and \mathbf{d}_2 sensitive to different polarization orientations. The asymmetric mapmaking

matrix, \mathbf{P}_{am} , was used because, as noted by [Jarosik et al. \(2011\)](#), large signals observed in one beam could leak into the solution for the pixel observed by the other beam, leading to incorrect signals in the final map. The asymmetric mapmaking solution essentially works by only updating the matrix multiplication for beam A when beam A is in a high emission region and beam B is not, and vice versa. [Bennett et al. \(2013\)](#) also identified that these effects are pronounced when one horn is observing a cross a large temperature gradient, leading to excesses 140° away from the Galactic center. For each side A/B, the maps are defined as a function of the Stokes parameters $T_{A/B}$, $Q_{A/B}$, and $U_{A/B}$, with polarization angle $\gamma_{A/B}$, such that

$$\begin{aligned} \mathbf{d}_1 &= \mathbf{P}_1 \mathbf{m} \\ &= (1 + x_{\text{im}})[T_A + Q_A \cos 2\gamma_A + U_A \sin 2\gamma_A + S_A] \\ &\quad + (1 - x_{\text{im}})[-T_B - Q_B \cos 2\gamma_B - U_B \sin 2\gamma_B - S_B], \end{aligned} \quad (4)$$

and

$$\begin{aligned} \mathbf{d}_2 &= \mathbf{P}_2 \mathbf{m} \\ &= (1 + x_{\text{im}})[T_A - Q_A \cos 2\gamma_A - U_A \sin 2\gamma_A - S_A] \\ &\quad + (1 - x_{\text{im}})[-T_B + Q_B \cos 2\gamma_B + U_B \sin 2\gamma_B + S_B]. \end{aligned} \quad (5)$$

In this formalism, $S_{A/B}$ acts as an extra Stokes parameter that absorbs the effects of differing bandpass responses between radiometers \mathbf{d}_1 and \mathbf{d}_2 ([Jarosik et al. 2007](#)).

An accurate noise model was necessary to perform the maximum likelihood mapmaking, as it required the evaluation of the dense time-space inverse noise covariance matrix \mathbf{N}^{-1} . The time-space autocorrelation function was estimated for each year of data, which is then Fourier transformed, inverted, and Fourier transformed again to create an effective inverse noise operator $N_{tt'}^{-1}$. Finally, to create the sky maps themselves, the data are treated one year at a time, and the iterative Bi-conjugate Gradient Stabilized Method (BiCG-STAB [van der Vorst 1992](#); [Barrett et al. 1994](#)) is applied to the maps.

2.3. COSMOGLobe instrument model

Perhaps the most fundamental difference between the COSMOGLobe and *WMAP* (and those of most other CMB experiments) analysis pipelines is that while the *WMAP* pipeline models each channel in isolation, the COSMOGLobe framework simultaneously considers all data, both internally within *WMAP*, and also from all other sources, most notably also including *Planck*. The main advantage of such a global approach is significantly reduced parameter degeneracies, as data from observations with different frequency coverages and instrumental designs break the same degeneracies. For this approach to be computationally tractable, one must establish a global parametric model that simultaneously accounts for both the astrophysical sky and all relevant instruments. For the current *WMAP*+LFI oriented analysis, we adopt the following expression ([BeyondPlanck 2022](#)),

$$\mathbf{d} = \mathbf{GP}[\mathbf{B}^{\text{symm}} \mathbf{Ma} + \mathbf{B}^{4\pi}(s^{\text{orb}} + s^{\text{fsl}})] + \mathbf{s}^{\text{inst}} + \mathbf{n}^{\text{corr}} + \mathbf{n}^{\text{w}}, \quad (6)$$

where \mathbf{G} is the time-dependent gain in the form of the matrix $\text{diag}(g_t)$; \mathbf{P} is the $n_p \times n_t$ pointing matrix, where n_p is the number of pixels and n_t the number of TOD datapoints; \mathbf{B}^{symm} and $\mathbf{B}^{4\pi}$ are the symmetrized and full asymmetric beam, respectively; \mathbf{M} is the mixing matrix between a given component c with spectral energy distribution $f_c(\nu/\nu_{0,c})$ and a detector j with bandpass $\tau_j(\nu)$, given by

$$M_{cj} = \int d\nu \tau_j(\nu) f_c(\nu/\nu_{c,0}). \quad (7)$$

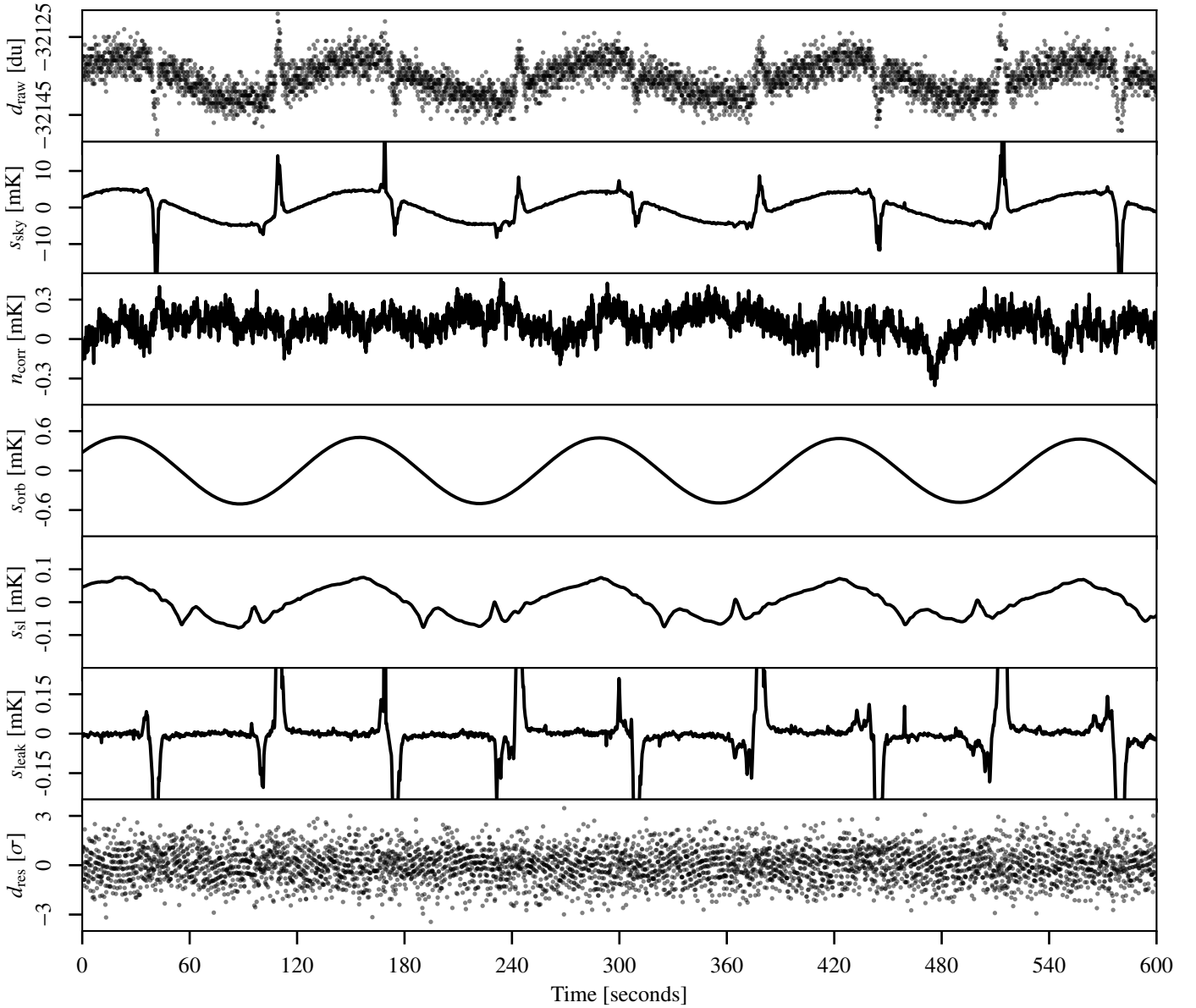


Fig. 1. Time-ordered data segment for the K113 radiometer. From top to bottom, the panels show 1) raw uncalibrated TOD \mathbf{d} ; 2) sky signal s_{sky} ; 3) calibrated correlated noise n_{corr} ; 4) orbital CMB dipole signal s_{orb} ; 5) sidelobe correction s_{sl} ; 6) bandpass leakage correction s_{leak} ; and 7) residual TOD, $d_{\text{res}} = (\mathbf{d} - \mathbf{n}_{\text{corr}} - \mathbf{b})/g - s_{\text{sky}} - s_{\text{orb}} - s_{\text{leak}} - s_{\text{sl}}$, in units of $\sigma_0[\text{du}]$ for this TOD segment. Note that the vertical range varies significantly from panel to panel.

The maps \mathbf{a} represent the Stokes parameters for each astrophysical component, while s^{orb} is the orbital dipole induced by the motion of the telescope with respect to the Sun, and s^{fsl} is the time-dependent far sidelobe signal. Following Ihle et al. (2022), we model the correlated noise component n^{corr} in terms of a $1/f$ power spectral density (PSD), which explicitly takes the form $P_n(f) = \sigma_0^2(1 + (f/f_k)^\alpha)$, where σ_0 denotes the white noise amplitude, f_{knee} is the so-called $1/f$ knee frequency, and α is a free power law slope. For notational purposes, we denote the set of all correlated noise parameters by $\xi_n = \{\sigma_0, f_k, \alpha\}$. We note that this model represents a significant approximation, as the actual WMAP noise is known to be significantly colored at high temporal frequencies. The main impact of this approximation is a worse-than-expected χ^2 goodness of fit statistic. However, measured in absolute noise levels the effect is very small, and has very little if any impact on the final science results; for further discussion of this approximation, see Sect. 7.1.

The term s^{inst} denotes any instrument-specific terms that might be required for a given experiment. For instance, for LFI it is used to model the 1 Hz spike contribution due to electronic cross-talk. For WMAP, we use it for first-order baseline corrections, and set $s_t^{\text{WMAP}} = b_0 + b_1 t$, where b_0 and b_1 represent the mean and slope of the baselines over the data segment in question. We note that while the WMAP team fitted a single constant baseline over either 1- or 24-hour periods, our data segments are typically several days long (corresponding to a number of samples chosen to optimize Fourier transforms). A natural question is therefore whether nonlinear baseline variations could induce artefacts. In this regard, it is important to note that the correlated noise component effectively acts as a single-sample baseline correction that can absorb by far most such nonlinearities, as long as their total effect on the power spectrum does not exceed that imposed by the $1/f$ model. In practice, that is a very mild constraint. At the same time, visual inspection of n^{corr} projected into

sky maps provides a very powerful check on any potential baseline residuals; these will appear as correlated stripes aligned with the *WMAP* scanning path. This has been used to identify and mitigate modeling errors several times in the course of this analysis. In sum, it is important to note that the CosMOGLOBE model allows for a more flexible baseline behaviour than the *WMAP* pipeline.

A third notable difference between the *WMAP* and CosMOGLOBE data models concerns bandpass mismatch. While the *WMAP* pipeline simply projects out any bandpass difference from the polarization maps by solving for the spurious S maps, we model it explicitly through the use of the global astrophysical sky model (Svalheim et al. 2022a). Explicitly, the expected calibrated sky signal for radiometer j is given by

$$m_{p,j} = \mathbf{B}_{p,p'} \sum_c M_{c,j} a_{p'}^c + n_{j,p}^w. \quad (8)$$

Since $M_{c,j}$ encodes the bandpass response of every detector j to every sky component c , the detector-specific maps, \mathbf{m}_j , will each be slightly different depending on their bandpass τ_j . Therefore, before averaging different detectors together, we estimate the average over all detectors in a given frequency channel $\mathbf{m} \equiv \langle \mathbf{m}_j \rangle$, and subtract it directly in the timestream;

$$\delta s_{t,j}^{\text{leak}} = \mathbf{P}_{t,p}^j \mathbf{B}_{p,p'} (\mathbf{m}_{j,p'} - \mathbf{m}_{p'}). \quad (9)$$

This leakage term uses the expected bandpass response to remove the expected component that deviates from the mean in the timestream, directly reducing polarization contamination.

To build intuition regarding this model, we plot in Fig. 1 both the TOD and the individual model components for an arbitrarily selected ten-minute segment for the *WMAP*'s $K113$ radiometer. The uncalibrated data, \mathbf{d}_{raw} , is displayed in the top panel, with the sky signal $s_{\text{sky}} = \mathbf{P}\mathbf{B}^{\text{symm}}\mathbf{M}\mathbf{a}$ plotted directly underneath. The next four panels show the correlated noise realization \mathbf{n}_{corr} , the orbital dipole \mathbf{s}_{orb} , the far sidelobe contribution \mathbf{s}_{sl} , and the bandpass leakage \mathbf{s}_{leak} . Finally, we also plot the time-ordered residual for this segment of data, obtained by subtracting the model from the raw data, in units of the estimated white noise level.

2.4. Sky model

Following BeyondPlanck (2022), we assume that the sky (as defined by $\mathbf{M}\mathbf{a}$ in Eq. (6) across the *WMAP* frequencies can be modeled as a linear combination of CMB fluctuations (\mathbf{a}_{CMB}), synchrotron (\mathbf{a}_s), free-free emission (\mathbf{a}_{ff}), anomalous microwave emission (\mathbf{a}_{AME} , AME), thermal dust (\mathbf{a}_d), and radio point sources ($\mathbf{a}_{j,\text{src}}$). Explicitly, we assume that the astrophysical sky (in units of brightness temperature) may be modelled as follows,

$$s_{\text{RJ}} = (\mathbf{a}_{\text{CMB}} + \mathbf{a}_{\text{quad}}(\nu)) \frac{x^2 e^x}{(e^x - 1)^2} + \quad (10)$$

$$+ \mathbf{a}_s \left(\frac{\nu}{\nu_{0,s}} \right)^{\beta_s} + \quad (11)$$

$$+ \mathbf{a}_{\text{ff}} \left(\frac{\nu_{0,\text{ff}}}{\nu} \right)^2 \frac{g_{\text{ff}}(\nu; T_e)}{g_{\text{ff}}(\nu_{0,\text{ff}}; T_e)} + \quad (12)$$

$$+ \mathbf{a}_{\text{AME}} e^{\beta_{\text{AME}}(\nu - \nu_{0,\text{AME}})} + \quad (13)$$

$$+ \mathbf{a}_d \left(\frac{\nu}{\nu_{0,d}} \right)^{\beta_d+1} \frac{e^{h\nu_{0,d}/k_B T_d} - 1}{e^{h\nu/k_B T_d} - 1} + \quad (14)$$

$$+ U_{\text{mJy}} \sum_{j=1}^{N_{\text{src}}} \mathbf{a}_{j,\text{src}} \left(\frac{\nu}{\nu_{0,\text{src}}} \right)^{\alpha_{j,\text{src}}-2}, \quad (15)$$

where $x = h\nu/kT_{\text{CMB}}$; $\nu_{0,i}$ is a reference frequency for component i ; β_s is a power-law index for synchrotron emission (which may take different values for temperature and polarization); T_e is the electron temperature, and g_{ff} is the so-called Gaunt factor (Dickinson et al. 2003); β_{AME} is an exponential scale factor for AME emission (see below); β_d and T_d are the emissivity and temperature parameters for a single modified blackbody thermal dust model; $\alpha_{j,\text{sr}}$ is the spectral index of point source j relative to the same source catalog as used by Planck Collaboration IV (2018); and U_{mJy} is the conversion factor between flux density (in millijansky) and brightness temperature (in K_{RJ}) for the channel in question. Finally, \mathbf{a}_{quad} accounts for a relativistic quadrupole correction due to the Earth's motion through space (Notari & Quartin 2015).

In general, this model is nearly identical to the one adopted by BeyondPlanck (2022). However, there is one notable exception, namely the spectral energy density (SED) for the AME component, $s_0^{\text{sd}}(\nu)$. In this current work, we adopt a simple exponential function for this component, as for instance proposed by Hensley et al. (2015), which is notably different from the SpDust2 model (Ali-Haïmoud et al. 2009; Ali-Haïmoud 2010; Silsbee et al. 2011) that was used in the BEYONDPLANCK analysis. The motivation for this modification is discussed in detail by Watts et al. (2023): First and foremost, the current combination of *WMAP* and LFI data appears to prefer a higher signal amplitude at frequencies between 40 and 60 GHz than can easily supported by SpDust2. This was first noted by Planck Collaboration IX (2016), who solved this issue by introducing a second independent AME component. For the original BEYONDPLANCK analysis, on the other hand, this excess was not statistically significant, simply because that analysis did not include the powerful *WMAP* K -band data. In the current analysis, the excess is obvious. The observation that a simple one-parameter exponential model fits the data as well as the complicated multi-parameter model of Planck Collaboration IX (2016) is a novel result from the current work. Indeed, it fits also about as well as the commonly used log-normal model derived by Stevenson (2014), which also has one extra parameter. By virtue of having fewer degrees of freedom than any of the previous models, we adopt the exponential model in the following.

2.5. Priors and poorly measured modes

The model described in Sects. 2.2 and 2.4 is prone to several degeneracies, allowing for unphysical solutions to be explored in the Gibbs chain. Such unphysical degeneracies are highly undesirable for two main reasons. First, they increase the statistical uncertainties on most (if not all) other important parameters in the model – sometimes to the point that the target quantity is rendered entirely unmeasurable. Secondly, and perhaps even more importantly, the data model described above is known to be a (sometimes crude) approximation to the real observations, and there will invariably be modelling errors. Degeneracies then generally tend to amplify their impact, in the sense that any unconstrained parameters will typically be used to fit such small modelling errors. For both these reasons, it is generally preferable to impose either informative or algorithmic priors on the unconstrained parameters, rather than to leave them entirely unconstrained in the model.

An important example of an algorithmic prior is the foreground smoothing prior used by Planck Collaboration IV (2018) and Andersen et al. (2022), which dictates that astrophysical foregrounds has to be smooth on small angular scales. This is justified by noting that the angular spectrum on large and inter-

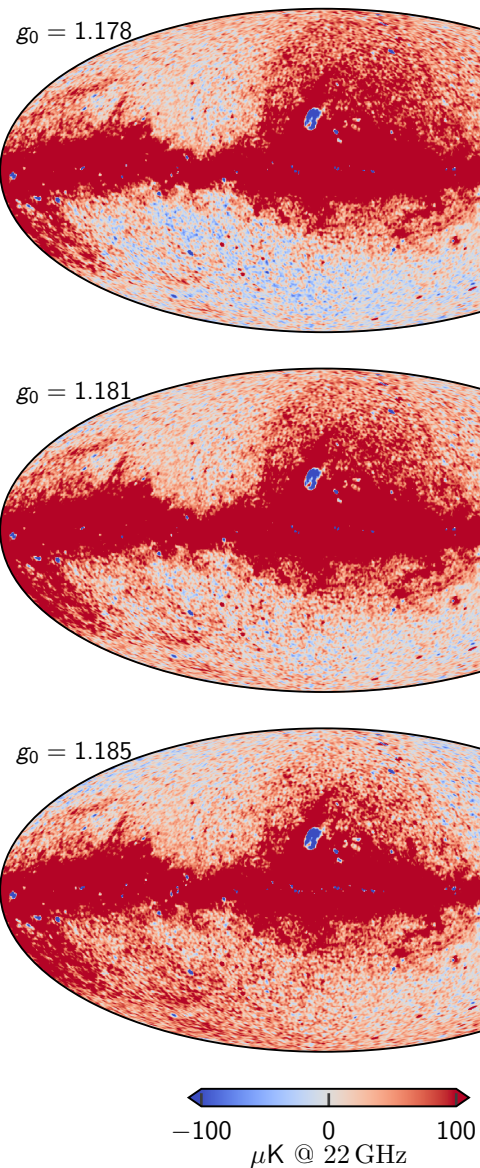


Fig. 2. Dependence on AME amplitude evaluated at 22 GHz as a function of absolute calibration. Each map comes from the fifth iteration of a dedicated Commander3 run that fixed g_0 while letting all other TOD parameters be fit. The values of $g_0 = 1.178$ and $g_0 = 1.185$ represent 3.5σ draws from the prior distribution with mean 1.181 and standard deviation 0.001. The dipole visible in the top and bottom panels is aligned perfectly with the Solar dipole, and is directly due to variations in the K -band absolute calibration.

mediate scales typically falls as a power-law in multipole space; extrapolating this into the noise dominated regime prevents the overall foreground model from becoming degenerate at small scales.

Correspondingly, important examples of informative priors are the use of HFI constraints on the thermal dust SED parameters, β_d and T_d in BEYONDPLANCK. Because that analysis only included the highest HFI frequency channel, they had very little constraining power on the thermal dust SED. Rather than trying to fit these directly from LFI WMAP alone, they instead imposed informative Gaussian priors on each of these parameters, as derived from the HFI observations (Planck Collaboration IV 2018).

In the current analysis, and unless otherwise noted, we adopt the same algorithmic and informative priors as BeyondPlanck (2022). However, there are three notable exceptions, as detailed below, all of which are dictated either by the fact that we include the WMAP K -band channel (which has a strong impact on the low-frequency foreground model), or by the fact that we now process the WMAP data in time-domain, and therefore are subject to the same degeneracies as the official WMAP low-level pipeline, and that were solved with similar implicit or explicit prior in the original analysis.

First and foremost, and as detailed in Sect. 7.3, we observe in the current analysis a very strong degeneracy between the absolute calibration of the K -band channel and the dipole of the AME map. This makes intuitive sense, since K -band is by far the strongest channel in terms of AME signal-to-noise ratio, exceeding that of LFI 30 GHz by about a factor of four; see Sect. 6.4. Effectively, a small variation in the absolute gain may be countered by subtracting the corresponding CMB Solar dipole variation from the AME map, and end up with a nearly identical total χ^2 ; the orbital CMB dipole is not bright enough at 23 GHz relative to AME emission to break this degeneracy.

This is illustrated in Fig. 2, which shows the derived AME amplitude map for three different values of the mean K -band gain, g_0 , namely 1.178, 1.181, and 1.184 $\mu\text{K mK}^{-1}$; the extreme values differ only by 0.25 %. All of these three values appear equally acceptable from a pure χ^2 point-of-view, relative to the noise level and modeling errors of these data. At the same time, it is clear from visual inspection that only the middle value actually makes physical sense, as compared to what we know about the structure of the Milky Way. For this reason, we apply a Gaussian prior on the absolute K -band gain of $g_0 \sim N(1.181, 0.001^2)$ in the following, to regularize this issue. Thus, the extreme panels in Fig. 2 represent $\pm 2.5\sigma$ outliers, respectively, and will appear in our Markov chains with a frequency of about 1-in-100.

It is reasonable to ask why the WMAP pipeline produced sensible results without applying such a prior during their calibration procedure. We posit that the answer is due to the main difference between the two approaches. While COSMOGLOBE attempts to fit a single overall parametric model to all data at once, the WMAP pipeline calibrated each channel independently by co-adding data from one channel into a map, subtracting that map from the TOD, fitting the gain to the orbital dipole, and iterating until the solution became stable. An advantage of the single-channel approach is that the solution is independent of the assumed sky model. However, a disadvantage is that it is impossible to break any potential inherent degeneracies; it cannot be combined with external observations in any meaningful way. One important example of this for the WMAP data is a strong degeneracy between the transmission imbalance factors and the polarized sky signal; it is exceedingly difficult to break this degeneracy using data from only one radiometer alone, and the resulting errors will propagate to most other aspects in the analysis. In the global approach, on the other hand, the polarization modes that are poorly measured by WMAP alone are well measured by Planck and vice-versa, resulting in an overall better fit.

Second, as reported by Svalheim et al. (2022b) for the BEYONDPLANCK analysis, another important degeneracy in the current global model concerns the spectral index of polarized synchrotron emission versus the time-variable detector gain; when fitting both the polarized synchrotron amplitude and calibration freely without priors, the synchrotron spectral index at high Galactic latitudes tend to be biased toward unreasonably flat values, $\beta \lesssim -2.5$, which was likely due to a low level of unmodelled systematics, for instance temperature-to-polarization leak-

age, rather than true polarized synchrotron emission. In turn, this resulted in a contaminated CMB sky map with a strong synchrotron morphology. To break this degeneracy, Svalheim et al. (2022b) chose to marginalize the high-latitude synchrotron spectral index over a Gaussian prior of $\mathcal{N}(-3.30, 0.1^2)$, informed by Planck Collaboration V (2020), rather than estimate it from the data themselves. In the current analysis, we observe the same degeneracy, and the introduction of the K -band data is not sufficient to break it on its own. For this reason, we choose to apply the same informative prior in the current analysis.

Third and finally, we also marginalize over the AME scale index with a prior of $\beta_{\text{AME}} \sim \mathcal{N}(3.56, 0.1^2)$. The parameters of these priors were determined by running a grid over β_{AME} , and identifying the range that resulted in reasonable residuals near the Galactic plane, similar to that shown in Fig. 2 for the absolute calibration of K -band. We note that this prior should in principle be replaced with direct χ^2 -based posterior optimization, combined with a properly tailored analysis mask. However, the recent release of the QUIJOTE data (Rubíño-Martín et al. 2023), which covers the 11–19 GHz frequency range, suggests that the entire AME model should be revisited in a future joint WMAP+LFI+QUIJOTE analysis. We therefore leave detailed prior and SED optimization to that work. For further information regarding AME modelling with the current dataset, we refer the interested reader to Watts et al. (2023).

2.6. Posterior distribution and Gibbs sampling

As shown by BeyondPlanck (2022), this joint parametric description of the instrumental effects and sky allows us to write down a total model for the data, $\mathbf{d} = \mathbf{s}^{\text{tot}}(\omega) + \mathbf{n}^w$, where \mathbf{s}^{tot} encompasses all of the terms in Eq. (6) except for the white noise term. Assuming that all instrumental effects have been modeled adequately, and that the white noise is Gaussian distributed, the data should then also be Gaussian distributed with a mean of $\mathbf{s}^{\text{tot}}(\omega)$ and variance σ_0^2 . In general, the likelihood reads

$$P(\mathbf{d} | \omega) \propto \exp\left(-\frac{1}{2} \sum_t \frac{(d_t - s_t^{\text{tot}}(\omega))^2}{\sigma_0^2}\right). \quad (16)$$

If $\mathbf{d} \sim \mathcal{N}(\mathbf{s}^{\text{tot}}, \sigma_0^2)$ is the correct model for the data, the argument of the exponent is proportional to a χ^2 -distribution with n_{TOD} degrees of freedom. In the limit of large n , a χ^2 distribution is well-approximated by a Gaussian with mean n and variance $2n$. Therefore we define and use in the following the reduced normalized χ^2 statistic,

$$\chi^2 \equiv \frac{\sum_t ((d_t - s_t^{\text{tot}})^2 / \sigma_0^2) - n_{\text{TOD}}}{\sqrt{2n_{\text{TOD}}}}, \quad (17)$$

which is approximately drawn from the standard normal distribution $\mathcal{N}(0, 1)$.

Following BeyondPlanck (2022), the COSMOGLOBE Gibbs chain for this analysis is given by

$$\mathbf{g} \leftarrow P(\mathbf{g} \mid \mathbf{d}, \xi_n, \mathbf{s}^{\text{inst}}, \boldsymbol{\beta}, \mathbf{a}, C_\ell, \theta) \quad (18)$$

$$\mathbf{n}^{\text{corr}} \leftarrow P(\mathbf{n}^{\text{corr}} \mid \mathbf{d}, \mathbf{g}, \xi_n, \mathbf{s}^{\text{inst}}, \boldsymbol{\beta}, \mathbf{a}, C_\ell, \theta) \quad (19)$$

$$\xi_n \leftarrow P(\xi_n \mid \mathbf{d}, \mathbf{g}, \mathbf{n}^{\text{corr}}, \mathbf{s}^{\text{inst}}, \boldsymbol{\beta}, \mathbf{a}, C_\ell, \theta) \quad (20)$$

$$\mathbf{s}^{\text{inst}} \leftarrow P(\mathbf{s}^{\text{inst}} \mid \mathbf{d}, \mathbf{g}, \mathbf{n}^{\text{corr}}, \xi_n, \boldsymbol{\beta}, \mathbf{a}, C_\ell, \theta) \quad (21)$$

$$\boldsymbol{\beta} \leftarrow P(\boldsymbol{\beta} \mid \mathbf{d}, \mathbf{g}, \mathbf{n}^{\text{corr}}, \xi_n, \mathbf{s}^{\text{inst}}, C_\ell, \theta) \quad (22)$$

$$\mathbf{a} \leftarrow P(\mathbf{a} \mid \mathbf{d}, \mathbf{g}, \mathbf{n}^{\text{corr}}, \xi_n, \mathbf{s}^{\text{inst}}, \boldsymbol{\beta}, C_\ell, \theta) \quad (23)$$

$$C_\ell \leftarrow P(C_\ell \mid \mathbf{d}, \mathbf{g}, \mathbf{n}^{\text{corr}}, \xi_n, \mathbf{s}^{\text{inst}}, \boldsymbol{\beta}, \mathbf{a}, \theta) \quad (24)$$

$$\theta \leftarrow P(\theta \mid \mathbf{d}, \mathbf{g}, \mathbf{n}^{\text{corr}}, \xi_n, \mathbf{s}^{\text{inst}}, \boldsymbol{\beta}, \mathbf{a}, C_\ell), \quad (25)$$

with each step requiring its own dedicated sampling algorithm. The Commander3 pipeline is designed so that results of each Gibbs sample can be easily passed to each other, and that the internal calculations of each step do not directly depend on the inner workings of each other, which greatly increases modularity of the code.

2.7. Sampling algorithms

Before we discuss the results of this Gibbs chain as applied to the *Planck* LFI and WMAP data, we summarize the TOD processing steps in this section. Each step of the Gibbs chain requires its own conditional distribution sampling algorithm. In Sect. 2.7.1 we review the sampling algorithms implemented in the BEYONDPLANCK suite of papers, while Sects. 2.7.2–2.7.4 provide an overview of the WMAP-specific processing steps.

2.7.1. Review of sampling algorithms

By far most of the techniques required for WMAP data analysis have already been described in the BEYONDPLANCK project and implemented in Commander3. This section includes a summary of the algorithms that were used previously for the analysis of LFI data. In each of these cases, every part of the model not explicitly mentioned is held fixed unless specified otherwise.

Noise estimation and calibration are described by Ihle et al. (2022) and Gjerløw et al. (2022), respectively. As noted in those works, these two steps are strongly correlated, simply because the timestream

$$d_{t,i} = g_{q,i} s_{t,i}^{\text{tot}} + n_{t,i}^{\text{corr}} + n_{t,i}^{\text{wn}} \quad (26)$$

may be almost equally well fit by two solutions defined by $g' = g s^{\text{tot}} / (s^{\text{tot}})'$ or $(n^{\text{corr}})' = n^{\text{corr}} + g s^{\text{tot}} + g'(s^{\text{tot}})'$; the only thing that breaks this degeneracy is the noise PSD, which is a relatively loose constraint. A Gibbs sampler is by nature not very effective for nearly degenerate distributions, and we therefore instead define a joint sampling step for the correlated noise and gain. In practice, this is done by first drawing the calibration from its marginal distribution with respect to \mathbf{n}^{corr} , and then drawing \mathbf{n}^{corr} from its conditional distribution with respect to g ,

$$\mathbf{g} \leftarrow P(\mathbf{g} \mid \mathbf{d}, \xi_n) \quad (27)$$

$$\mathbf{n}^{\text{corr}} \leftarrow P(\mathbf{n}^{\text{corr}} \mid \mathbf{d}, \mathbf{g}, \xi_n). \quad (28)$$

One can see that this is a valid sample from the joint distribution from the definition of a conditional distribution, $P(\mathbf{g}, \mathbf{n}^{\text{corr}} \mid \omega) = P(\mathbf{n}^{\text{corr}} \mid \mathbf{g}, \omega)P(\mathbf{g} \mid \omega)$. In practice, this simply means that when sampling for \mathbf{g} , the covariance matrix $\mathbf{N} = \mathbf{N}_{\text{wn}} + \mathbf{N}_{\text{corr}}$ must be used, rather than just \mathbf{N}_{wn} .

Commander3 models the gain at each timestream t for a detector i as

$$g_{t,i} = g_0 + \Delta g_i + \delta g_{q,i}, \quad (29)$$

where q labels the time interval for which we assume the gain is constant, typically a single scan. In order to sample the gain, we write down a generative model for the TOD,

$$\mathbf{d}_i = \mathbf{g}_i s_i^{\text{tot}} + \mathbf{n}_i^{\text{tot}} \sim \mathcal{N}(\mathbf{g}_i s_i^{\text{tot}}, \mathbf{N}_i). \quad (30)$$

Since the \mathbf{d}_i is given as a linear combination of the fixed signal and the gains, a random sample of the gain can be drawn by solving³

$$[(s_i^{\text{tot}})^T \mathbf{N}_i^{-1} s_i^{\text{tot}}] \mathbf{g}_i = (s_i^{\text{tot}})^T \mathbf{N}_i^{-1} \mathbf{d}_i + (s_i^{\text{tot}})^T \mathbf{N}_i^{-1/2} \boldsymbol{\eta}, \quad (31)$$

where $\boldsymbol{\eta} \sim \mathcal{N}(0, 1)$ is a vector of standard normal variables. Note that \mathbf{N}_i depends implicitly on the noise PSD ξ_n , while the fluctuations corresponding to \mathbf{n}^{corr} are properly downweighted by $\mathbf{N}_{\text{corr},i}$. As detailed by Gjerløw et al. (2022), **Commander3** samples in practice g_0 , Δg_i , and $\delta g_{q,i}$ in separate sampling steps. Specifically, the absolute calibration g_0 is for the CMB-dominated channels only fitted using the orbital dipole, while the relative calibrations, Δg_i , exploits the full sky signal. The same is true for the time-dependent gain fluctuations, $\delta g_{q,i}$, and in this case an additional smoothness prior is applied through an effective Wiener filter. It is worth noting that the Gibbs chain is formally broken by fitting the absolute gain g_0 to the orbital dipole alone, as opposed to the full sky signal. However, this makes the sampling more robust with respect to unmodeled systematic effects, somewhat analogous to applying a confidence mask when estimating the CMB power spectrum.

The correlated noise sampling, described by Ihle et al. (2022), follows a similar procedure, except this now conditions upon the previous gain estimate, which is sampled immediately before the correlated noise component in the code. Similar to the gain case, we can write a generative model for the data,

$$\mathbf{d}_i = \mathbf{g}_i s_i^{\text{tot}} + \mathbf{n}_i^{\text{corr}} + \mathbf{n}_i^{\text{wn}} \sim \mathcal{N}(\mathbf{g}_i s_i^{\text{tot}}, \mathbf{N}_{\text{corr},i} + \mathbf{N}_{\text{wn},i}). \quad (32)$$

Given fixed $\mathbf{r}_i = \mathbf{d}_i - \mathbf{g}_i s_i^{\text{tot}}$, we can again write a sampling equation,

$$(\mathbf{N}_{\text{corr},i}^{-1} + \mathbf{N}_{\text{wn},i}^{-1}) \mathbf{n}_i^{\text{corr}} = \mathbf{N}_{\text{wn},i}^{-1} \mathbf{r}_i + \mathbf{N}_{\text{wn},i}^{-1/2} \boldsymbol{\eta}_1 + \mathbf{N}_{\text{corr},i}^{-1/2} \boldsymbol{\eta}_2. \quad (33)$$

This gives a sample of the underlying correlated noise.

To sample the correlated noise parameters, we assume that the correlated noise is drawn from a correlated Gaussian and form the conditional posterior distribution,

$$P(\xi_n | \mathbf{n}^{\text{corr}}) \propto \frac{\exp[-\frac{1}{2}(\mathbf{n}^{\text{corr}})^T \mathbf{N}_{\text{corr}}^{-1} \mathbf{n}^{\text{corr}}]}{\sqrt{|\mathbf{N}_{\text{corr}}|}} P(\xi_n). \quad (34)$$

The simplest and most commonly used parameterization for correlated noise is given by

$$\mathbf{N}_{\text{corr}}(f) = \sigma_0^2 \left(\frac{f}{f_{\text{knee}}} \right)^\alpha. \quad (35)$$

This can in principle be modified, and for *Planck* LFI a Gaussian log-normal bump was added at a late stage in the BEYOND-PLANCK analysis. Rather than sampling for σ_0 , we effectively fix

the white noise level to the noise level at the highest frequency, e.g.,

$$\sigma_0^2 \equiv \frac{\text{Var}(r_{t+1} - r_t)}{2}, \quad (36)$$

where t and $t + 1$ are consecutive time samples, and $r \equiv \mathbf{d} - \mathbf{gs}^{\text{tot}} - \mathbf{n}^{\text{corr}}$. In practice, this makes σ_0 a deterministic function of the sampled sky and gain parameters. The parameters α and f_{knee} are not linear in the data, and they can be sampled efficiently using a standard inversion sampler (see, e.g., Appendix A.3 of BeyondPlanck (2022) or Chapter 7.3.2 of Press et al. (2007) for further details). In practice, this requires computing the posterior over a linear grid one parameter at a time.

Once the instrumental parameters have been sampled, **Commander3** computes the calibrated TOD for each band,

$$r_{t,j} = \frac{d_{t,j} - n_{t,j}^{\text{corr}}}{g_{t,j}} - (s_{t,j}^{\text{orb}} + s_{t,j}^{\text{fsl}} + \delta s_{t,j}^{\text{leak}} + s_{t,j}^{\text{inst}}) \quad (37)$$

where s^{orb} is the orbital dipole (Gjerløw et al. 2022), s^{fsl} is the far sidelobe timestream (Galloway et al. 2022b), δs^{leak} is the bandpass leakage (Svalheim et al. 2022a), and s^{inst} is some instrumental-specific contribution, e.g., the 1 Hz electronic spike for LFI. With a correlated noise realization removed, one can perform simple binned mapmaking, weighting each pixel by the white noise amplitude.

2.7.2. Differential mapmaking

The first additional algorithm that needs to be added to **Commander3** in order to process WMAP TOD data is support for differential mapmaking (Watts et al. 2022). After calibration and correction for instrumental effects, the TOD can be modeled as

$$\mathbf{d} = \mathbf{Pm} + \mathbf{n}^{\text{w}}, \quad (38)$$

where

$$\mathbf{m} = \mathbf{B}^{\text{symm}} \mathbf{Ma} \quad (39)$$

is the expected map for each detector after removing the orbital dipole, far sidelobe, baseline, and a realization of correlated noise. The differential pointing strategy can be represented in matrix form as

$$\begin{aligned} \mathbf{P}_{tp} = & (1 + x_{\text{im}})(\delta p' p_A^I + \delta p^O p_A^O \cos 2\psi_A + \delta p^U p_A^U \sin 2\psi_A) \\ & - (1 - x_{\text{im}})(\delta p' p_B^I - \delta p^O p_B^O \cos 2\psi_B - \delta p^U p_B^U \sin 2\psi_B) \end{aligned} \quad (40)$$

where p_A and p_B are the time-dependent pointings for each DA. The maximum likelihood map can now in principle be derived using the usual mapmaking equation,

$$\mathbf{P}^T \mathbf{N}^{-1} \mathbf{Pm} = \mathbf{P}^T \mathbf{N}^{-1} \mathbf{d}. \quad (41)$$

For a single-horn experiment, i.e., *Planck* LFI, this reduces to a 3×3 matrix that can be inverted for each pixel independently. For the pointing matrix in Eq. (40), this is no longer possible, as there is inherently coupling between horns A and B in the timestreams. The $3N_{\text{pix}} \times 3N_{\text{pix}}$ matrix can be solved using an iterative algorithm, e.g., preconditioned conjugate gradients (Shewchuk 1994).

Jarosik et al. (2011) identified an issue where a large difference in the sky temperature values at pixel A versus pixel B induced artifacts in the mapmaking procedure. We adopt the

³ See, e.g., Appendix A.2 of BeyondPlanck (2022) for a derivation of this result.

procedure first described by Hinshaw et al. (2003) where only the pixel in a bright region, defined by a small processing mask (Bennett et al. 2013) is accumulated, thus modifying the map-making equation to

$$\mathbf{P}_{\text{am}}^T \mathbf{N}^{-1} \mathbf{P} \mathbf{m} = \mathbf{P}_{\text{am}}^T \mathbf{N}^{-1} \mathbf{d}. \quad (42)$$

This equation can be solved using the BiCG-STAB algorithm for a non-symmetric matrix \mathbf{A} where $\mathbf{Ax} = \mathbf{b}$. We apply a preconditioner \mathbf{M} by numerically inverting the same problem with $N_{\text{side}} = 16$ maps and applying a diagonal noise matrix. Numerically, we define convergence as when the residual $\mathbf{r} \equiv \mathbf{b} - \mathbf{Ax}$ satisfies $\mathbf{r}^T \mathbf{M}^{-1} \mathbf{r} / \mathbf{b}^T \mathbf{M}^{-1} \mathbf{b} < 10^{-10}$, which typically takes about 20 iterations for producing frequency maps.

2.7.3. Transmission imbalance estimation

Transmission imbalance, the differential power transmission of the optics and waveguide components, can be parameterized as

$$d_{t,j} = g_{t,j}[(1 + x_{\text{im},j})s_{t,j}^{\text{tot,A}} - (1 - x_{\text{im},j})s_{t,j}^{\text{tot,B}}] + n_t. \quad (43)$$

This can be decomposed into a differential (d) and common-mode (c) signal such that

$$d_{t,j} = g_{t,j}[s_{t,j}^{\text{d}} + x_{\text{im},j}s_{t,j}^{\text{c}}] + n_t. \quad (44)$$

In this form, the imbalance parameters can be estimated by drawing Gaussian samples from the standard mean and standard deviation over the entire mission. To draw samples for $x_{\text{im},j}$, we construct a sampling routine analogous to the gain estimation of Eq. (31) and correlated noise estimation of Eq. (33), with $\mathbf{r} = \mathbf{d} - \mathbf{gs}^{\text{d}}$,

$$[(\mathbf{gs}^{\text{c}})^T \mathbf{N}^{-1} \mathbf{gs}^{\text{c}}]x_{\text{im}} = (\mathbf{gs}^{\text{c}})^T \mathbf{N}^{-1} \mathbf{r} + (\mathbf{gs}^{\text{c}})^T \mathbf{N}^{-1/2} \boldsymbol{\eta}, \quad (45)$$

essentially cross-correlating the common-mode signal with \mathbf{r} with appropriate weights and adding a Gaussian random variable with the correct weighting. Note that we are marginalizing over the correlated noise here by using $\mathbf{N} = \mathbf{N}_{\text{wn}} + \mathbf{N}_{\text{corr}}$. This mitigates any baseline drifts being erroneously attributed to the common-mode signal and biasing the estimate of x_{im} .

The WMAP procedure, described by Jarosik et al. (2003a), fit for common-mode and differential coefficients along with a cubic baseline over 10 precession periods at a time, corresponding to 10 hours of observation. The mean and uncertainty were then calculated by averaging and taking the standard deviation of these values. This approach has the benefit of allowing for the tracking of possible transmission imbalance variation throughout the mission. However, none of the WMAP suite of papers have found evidence for this, and it has not arisen in our analysis, so we model this as an effect whose value is constant throughout the mission.

2.7.4. Baseline sampling

The data model adopted by Hinshaw et al. (2003) can be written in raw du as

$$\mathbf{d} = \mathbf{GPBM} \mathbf{a} + \mathbf{n} + \mathbf{b}, \quad (46)$$

where \mathbf{b} is the instrumental baseline and \mathbf{n} is the total instrumental noise. As noted above, Commander3 divides the noise into $\mathbf{n} = \mathbf{n}^{\text{w}} + \mathbf{n}^{\text{corr}}$, a white noise term and a correlated noise term. Because the white noise is by definition uncorrelated in time, it does not have any correlations between adjacent pixels, so that

Table 1. COSMOGLOBE flagging statistics for each DA. The second column indicates the fraction of data that are removed by the official WMAP flags, while the third column indicates the fraction that is additionally discarded in the current processing for computational reasons. The fourth column indicates the total fraction of data actually used to generate the final maps.

Band	Flagged (%)	Discarded (%)	Used (%)
K	1.72	0.87	97.4
Ka	1.64	0.88	97.5
Q1	1.84	0.84	96.5
Q2	1.62	0.81	97.6
V1	1.62	1.10	97.3
V2	1.61	1.01	97.4
W1	1.76	1.03	97.2
W2	1.60	0.81	97.6
W3	1.61	0.87	97.5
W4	1.60	0.81	97.6

any pixel-pixel covariance should be fully described by realizations of the \mathbf{n}^{corr} timestream.

Commander3 estimates the baseline using the full estimate of the current sky model, $\mathbf{r} = \mathbf{d} - \mathbf{gs}^{\text{tot}} = \mathbf{b} + \mathbf{n}$. Modeling $\mathbf{b} = b_0 + b_1 \Delta t$, we solve for b_0 and b_1 using linear regression in each timestream while masking out samples that lie within the processing mask. Strictly speaking, this is breaking the Gibbs chain, as we are not formally sampling b_0 and b_1 for each TOD chunk. In practice, baseline estimation uncertainty propagates to correlated noise realizations and PSD parameters, as discussed below.

The approach detailed by Hinshaw et al. (2003) and the Commander3 implementation differ mainly in two ways. First, the assumed stable timescales are different – the initial WMAP baseline is estimated over one hour timescales, and assumed to be an actual constant, whereas Commander3 assumes constant values throughout the entire time chunk, which is 3–7 days depending on the band in question, but allows a linear term in the baseline. Second, the two methods differ in how they treat nonlinear residuals in the first-order baseline model. As noted by Hinshaw et al. (2003), residual baseline variations manifest as correlated noise stripes in the final maps, and WMAP9 solves this using a time-domain filter, downweighting the data based on the noise characterization. This is fundamentally similar to the Commander3 approach, which accounts for this as part of the correlated noise component. The main advantages of the latter is that it allows for proper error propagation at all angular scales without the use of a dense pixel-pixel noise covariance, and also that it provides a convenient means for inspecting the residuals visually by binning the correlated noise into a sky map.

3. Data and data processing

We describe the delivered WMAP data products in Sect. 3.1, then describe the treatment we apply to make them compatible with Commander3 in Sect. 3.2. Finally, we describe the computational requirements in Sect. 3.3.

3.1. Publicly available WMAP products

The full WMAP dataset is hosted at the Legacy Archive for Microwave Background Data Analysis (LAMBDA).⁴ In addition to

⁴ https://lambda.gsfc.nasa.gov/product/wmap/dr5/m_products.html

Table 2. Computational resources required for end-to-end COSMOGLOBE processing. All times correspond to CPU hours, and all data volumes are reported in GB. Reported times are averaged over more than 100 samples, and vary by $\lesssim 5\%$ from sample to sample. Note that the average cost per sample takes into account the undersampling of 70, V, and W.

ITEM	30	44	70	K	Ka	Q1	Q2	V1	V2	W1	W2	W3	W4	SUM	
<i>Data volume</i>															
Compressed TOD volume	86	178	597	13	12	15	15	19	18	26	26	26	26	1 053	
<i>Processing time (cost per run)</i>															
TOD initialization/IO time	1.8	2.5	7.8	0.7	0.6	0.8	0.7	0.9	0.8	1.3	1.3	1.0	0.9	21.1	
Other initialization														14.6	
Total initialization														35.7	
<i>Gibbs sampling steps (cost per sample)</i>															
Huffman decompression	1.2	2.2	23.2	0.8	0.9	1.1	1.1	1.5	1.4	2.0	2.0	2.0	2.0	41.4	
Array allocation	0.4	0.9	51.6	1.3	1.3	1.5	1.5	3.1	3.3	4.0	3.8	4.0	4.0	80.7	
TOD projection (P operation)	0.9	2.0	12.3	6.1	7.1	8.7	8.9	11.4	11.3	15.9	15.8	15.7	15.8	131.9	
Sidelobe evaluation	1.2	2.6	9.5	3.0	3.5	4.1	4.2	5.5	5.4	7.8	7.7	7.7	7.5	69.7	
Orbital dipole	0.9	2.0	9.0	1.2	1.5	1.8	1.9	2.6	2.5	3.8	3.8	3.8	3.8	38.6	
Gain sampling	0.6	0.9	2.2	1.3	1.3	0.8	0.8	1.3	1.3	1.2	1.2	1.2	1.2	15.3	
1 Hz spike sampling	0.3	0.4	1.9											2.7	
Correlated noise sampling	2.1	4.3	24.8	2.7	2.9	3.7	3.8	6.2	5.4	7.7	7.4	6.9	8.3	86.4	
Correlated noise PSD sampling	5.0	6.2	1.6	0.3	0.3	0.3	0.3	0.5	0.5	0.7	0.6	0.6	0.7	17.6	
TOD binning (P^t operation)	0.1	0.1	10.5	0.8	0.8	1.0	1.0	1.7	1.6	2.4	2.4	2.4	2.4	27.2	
Mapmaking						9.2	9.7	13.1	12.7	21.7	20.2	35.4	34.9	36.1	39.3
MPI load-balancing	1.2	1.7	9.2	2.2	2.0	2.2	2.1	3.6	3.3	4.8	4.6	4.5	4.6	46.0	
Sum of other TOD processing	0.7	1.6	13.1	0.1	0.2	0.5	0.4	0.7	0.8	0.9	1.0	0.9	1.2	22.1	
TOD processing cost per sample	14.6	24.9	169.7	28.8	31.5	38.7	38.7	59.8	57.0	86.6	85.2	85.8	90.8	812.1	
Amplitude sampling														16.2	
Spectral index sampling														32.1	
Average cost per sample														418.9	

the primary scientific products, e.g., cosmological parameters, CMB power spectra and anisotropy maps and frequency maps, the time-ordered data (TOD) can be downloaded, both in uncalibrated and calibrated form.⁵ In principle, thanks to these data and the explanatory supplements (Greason et al. 2012), the entire data analysis pipeline can be reproduced from TOD in digital units (du) to frequency maps.

For this analysis, we keep certain instrumental parameters fixed to the reported values. For example, we have made no attempts to rederive the pointing solutions, re-estimate the main beam response and far sidelobe pickup, or recover data that were flagged in the *WMAP* event log. These and other analyses, such as estimating the bandpass shift over the course of the mission, are certainly possible within the larger Gibbs sampling framework. However, in this work we limit ourselves to recalibrating the TOD, estimating the noise properties, and applying bandpass corrections to the data before mapmaking.

3.2. TOD preprocessing and data selection

The full nine-year *WMAP* archive spans from 10 August 2001 to 10 August 2010, with the raw uncalibrated data comprising 626 GB. A little over 1 % of the data were lost or rejected due to incomplete satellite telemetry, thermal disturbances, spacecraft anomalies, and station-keeping maneuvers, with an extra 0.1 % rejected due to planet flagging (Bennett et al. 2003b; Hinshaw et al. 2007, 2009; Bennett et al. 2013). The final results reported by Bennett et al. (2013) included roughly 98.4 % of the total data volume. A full accounting of all data cuts can be found in

Table 1.8 of Greason et al. (2012). In this analysis we flag the same data indicated in the fiducial *WMAP* analysis, and use the same planet flags.

As shown by Galloway et al. (2022a), a large fraction of Commander3’s computational time is spent performing Fast Fourier Transforms (FFTs) on individual scans. Rather than truncating datastreams to have lengths equal to “magic numbers” for which FFTW (Frigo & Johnson 2005) is fastest, as was done in the BEYONDPLANCK analysis, we redistribute the data into scans of length 2^N , where $N = 22$ for $K-Q$, $N = 23$ for $V-W$. This yields scans with lengths of 6.21 days for K - and Ka -band, 4.97 days for Q -band, 7.46 days for V -band, and 4.97 days for W -band.⁶ These datastream lengths are short enough to be processed quickly and distributed efficiently across multiple processors, while being long enough to properly characterize the noise properties of the timestreams, whose f_{knee} values are on the order 1 mHz. Most importantly, FFTW performs fastest when the datastream is of length 2^N .

When redistributing the data, timestreams of length 2^N were interrupted by events logged in Table 1.8 of Greason et al. (2012). When we encountered these events, interrupted TOD segments were appended to the previous TOD, in most cases creating TODs with lengths $> 2^N$. We found that events of length $< 2^N$ were too short to accurately estimate the noise PSD parameters. This criterion led us to discard these otherwise useful data. In addition, when $> 10\%$ of the TOD are flagged, the large number of gaps in the data makes the constrained realizations computationally more expensive. Given that data near many large gaps are more likely to have unmodeled effects than stable data, and

⁵ https://lambda.gsfc.nasa.gov/product/wmap/dr5/tod_info.html

⁶ Note that scans with equal n_{TOD} cover different lengths of time due to the different sampling rate for each frequency.

they are more expensive to process, we chose to remove these from the analysis. Together, these two effects led to $\simeq 1\%$ of the data to be discarded. We summarize the full flagging statistics for our maps in Table 1. In total, the COSMOGLOBE maps use about 1 % less data than the *WMAP9* official products. The total difference in data volume can be entirely accounted for by the cuts described in this paragraph.

3.3. Computational resources and future plans

A key motivation of the current analysis is to evaluate whether it is feasible to perform a joint analysis of two datasets simultaneously, each with its own particular processing requirements and algorithmic treatment. One of the results from Watts et al. (2022) was that most of the data processing procedures for *WMAP* and *Planck* LFI overlapped, with the notable exception of mapmaking. While the algorithmic requirements have been discussed in Sect. 2, we have not yet quantified the requirements in terms of RAM and CPU hours. In Table 2, we enumerate the RAM requirements and CPU time for each sampling step using a single AMD EPYC 7H12, 2.6 GHz cluster node with 128 cores and 2 TB of memory. As such, approximate wall runtimes can be obtained by dividing all numbers in Table 2 by 128.

Despite the relatively small data volume spanned by *WMAP*, the CPU time is comparable to each of the LFI channels. The single largest reason for this is the mapmaking step, which requires looping over the entire dataset for each matrix multiplication, a process which must be repeated ~ 20 times. As discussed in Sec. 2.7.2, this is vastly sped up by the use of a low resolution preconditioner, reducing the number of iterations by an order of magnitude.

Additionally, operations that require the creation of timestreams for each detector, i.e., TOD projection, sidelobe evaluation, and orbital dipole projection, take much longer than expected from a pure data volume scaling. Part of this is due to each *WMAP* radiometer needing to evaluate the sky in two pixels simultaneously, doubling the expected workload, but the other issue is that we are unable to benefit from the ring-clustering based TOD distribution scheme used for LFI. Due to *WMAP*'s more complex scan strategy and detector geometry, it is impossible to cluster scans with similar pixel coverage onto a single core, which makes pixel-space lookup operations less efficient in this case.

Gain sampling and correlated noise sampling include multiple FFTs. Typical LFI TODs are of length $\sim 200\,000$, an order of magnitude smaller than the *WMAP* TODs of length $\sim 5\,000\,000$. Despite the TOD lengths being pre-determined to be 2^N , this extra length still results in longer run times for equivalent data volumes, but does yield noise information on much longer time scales than we have for LFI.

For the current analysis, which aims primarily to derive posterior-based *WMAP* frequency maps, we produce a total of 500 main Gibbs samples, divided into two chains. Noting that the computational cost of the *W*-channel carries almost half of the total expense of the *WMAP* TOD processing, while being of less scientific importance than, say, the *K*-band, we choose to only reprocess this channel every fourth main sample. Likewise, we only reprocess the *V*-band every other main sample, and the LFI 70 GHz sample every fourth sample. The total cost for producing 500 *WMAP K, Ka, Q, Planck 30*, and 44 GHz samples, 250 *V*-band samples, and 125 *W*-band and 70 GHz samples is 210k CPU-hrs, and the total walltime is 33 days. Noting that the BEYONDPLANCK analysis required 4000 samples to reach full convergence in terms of the optical depth of reionization (Paradiso

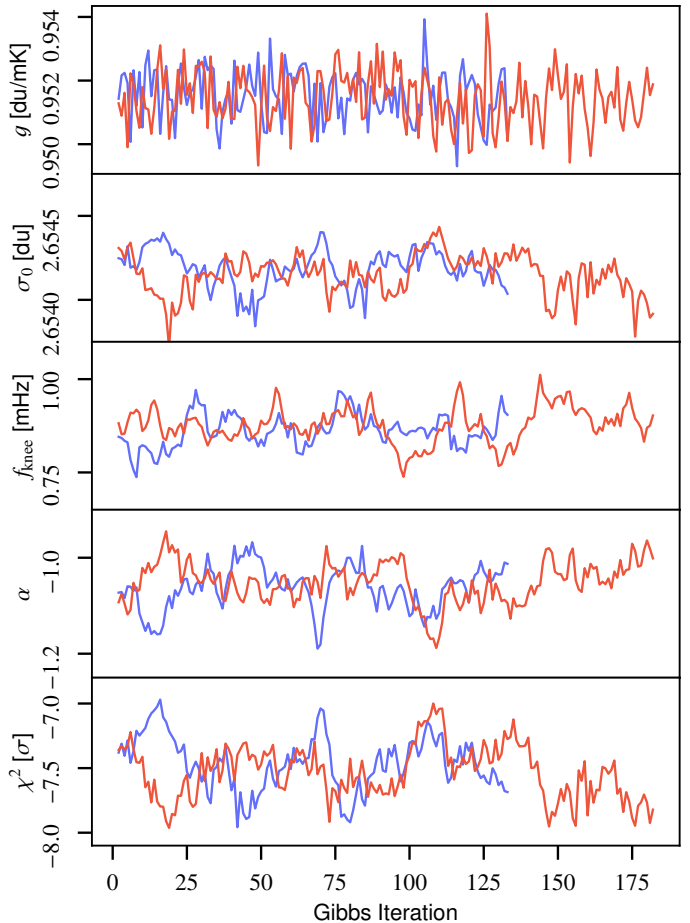


Fig. 3. Trace plots of the *K113* gain and noise parameters for a single scan starting on MJD 52285.2. The two colors correspond to the two independent Markov chains produced in this analysis.

et al. 2022), a corresponding complete LFI+*WMAP* analysis will cost about 1.7M CPU-hrs, and take about 9 months of continuous runtime on two cluster nodes. While entirely feasible, this is sufficiently expensive that we choose to perform the analysis in two stages; first we present preliminary frequency maps in the current paper, and use these to identify potential outstanding issues, either in terms of data model or Markov chain stability. An important goal of this phase is also to invite the larger community to study these preliminary maps, and thereby identify additional problems that we may have missed. Then, when all issues appear to have been resolved, we will restart the process, and generate sufficient samples to achieve full convergence.

4. Instrumental parameters

We are now ready to present the main results from the COSMOGLOBE DR1 analysis, which may be summarized in terms of the joint posterior distribution. For organizational purposes, we will discuss instrumental parameters, frequency maps, and astrophysical results separately in this and the following two sections, but it is important to remember that these results are all derived from one single highly multivariate posterior distribution, and every parameter is in principle correlated with all others. In this section, we focus on instrumental parameters, starting with visual inspection of the basic Markov chains and posterior means, before considering each instrumental parameter in turn.

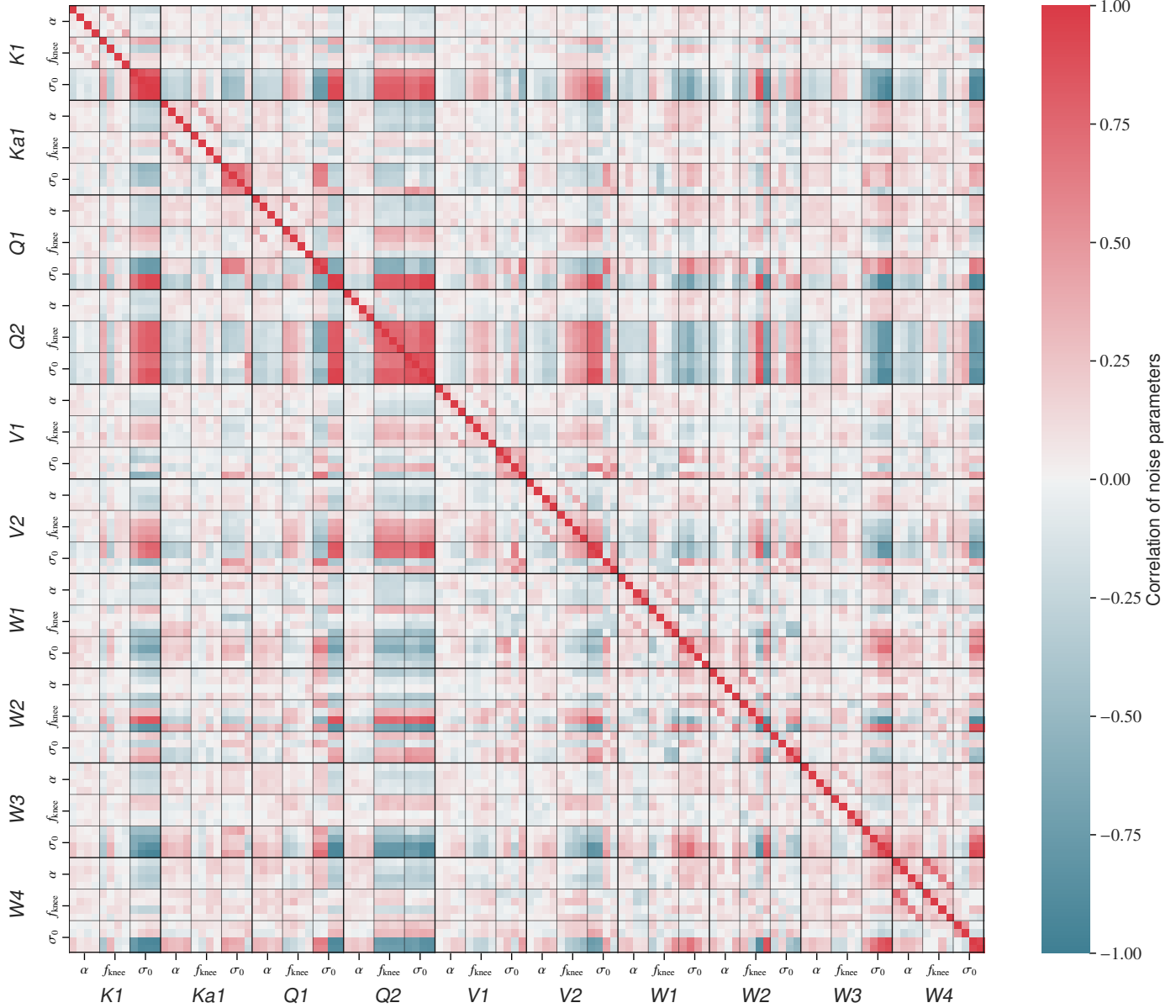


Fig. 4. Noise parameter correlation matrix. We average over all Gibbs samples of the noise parameters $\xi^n = \{\alpha, f_{\text{knee}}, \sigma_0\}$ for each PID. We then find the correlation in time between these averages for the different bands and detector. The results here are for the calibrated white noise level, σ_0 [mK]. The values for each detector are ordered 13, 14, 23, and 24.

4.1. Markov chains, correlations and posterior mean statistics

To build intuition regarding the general Markov chain properties, we show in Fig. 3 the Markov chains for the gain and noise parameters for one randomly selected diode ($K113$) and scan. Each panel corresponds to one single parameter, and the observed variation quantify the uncertainty in that single parameter due to the combination of white noise and correlations with other parameters. Here we immediately see that the different parameters have quite different correlation lengths; the gain (shown in the top panel) has a very short auto-correlation length, as in just a few samples, while the noise parameters have typical correlation lengths of a few tens of samples. Even for these parameters, however, the full set of 500 samples provides a fairly robust estimate of the full marginal mean and uncertainty.

The bottom panel shows the reduced normalized χ^2 for the same scan in units of σ , and we see that this also shows similar

correlation lengths as the noise parameters. This makes intuitive sense since the TOD residual at the level of a single-sample is strongly noise dominated. In contrast, small variations in either the sky signal or gain have relatively small impacts on this particular χ^2 ; the goodness of fit of such global parameters is better measured through map-level residuals and χ^2 's. In this respect, we also note that the absolute value of the TOD-level χ^2 is for this particular scan about -7.5σ , which at first sight appears as a major goodness of fit failure. However, it is important to recall that a typically scan contains about five million data points, and this statistic is therefore extremely sensitive to any deviation in the noise model. Specifically, the reduced χ^2 for this particular scan is $\chi^2_{\text{raw}}/n_{\text{tod}} = 0.993$, which corresponds to an over-estimation of the white noise level of only 0.3 %. Furthermore, as discussed in Sect. 2.7.1, we currently assume a strict $1/f$ noise model for the WMAP noise, while the true WMAP noise is known to exhibit a very slight non-white noise excess

at high frequencies (Watts et al. 2022). Properly modelling such non-white high-frequency noise is therefore an important goal for the next COSMOGLOBE data release. Such work is also a vital step in preparing for integration of other types of experiments with non-white noise into the framework, such as *Planck* HFI. However, in absolute terms, the impact of this model failure is very limited, and not likely to significantly affect any astrophysical results; it is primarily a limitation for TOD-level goodness of fit testing.

Going one step higher in complexity, Fig. 4 shows pairwise correlations between the various noise parameters for all DAs, averaged over all Gibbs samples and scans. It is important to note that a non-zero correlation in this plot does not indicate the that specific noise realization is correlated between DAs, but only that the noise PSD parameters are correlated. This is expected due to the *WMAP* satellite motion around the Sun, which induces an annual variation in the system temperature. This correlation plot therefore primarily quantifies the sensitivity to this common-mode signal for each radiometer. Most notably, we see that the *Q2* radiometer exhibits particularly strong correlations, and we also note that σ_0 is generally more susceptible to these variations than f_{knee} and α .

Next, in Fig. 5 we show posterior mean values for each instrumental parameter for the same *K113* diode, in this case plotted as a function of time throughout the entire mission. The panels show, from top to bottom, 1) gain; 2) the difference between the baseline mean and its full-mission average; 3) the baseline slope; 4) the white noise level; 5) the correlated noise knee frequency; 6) the correlated noise slope; and 7) the TOD-level χ^2 . The COSMOGLOBE results are shown as black curves, while the *WMAP* results are (for the gain and baseline) shown as red curves; dotted red and orange line corresponds to the first-year *WMAP* and Goddard Space Flight Center (GSFC) laboratory measurements, respectively. For brevity, we have only shown the results for one single diode here. However, a complete survey of all instrumental parameter posterior means for all 40 diodes is provided in Appendix A, and all individual samples are also available in a digital format as part of the COSMOGLOBE DR1.

4.2. Gain and baselines

We now consider the gain and baseline parameters in greater detail, and aim to compare our estimates with the *WMAP9* products. Unfortunately, the *WMAP9* gain and baseline estimates are not directly available in terms of easily accessible and public data products, but only in terms of the general parametric models. For instance, the *WMAP* gain model reads Greason et al. (2012)

$$g = \alpha \frac{\bar{V} - V_o - \beta(T_{\text{RXB}} - 290 \text{ K})}{T_{\text{FPA}} - T_o} + (m\Delta t + c), \quad (47)$$

where \bar{V} represents the radio frequency bias powers per detector; T_{RXB} and T_{FPA} are the receiver box and focal plane assembly temperatures, which are recorded every 23.04 s; α , V_o , β , T_o , m , and c are all free parameters that are fit to a constant value across the mission for each radiometer. Evaluating this model as a function of T_{RXB} and T_{FPA} requires the housekeeping data for the thermistor that was physically closest to the relevant radiometer's focal plane on the satellite. The free parameters are fully tabulated in the *WMAP* Explanatory Supplement (Greasor et al. 2012), but the physical layout of the thermistors in the focal plane is not readily available. We therefore do not attempt to reproduce the gain model given in Eq. (47).

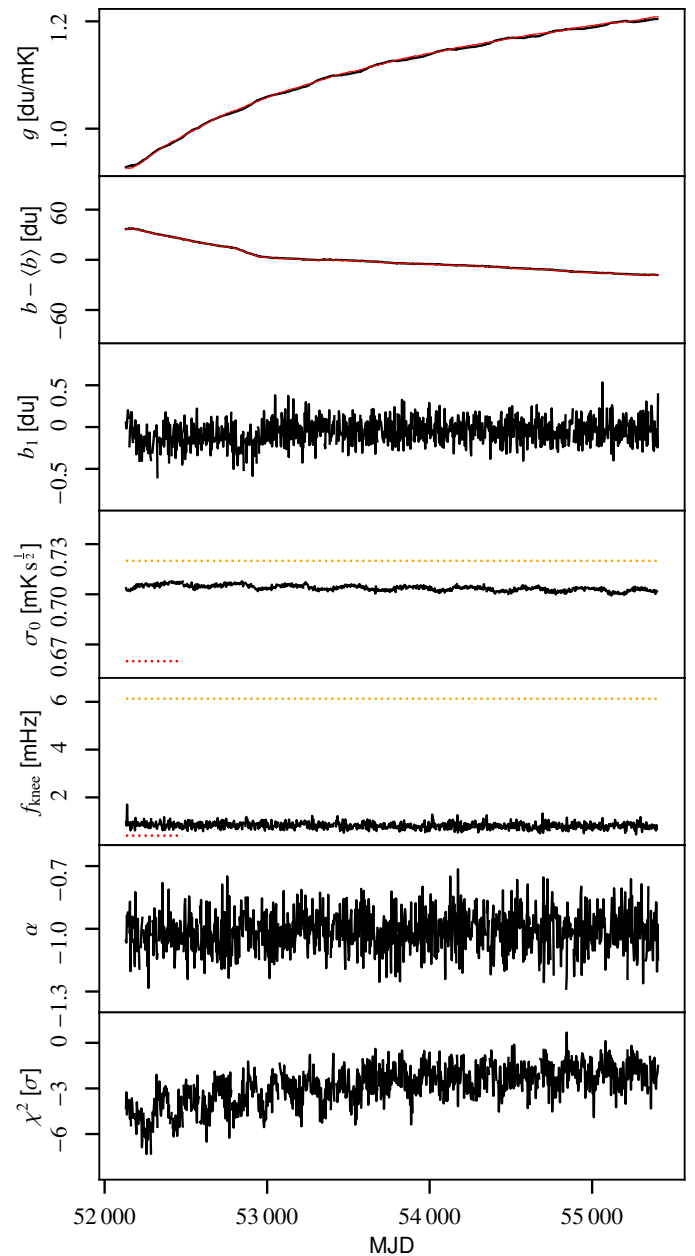


Fig. 5. Overview of *K113*. The red solid lines in first and second panel are the regressed gain and baseline from *WMAP9*, while the black lines in all panels are samples from the COSMOGLOBE Gibbs chain. The red dashed and yellow dashed lines are reported σ_0 and f_{knee} values from the first-year *WMAP* data analysis and GSFC measurements, respectively.

Rather, we estimate the gains and baselines by comparing the uncalibrated *WMAP* data with the calibrated *WMAP* data, after subtracting a far sidelobe contribution convolved with the delivered *WMAP9* DA maps plus the Solar dipole. We find that the calibrated and uncalibrated data can be related by

$$d_t^{\text{raw}} = g(d_t^{\text{cal}} + s_i^{\text{sl}}) + \sum_{i=0}^3 c_i(t - t_0)^i, \quad (48)$$

where the second term is a cubic polynomial with coefficients c_i referenced to the time at the beginning of the scan t_0 . The red curves in the top two panels of Fig. 5 correspond to these estimates. At least visually, the agreement between the *WMAP*

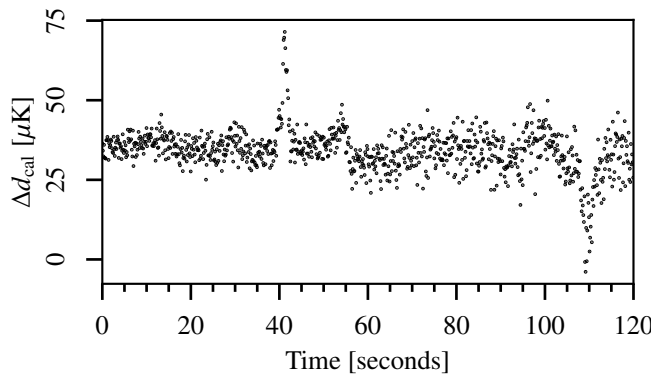


Fig. 6. Difference between the COSMOGLOBE $d_{\text{cal}} = d/g - b - s_{\text{sl}}$ and the delivered calibrated TOD from WMAP.

and COSMOGLOBE gain and baseline models appear reasonable at this level and for this diode.

A complete comparison between the WMAP and COSMOGLOBE gain and baseline models for all diodes is provided in Appendix A. In particular, Fig. A.1 shows the baseline differences as a function of time, and here we see that most diode differences scatter around a constant value that is close to zero; the precise constant value is of limited importance, since that only corresponds to a difference in the overall monopole of the maps, which for WMAP is determined through post-processing. However, there are a few notable features. First, we see that the two Q11 diodes exhibit large variations at the very beginning of the mission, with typical values of a few μK 's, and individual scans show notable spikes for many diodes. These are all relatively isolated in time, and will therefore have relatively minor impact on the final maps. Far more significant are the W-band differences, for which one sees both slow drifts and abrupt changes. Furthermore, in many cases they vary notably between diodes within the same DA, and this will obviously translate into differences in the large-scale polarization maps derived from the two pipelines.

Similarly, Fig. A.3 compares the gain solutions directly, while Fig. A.4 shows the fractional differences in units of percent. Overall, we see that the two gain models agree to typically about 0.5 % in an absolute sense, and better than typically 0.1 % in terms of relative agreement between neighboring scans. By far the most striking feature in this plot is an annual variation that traces the WMAP satellite's motion around the Sun. In general, such an oscillatory gain behaviour is entirely expected, because of known temperature variations in the satellite. However, the difficulty lies in estimating the magnitude of the oscillations, as different radiometers can respond differently to these temperature variations. In this respect, it is useful to recall that the WMAP and COSMOGLOBE gain estimation algorithms differ at a fundamental level; while the WMAP analysis considers each DA in isolation, and attempts to fit a handful of instrumental parameters, defined by Eq. (47), to the orbital dipole seen by each DA. The COSMOGLOBE analysis considers the problem globally, and attempts to fit all gain parameters to the full sky signal (including both the Solar and orbital CMB dipole) simultaneously, without the use of a strong instrumental model prior. Returning to the absolute gains shown in Fig. A.3, it is difficult to determine visually which approach is better at this level alone, as the two models are quite similar; in some cases, such as Ka124 and Q214, the WMAP model oscillates more strongly than the COSMOGLOBE model, while in others, such as K113 and K114, the opposite is true. We also see the impact of the strong instrumental

Table 3. Transmission imbalance parameters for each WMAP radiometer as estimated in the current analysis (*second column*) and in the official 9-year WMAP analysis (*third column*). Our uncertainties indicate 1σ marginal posterior standard deviations.

RADIOMETER	$x_{\text{im}}^{\text{CG}}$	$x_{\text{im}}^{\text{WMAP}}$
K11	0.00018 ± 0.00013	-0.00067 ± 0.00017
K12	0.00388 ± 0.00015	0.00536 ± 0.00014
Ka11	0.00339 ± 0.00012	0.00353 ± 0.00017
Ka12	0.00150 ± 0.00010	0.00154 ± 0.00008
Q11	0.00081 ± 0.00016	-0.00013 ± 0.00046
Q12	0.00517 ± 0.00027	0.00414 ± 0.00025
Q21	0.00985 ± 0.00042	0.00756 ± 0.00052
Q22	0.01235 ± 0.00011	0.00986 ± 0.00115
V11	0.00012 ± 0.00041	0.00053 ± 0.00020
V12	0.00212 ± 0.00089	0.00250 ± 0.00057
V21	0.00246 ± 0.00012	0.00352 ± 0.00033
V22	0.00323 ± 0.00070	0.00245 ± 0.00098
W11	0.01169 ± 0.00105	0.01134 ± 0.00199
W12	0.00442 ± 0.00109	0.00173 ± 0.00036
W21	0.01595 ± 0.00052	0.01017 ± 0.00216
W22	0.01540 ± 0.00167	0.01142 ± 0.00121
W31	-0.00089 ± 0.00010	-0.00122 ± 0.00062
W32	0.00354 ± 0.00084	0.00463 ± 0.00041
W41	0.02734 ± 0.00219	0.02311 ± 0.00380
W42	0.01882 ± 0.00282	0.02054 ± 0.00202

priors in the WMAP solution particularly well in W-band, where the COSMOGLOBE gains are far more noisy than the WMAP gains.

The impact of these differences at the TOD level is illustrated in Fig. 6, which shows the calibrated COSMOGLOBE timestream $d/g - s_{\text{sl}}$ minus the WMAP calibrated signal in units of microkelvin. The most prominent feature is a $\sim 25 \mu\text{K}$ offset, which is unsurprising, given the different treatment of baselines in our two pipelines. The second obvious difference is a series of spikes associated with Galactic plane crossings. Differences of order $50 \mu\text{K}$ are seen where the absolute sky brightness is about 10 mK , and this is equivalent to $\sim 0.5\%$ deviations in the gain solution. This is twice as large as the 0.2% uncertainty estimated in Bennett et al. (2013) based on end-to-end simulations.

Another interesting feature in Fig. 6 is slow correlated variations at a timescale of ~ 20 sec timescale. There is nothing in the COSMOGLOBE instrument model that varies on such short timescales, and this must therefore come from WMAP. The most likely explanation is the fact that the the WMAP gain model depends directly on housekeeping data that are recorded with a 23.04 sec sample rate, and these values appear to have been applied without any smoothing, resulting in sharp jumps in the final WMAP gain model. At the same time, it is also important to note that the COSMOGLOBE gain model does not include any time-varying structure within a single scan, and if any artifacts resulting from this are identified in the current products, it may be worth incorporating housekeeping data in a future COSMOGLOBE data release.

4.3. Transmission imbalance

Closely related to the gain model is the transmission imbalance factor, x_{im} , quantifying the difference between responsivity in the two horns, as described in Sect. 2.2. These are listed for each radiometer in Table 3 for both COSMOGLOBE and WMAP9; for COSMOGLOBE the reported values correspond to marginal posterior means and standard deviations. The same information is plotted in Fig. 7.

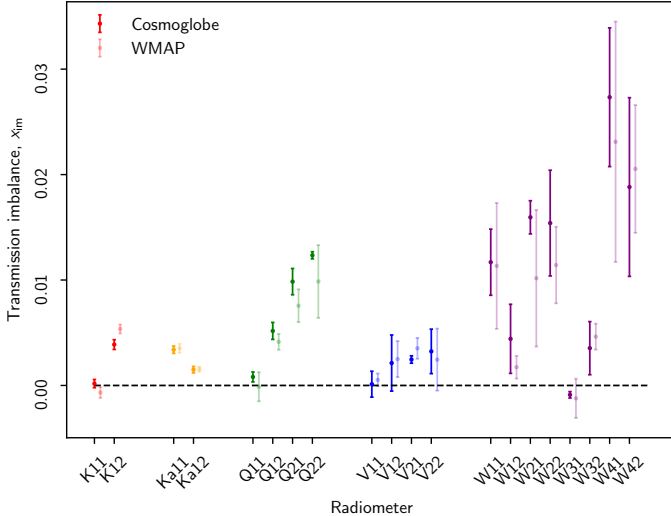


Fig. 7. Comparison of the transmission imbalance factors, x_{im} , estimated by COSMOGLOBE (dark colors) and WMAP9 (light colors) for each radiometer.

At first glance, the two estimates appear in reasonable agreement, and except for K -band, they are always within 1σ from each other. However, there are subtle differences that could play an important role in the final maps and uncertainty estimates. The reason for this is that these parameters couple directly to the astrophysical sky signal, and in particular to the bright 3 mK Solar CMB dipole. Even an inaccuracy at the $O(10^{-3})$ level can therefore in principle excite correlated large scale artifacts at the microkelvin level, which is comparable to, or larger than, the expected cosmological reionization of about $0.5\mu\text{K}$.

With this in mind, we first note that the K -band imbalance factors differ by $2\text{--}3\sigma$. For this particular channel, it is important to note both that the foregrounds are very bright and that the effective bandpass of each radiometer differ. Minor details in both foreground and bandpass modelling are therefore likely to have a significant impact of the estimated parameters.

Second, we see that for many several channels, the two methods disagree strongly on the marginal uncertainties. For instance, the WMAP $Q22$ uncertainty is about a factor of ten larger than the COSMOGLOBE uncertainty, and the corresponding mean differs from the COSMOGLOBE mean by about 8σ as measured in units of COSMOGLOBE uncertainties. These differences are important both in terms of final sky maps (which depend on the mean value) and error propagation. In particular, it is important to note that while the COSMOGLOBE sampling approach accounts for all couplings between the specific value of x_{im} and all other parameters (gain, baselines, correlated noise, CMB dipole, large scale polarization, etc.) at every single step of the Markov chain, the WMAP approach only marginalizes over two linear templates in the low-resolution covariance matrix. These two templates are derived by changing x_{im} by respectively 10 and 20 % with respect to their mean values, respectively, and recomputing the maps. This linear low resolution approach can only capture a limited subvolume of the full nonlinear effect of transmission imbalance uncertainties. Even cases for which the mean estimates formally agree within 1σ may therefore in practice result in significantly different sky maps. We will return to this issue in Sect. 5.

4.4. Instrumental noise

Next, we consider the instrumental noise parameters, $\xi_n = \{\sigma_0, f_{\text{knee}}, \alpha\}$. In this case, we recall three major differences between the COSMOGLOBE and WMAP analysis. First, while we model the noise explicitly with a $1/f$ noise profile in Fourier domain, the WMAP analysis adopts a model independent approach by simply measuring the autocorrelation function directly. A notable advantage of the latter approach is that it naturally accounts for the non-white noise at high frequency without algorithmic modifications, while this has to be added manually in the parametric COSMOGLOBE approach. A second difference is the fact that while WMAP uses 1- or 24-hour segments to estimate the noise model, we use 3–5 days, and are therefore able to trace noise correlations to longer timescales. Thirdly, while WMAP assumed the noise filter to be constant within each year of operations, we allow it to vary between scans, that is, on a timescale of days.

With these differences in mind, Figs. A.5–A.7 provides a complete overview of the noise parameters for all 40 WMAP diodes. As in Fig. 5, the solid black lines show COSMOGLOBE results, while the dotted red and orange lines show the corresponding 1-year and GSFC measurements (where available). Starting with the white noise level, we see that these are overall relatively constant in time, although with slight traces for annual variations in some channels (e.g., $K113$); slight instabilities near the beginning and/or end of the mission in other channels (e.g., Ka); and slight drifts in yet others (e.g., $Q12$ and $W32$).

When comparing the COSMOGLOBE values with the WMAP values, it is worth noting that WMAP only published results for each diode-pair, not for individual diodes. All WMAP values are therefore the same for each diode pair. Still, from the COSMOGLOBE results, which are reported individually for each diode, we see that diode pairs generally have quite similar white noise levels and vary at most by a percent.

To facilitate a more quantitative comparison, Table 4 compares the COSMOGLOBE posterior mean results with the reported WMAP results. Note that for σ_0 , the COSMOGLOBE values have been scaled by a factor of $\sqrt{2}$, in order to account for the fact that these apply to individual diodes, as opposed to diode-pairs. Both in Table 4 and Fig. A.5, we see that about half of the COSMOGLOBE values lie between the two WMAP results, while the other half are higher. In particular the W -band noise levels are much higher in the COSMOGLOBE solution, sometimes by as much as 50 %.

In this respect, it is worth recalling from Sect. 2.7.1 that the white noise level in raw du is in COSMOGLOBE not strictly sampled from the full posterior distribution, but rather estimated deterministically from the highest frequencies. This makes our estimate more sensitive to possible colored noise at high frequencies (Watts et al. 2022). At the same time, the calibrated white noise level $\sigma_0[V] = \sigma_0[du]/g$ depends on the gain, and this allows us to test the effects of the calibration on the instrument sensitivity itself. The calibrated white noise level follows a biannual trend indicative of a system temperature variation, which is to be expected given the radiometer equation

$$\sigma_0[V] \propto gT_{\text{sys}}. \quad (49)$$

Aside from an overall amplitude shift due to the absolute calibration variation, the shape of the white noise level is stable throughout the Gibbs chain.

Another issue worth pointing out is the fact that we are not yet accounting for correlations between the white noise in diode pairs. However, these are write something more here.

Table 4. Summary of noise properties.

Radiometer ..	Diode	Sensitivity, σ_0 (mK \sqrt{s})			Knee frequency, f_{knee} (mHz)			Slope, α
		GSFC	WMAP	$CG/\sqrt{2}$	GSFC	WMAP	$CG/\sqrt{2}$	
<i>K</i> 11	1	0.72	0.66	0.704 ± 0.002	6.13	0.4	0.82 ± 0.20	-1.01 ± 0.10
	2			0.708 ± 0.003			0.63 ± 0.14	-0.95 ± 0.10
<i>K</i> 12	1	0.87	0.75	0.796 ± 0.004	5.37	0.51	0.42 ± 0.19	-0.93 ± 0.12
	2			0.780 ± 0.005			0.71 ± 0.15	-1.02 ± 0.10
<i>Ka</i> 11	1	0.75	0.71	0.788 ± 0.001	1.66	0.71	1.20 ± 0.22	-1.02 ± 0.09
	2			0.777 ± 0.001			1.19 ± 0.22	-1.02 ± 0.09
<i>Ka</i> 12	1	0.77	0.72	0.788 ± 0.003	1.29	0.32	0.62 ± 0.16	-0.99 ± 0.11
	2			0.784 ± 0.001			0.63 ± 0.13	-1.01 ± 0.11
<i>Q</i> 11	1	0.99	0.92	0.998 ± 0.002	3.21	1.09	1.06 ± 0.16	-1.09 ± 0.09
	2			0.992 ± 0.002			1.06 ± 0.16	-1.10 ± 0.09
<i>Q</i> 12	1	0.95	1.02	1.159 ± 0.007	3.13	0.35	0.45 ± 0.47	-0.98 ± 0.11
	2			1.146 ± 0.007			0.83 ± 0.14	-1.00 ± 0.09
<i>Q</i> 21	1	0.89	0.85	0.908 ± 0.002	1.92	5.76	2.88 ± 0.37	-1.10 ± 0.07
	2			0.906 ± 0.002			3.22 ± 0.56	-1.10 ± 0.06
<i>Q</i> 22	1	1.04	0.99	1.074 ± 0.004	4.61	8.62	3.95 ± 0.54	-1.11 ± 0.06
	2			1.064 ± 0.003			4.05 ± 0.64	-1.11 ± 0.06
<i>V</i> 11	1	1.25	1.22	1.551 ± 0.003	2.56	0.09	1.27 ± 0.15	-0.90 ± 0.06
	2			1.539 ± 0.003			1.19 ± 0.14	-0.89 ± 0.06
<i>V</i> 12	1	1.07	1.11	1.398 ± 0.002	4.49	1.41	2.11 ± 0.20	-0.97 ± 0.05
	2			1.432 ± 0.002			1.88 ± 0.17	-0.96 ± 0.05
<i>V</i> 21	1	1.01	0.97	1.241 ± 0.298	2.43	0.88	1.50 ± 0.24	-0.95 ± 0.07
	2			1.217 ± 0.294			1.60 ± 0.26	-0.97 ± 0.06
<i>V</i> 22	1	1.13	1.1	1.443 ± 0.300	3.06	8.35	4.01 ± 0.85	-1.00 ± 0.08
	2			1.415 ± 0.316			3.08 ± 0.65	-1.01 ± 0.08
<i>W</i> 11	1	1.18	1.35	1.938 ± 0.005	16.2	7.88	5.59 ± 0.53	-0.94 ± 0.05
	2			1.895 ± 0.005			8.99 ± 0.85	-0.95 ± 0.04
<i>W</i> 12	1	1.41	1.61	2.301 ± 0.005	15.1	0.66	3.91 ± 0.42	-0.89 ± 0.05
	2			2.345 ± 0.006			4.81 ± 0.53	-0.89 ± 0.05
<i>W</i> 21	1	1.38	1.61	2.225 ± 0.007	1.76	9.02	13.57 ± 1.47	-0.89 ± 0.03
	2			2.292 ± 0.006			5.06 ± 0.95	-0.93 ± 0.05
<i>W</i> 22	1	1.44	1.72	2.291 ± 0.006	0.77	7.47	3.02 ± 0.53	-0.98 ± 0.05
	2			2.232 ± 0.007			7.26 ± 1.05	-0.95 ± 0.04
<i>W</i> 31	1	1.47	1.65	2.328 ± 0.005	1.84	0.93	1.30 ± 0.46	-0.99 ± 0.07
	2			2.322 ± 0.006			1.97 ± 0.28	-0.98 ± 0.06
<i>W</i> 32	1	1.69	1.86	2.707 ± 0.015	2.39	0.28	1.59 ± 0.29	-0.98 ± 0.07
	2			2.579 ± 0.015			1.40 ± 0.39	-1.00 ± 0.07
<i>W</i> 41	1	1.6	1.71	2.519 ± 0.010	8.46	46.5	26.81 ± 1.83	-0.92 ± 0.04
	2			2.479 ± 0.009			24.75 ± 1.63	-0.92 ± 0.04
<i>W</i> 42	1	1.43	1.65	2.221 ± 0.017	5.31	26.0	16.10 ± 1.09	-0.94 ± 0.04
	2			2.202 ± 0.015			17.11 ± 1.19	-0.94 ± 0.04

In summary, we have not yet been able to identify the cause of the major difference in reported white noise levels at *W*-band; while we do detect goodness of fit failures of as much as $5-10\sigma$ for many of these diodes at the TOD level (see Sect. 4.1), such significances correspond to sub-percent errors in the white noise level. For comparison, a white noise misestimation of 50% would translate into an $800\sigma\chi^2$ failure. This is left to be understood through future work, but we do not expect it to indicate a real failure in either analysis, but it is more likely just a matter of different conventions.

Turning our attention to the low frequency parameters, we see in Table 4 and Fig. A.6 that our knee frequencies lie between the *WMAP* ground and laboratory measurements, almost without exception, which on the one hand indicates generally good agreement between the two analyses. However, on the other hand, it also implies that our values are in fact closer to the *WMAP* laboratory measurements than the *WMAP* flight measurements. This may possibly be due to the longer time-scales used in the COSMOGLOBE analysis.

Most radiometers have constant f_{knee} throughout the mission, with a few notable exceptions. First, all *W*-band channels display some amount of temporal variation that does not seem to be associated with any sinusoidal features. Second, all *Q*2 channels, *V*223, and *V*224 all display a similar asymptotic drift in time. We have not found any instrumental effects that share this feature. The PSD slope α is around -1 for each radiometer, albeit with high scatter for the lower frequencies. As expected, the uncertainty in α decreases as f_{knee} increases, since there are more datapoints to fit below f_{knee} where the constraining power on α is the strongest.

For completeness, Fig. A.8 shows a summary of the reduced normalized χ^2 for all diodes. The most striking features in these figures are the amplitude and semiannual periodicity. Given the noise model and data residual, we can evaluate the goodness of fit in the form of the relative χ^2 . Here, we find that approximately half of the radiometers have a χ^2 value at least 6σ above or below the expected value. Given perfect Gaussian residuals, we would expect these values to be within $\pm 1\sigma$ 68% of the

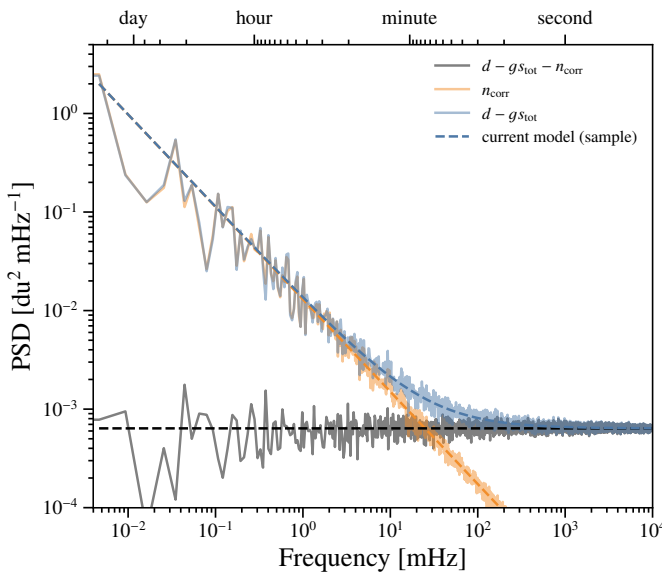


Fig. 8. PSD for radiometer W413 that spans MJDs 52252.3–52254.8. The power spectrum of the blue line corresponds to the residual, while the gray line is the residual with a correlated noise realization removed.

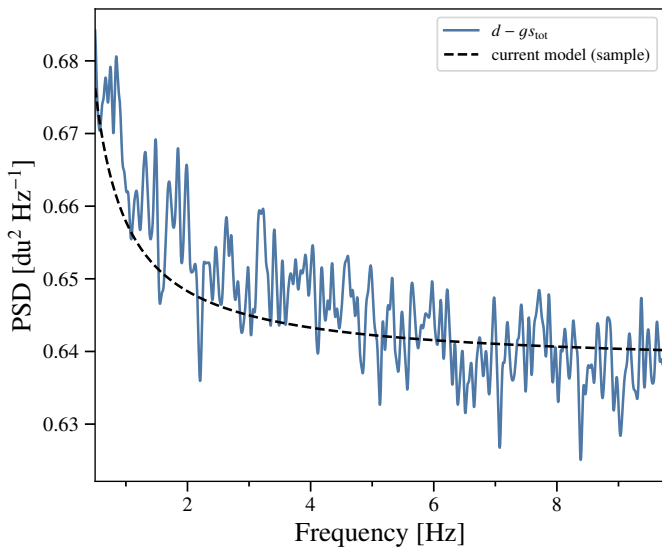


Fig. 9. PSD for radiometer W413 that spans MJDs 52252.3–52254.8. The black dashed line is a sample of the theoretical PSD, while the blue line is the smoothed residual power spectrum.

time. For a typical W -band scan of length $n_{\text{TOD}} = 2^{22}$, a 10σ model failure corresponds to $\chi^2/n_{\text{TOD}} = 1.003$. It is therefore exceedingly difficult to look at any given $WMAP$ scan in the time domain and identify a model failure. To illustrate this, Fig. 8 compares the observed noise PSD with the best-fit model for the W413 diode. This is a 7σ outlier; despite this, the $1/f$ model appears to perform exceedingly well over seven decades in frequency.

Only with aggressive smoothing does the model failure become apparent at frequencies 1–10 Hz. This is illustrated in Fig. 9, which shows exactly the same underlying data as in Fig. 8, but heavily smoothed. Here, it is clear that despite fitting the data well at the highest and lowest frequencies, it is in the intermediate range of 1–5 Hz where the $1/f$ model is a less accurate fit to the residual power spectrum. Part of the cause of

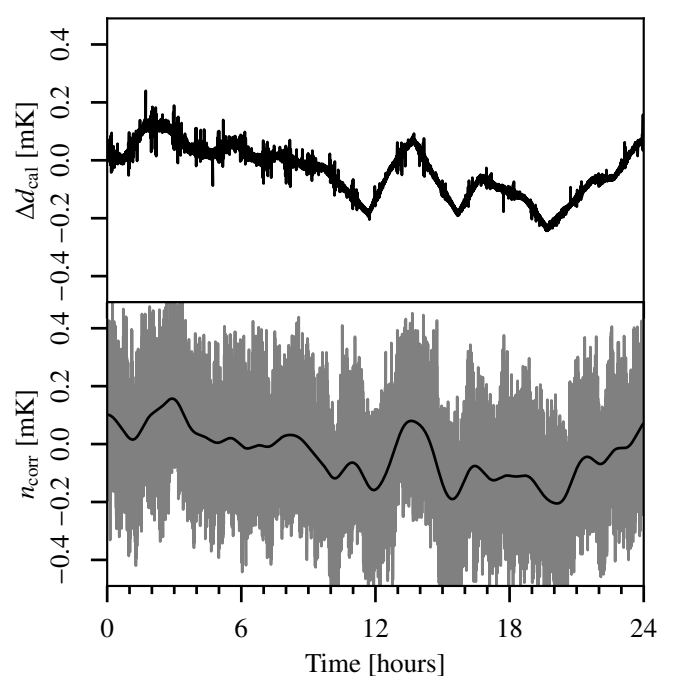


Fig. 10. (top): Difference between the COSMOGLobe $d_{\text{cal}} = d/g - \mathbf{b} - \mathbf{s}_{\text{sl}}$ and the delivered calibrated TOD from $WMAP$. (Bottom): Raw correlated noise (gray) and smoothed data with Gaussian kernel (black). This shows the hourly baseline subtraction from the $WMAP$ treatment.

this failure is that the white noise level is essentially fixed by the value of the power spectrum at the Nyquist frequency, as it was computed by differencing adjacent samples. The power spectrum has a downward trend beyond above 1 Hz, indicating that the data would be better fit by one or more terms proportional to f^α . This is phenomenologically similar to the $WMAP$ collaboration’s approach of describing the time-space autocorrelation as a cubic polynomial in $\log \Delta t$ (Jarosik et al. 2007).

In practice, the $1/f$ model has a small effect on the final data products, and was not visible in noise models when we modeled the data in one day scans rather than the longer 3–7 day scans due to the lower n_{TOD} giving a higher uncertainty on the relative χ^2 . Therefore, although this strictly constitutes a deficiency in the model, it is in practice too small to affect the results of the rest of the chain. The downturn of the noise PSD at high frequencies is also present in, e.g., the *Planck* HFI data (Planck Collaboration Int. XLVI 2016, Fig. 1), so improved modeling of this form will be a necessity in future COSMOGLobe endeavors, and will be used to improve the $WMAP$ data processing.

Before concluding this section, we recall the close relationship between the correlated noise component and the baseline model. This is illustrated in Fig. 10, which shows the difference between the calibrated COSMOGLobe and $WMAP$ TOD data, i.e., the same as Fig. 6, but plotted for 24 hours instead of 10 minutes. The bottom panel shows the COSMOGLobe correlated noise realization for the same period, both raw and smoothed. The most prominent feature in this figure is a varying signal of amplitude 0.2 mK. This is due to the hourly baseline subtraction mentioned above, which contrasts with the COSMOGLobe approach of assigning a linear baseline solution for the entire scan, and then accounting for the nonlinearity through \mathbf{n}^{corr} . The variations are commensurate with the correlated noise correlation length, which for K113 has $f_{\text{knee}} \sim 0.5$ mHz, corresponding to a little over half an hour. Therefore, the hourlong baseline subtrac-

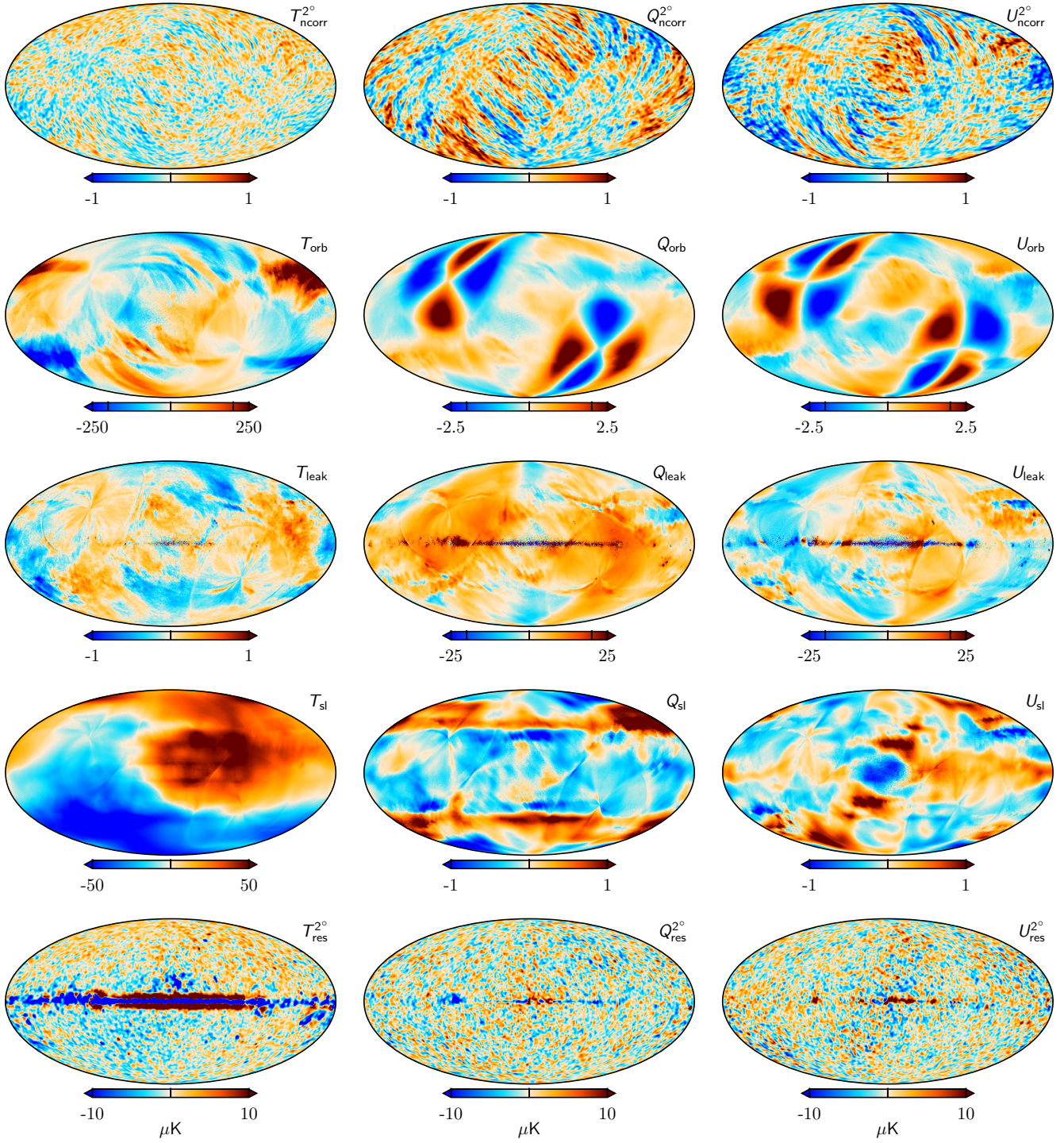


Fig. 11. TOD corrections for K -band for a single Gibbs sample, projected into maps. Columns show Stokes T , Q , and U parameters. Rows show, from top to bottom, 1) correlated noise; 2) the orbital dipole; 3) bandpass mismatch leakage; and 4) sidelobe corrections. The bottom row shows the residual obtained when binning the sky and systematics-subtracted TOD into a sky map. Note that the correlated noise and residual have been smoothed by a 2° Gaussian beam.

tion essentially acts as a destriper, removing an estimate of the correlated noise.

4.5. Instrumental corrections in map domain

Returning to the global parametric data model in Eq. (6), it is useful for intuition purposes to project each of the *WMAP* TOD-level correction terms into sky maps. This is done for K -band

in Fig. 11, in the same form as was done for LFI by [Basyrov et al. \(2022\)](#). Columns correspond to Stokes T , Q , and U parameters, while rows show, from top to bottom, 1) correlated noise; 2) the orbital CMB dipole; 3) bandpass leakage; and 4) sidelobe corrections. The bottom row shows the residual obtained after subtracting all modelled terms from the raw TOD. All maps correspond to one single and randomly selected Gibbs sample.

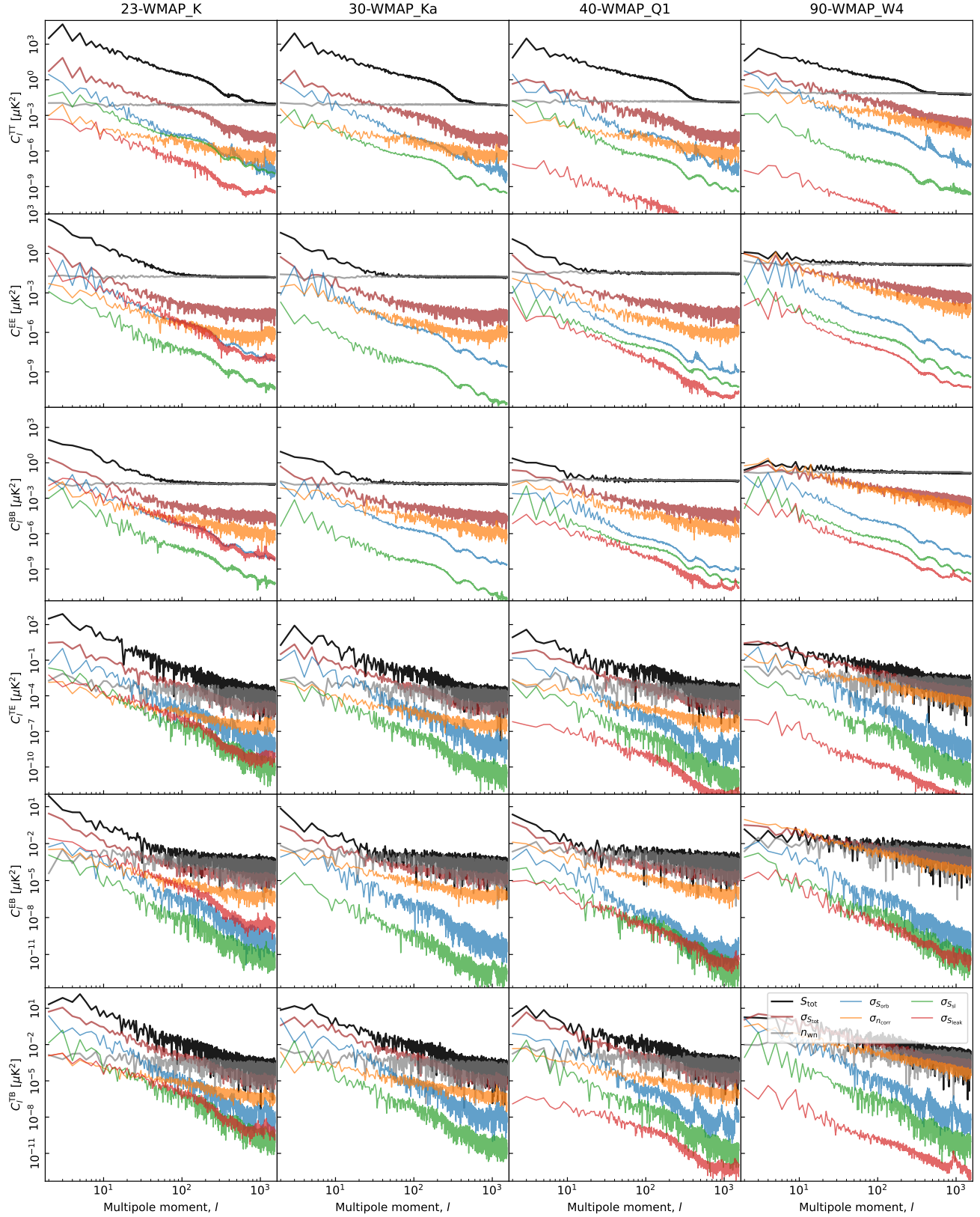


Fig. 12. Pseudo-spectrum standard deviation for each instrumental systematic correction shown in Fig. 11 (thin colored lines). For comparison, thick black lines show spectra for the mean of the full frequency map; thick red lines show their standard deviations (i.e., the full systematic uncertainty); and gray lines show white noise realizations. Columns show results for K , Ka , $Q1$, and $W4$, respectively, while rows show results for each of the six polarization states (TT , EE , BB , TE , TB , and EB). All spectra have been derived outside the CMB confidence mask presented by Andersen et al. (2022) using the HEALPix anafast utility, correcting only for sky fraction and not for mask mode coupling.

Starting with the correlated noise in the top row and the residual in the bottom row, we note that these are the only terms that are fundamentally stochastic in nature; all the other terms are primarily deterministic in nature, as they rely only on the sky model coupled to a small number of instrumental parameters, such as the gain, bandpass, or beam. As such, the correlated noise and residual maps essentially act as the “trash cans” of Bayesian CMB analysis; together they show anything in the TOD that is not explicitly modelled. For the K -band channel, we see that the correlated noise is limited to less than $1 \mu\text{K}$ over almost the full sky, while the residual appears like random noise over most of the sky. The main exceptions to this are strong residuals near the Galactic plane in temperature, which indicates the presence of unmodelled foreground features; typical candidates to explain this would be curvature in the synchrotron spectral index or a more complicated AME SED than that assumed here. Secondly, at high latitudes we see traces of a small dipole with an amplitude of $1\text{--}2 \mu\text{K}$ aligned with the CMB dipole. This indicates the presence of an absolute calibration deviation of about 0.03–0.06 %; this is within the uncertainty of the absolute K -band calibration prior of 0.1 % discussed in Sect. 2.5, and when inspecting different Markov chain samples of the same type, one can see that the amplitude and sign of this residual scatter around zero as expected.

Next, the amplitude of the orbital dipole is about $250 \mu\text{K}$ in temperature and $2.5 \mu\text{K}$ in polarization. This component by itself exceedingly well known, as it depends only on the satellite velocity and the CMB monopole temperature. However, when actually fitting this to the real data, it obviously also depends on both the gain, and sample-to-sample variations in this map is therefore a good tracer of gain uncertainties. In addition, its physical appearance also in principle depends on the sidelobe model, but we do not yet propagate sidelobe uncertainties anywhere in the analysis.

The third row shows the corrections for bandpass leakage. (In principle, this also accounts for leakage due to beam differences, as discussed by Svalheim et al. (2022a), but for *WMAP* this effect is much smaller than the bandpass effect.) As for *Planck* LFI, this term is by far the largest correction in polarization, with an amplitude that is almost an order of magnitude larger than any of the others. It is highly non-trivial to compare this component to the *WMAP9* analysis, since this effect was accounted for by solving for a spurious S map as part of their mapmaking. However, it is important to note that whether one models this effect explicitly, as we do, or project it out during mapmaking, as the *WMAP* pipeline did, the accuracy of the bandpass correction depend directly on the accuracy of the gain and transmission imbalance calibration.

The fourth row shows the sidelobe contribution. Here we see that the temperature amplitude reaches $50 \mu\text{K}$, which corresponds to 1.5 % of the CMB Solar dipole amplitude. If it should turn out that the sidelobe model were incorrect by, say, 30 %, this translates directly into an error in the absolute K -band calibration of about 0.5 %, which is significantly greater than the statistical error shown above. Given the degeneracies discussed in Sect. 2.5, there is thus also a strong degeneracy between the AME dipole and the K -band sidelobe. For polarization, the amplitude is mostly smaller than $1 \mu\text{K}$, and therefore of minor importance for this channel. We note that only the intensity component of the *WMAP* sidelobe model has been published, and polarized sidelobes are not accounted for in the current processing. However, as shown by Barnes et al. (2003)’s Table 2, the amplitude of this contribution is relatively small, with a high-

latitude mean of $0.8 \mu\text{K}$ for K -band and $< 0.1 \mu\text{K}$ for all other bands.

4.6. Instrumental uncertainties in power spectrum domain

We conclude this section by estimating the uncertainty of each instrumental effect in terms of angular power spectra, using the same methodology as Basyrov et al. (2022) for *Planck* LFI. That is, we first compute the power spectra for each individual instrumental correction Markov chain sample, as illustrated in Fig. 11, and the compute the standard deviation of all these samples. The results from this computation are summarized in Fig. 12 for four DAs, namely K , Ka , $Q1$, and $W4$. In each panel the black line shows the power spectrum of the full co-added frequency sky map (including both signal and noise), while the gray line shows the white noise level. The thick dark red line shows the sum of all variations, while the thin colored lines show the contribution from individual correction terms.

On large angular scales in the TT spectrum, we see that the dominant uncertainty comes from the orbital dipole (blue lines), which essentially trace gain uncertainties. This makes intuitive sense, since these data are strongly signal-dominated; indeed, for K -band even the sidelobe contribution (green lines) is higher than the correlated noise.

For large-scale EE polarization, the dominant term varies from channel to channel. Specifically, for K -band the bandpass leakage (thin red lines) and gain fluctuations are significantly larger than the correlated noise, while for $Q1$ and W -band the correlated noise dominates for most multipoles, although the gain fluctuations are comparable for some ℓ ’s.

An important conclusion to be drawn from these measurements is that a simple uncertainty model that primarily accounts for correlated noise is likely to be suboptimal for detailed cosmological analysis of large-scale polarization. Both gain and bandpass uncertainties are at least as important for the lowest multipoles, and simultaneously accounting for all of these contributions is important in order to derive robust cosmological results.

5. Frequency maps

In this section, we discuss the reprocessed *WMAP* frequency maps and their properties. In Sect. 5.1 we present the reprocessed *WMAP* maps themselves, commenting on notable features. In Sect. ?? we compare the properties of the individual DAs with the published *WMAP9* results, while we in Sect. 5.2 focus on the consistency of our new maps, both internally among the *WMAP* channels, and with respect to *Planck*. Section 5.3 describes the efficiency of template-based transmission imbalance uncertainty propagation.

5.1. Map survey

We start by showing the co-added frequency K -band, Ka -band, Q -band, V -band, and W -band posterior mean maps in Figs. 13–17, all defined in thermodynamic μK_{CMB} units. All maps are inherently produced at the DA level, and in these figures the Q , V , and W -band maps are generated by inverse-variance weighting the individual DAs. The temperature maps are presented at full angular resolution, while the polarization maps have been smoothed with a 2° Gaussian beam. Overall, the temperature maps behave as expected from the official *WMAP* analysis, with falling foreground amplitudes with frequency. Furthermore, it is very difficult indeed, if not impossible, to see visual differences

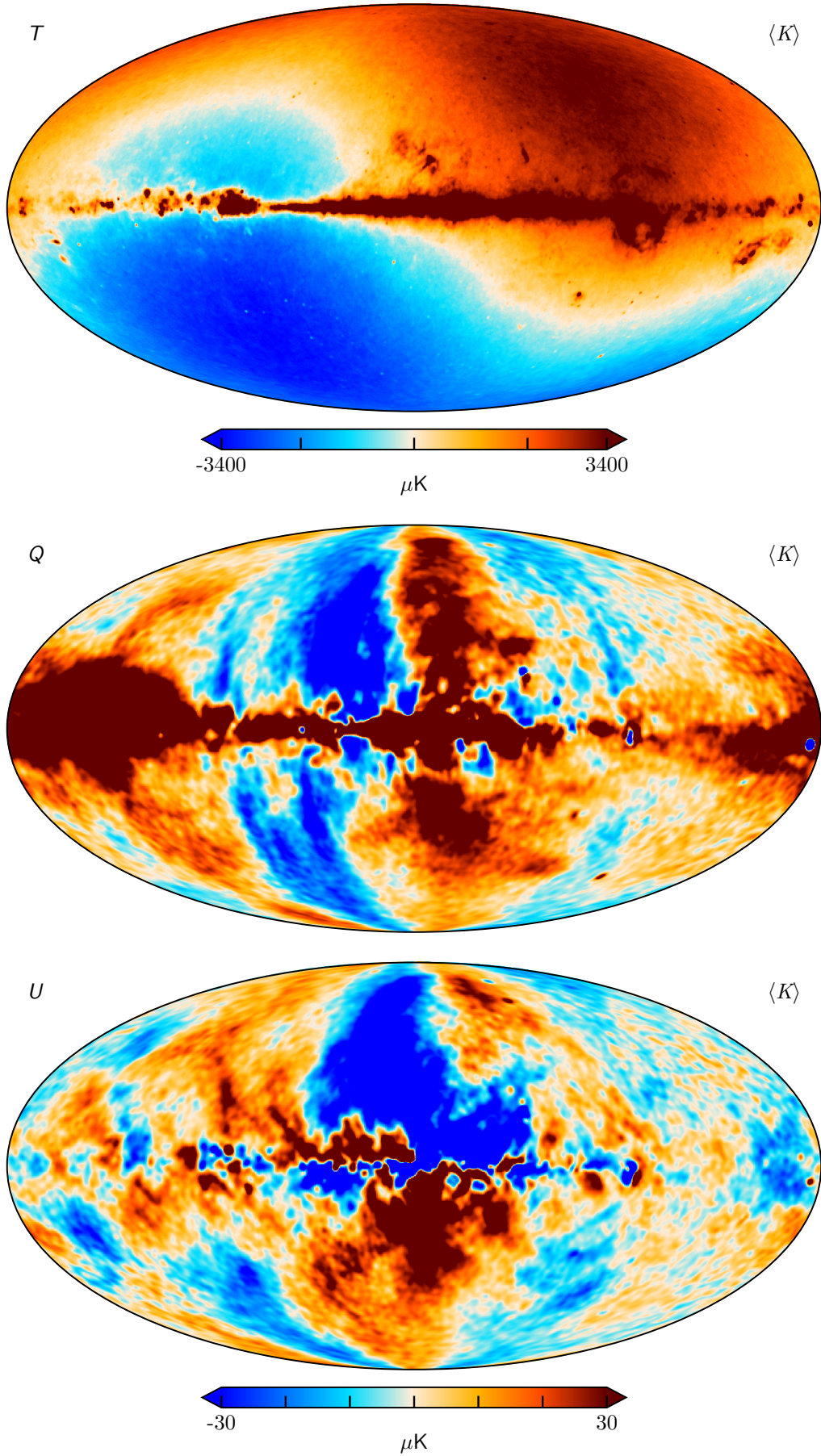
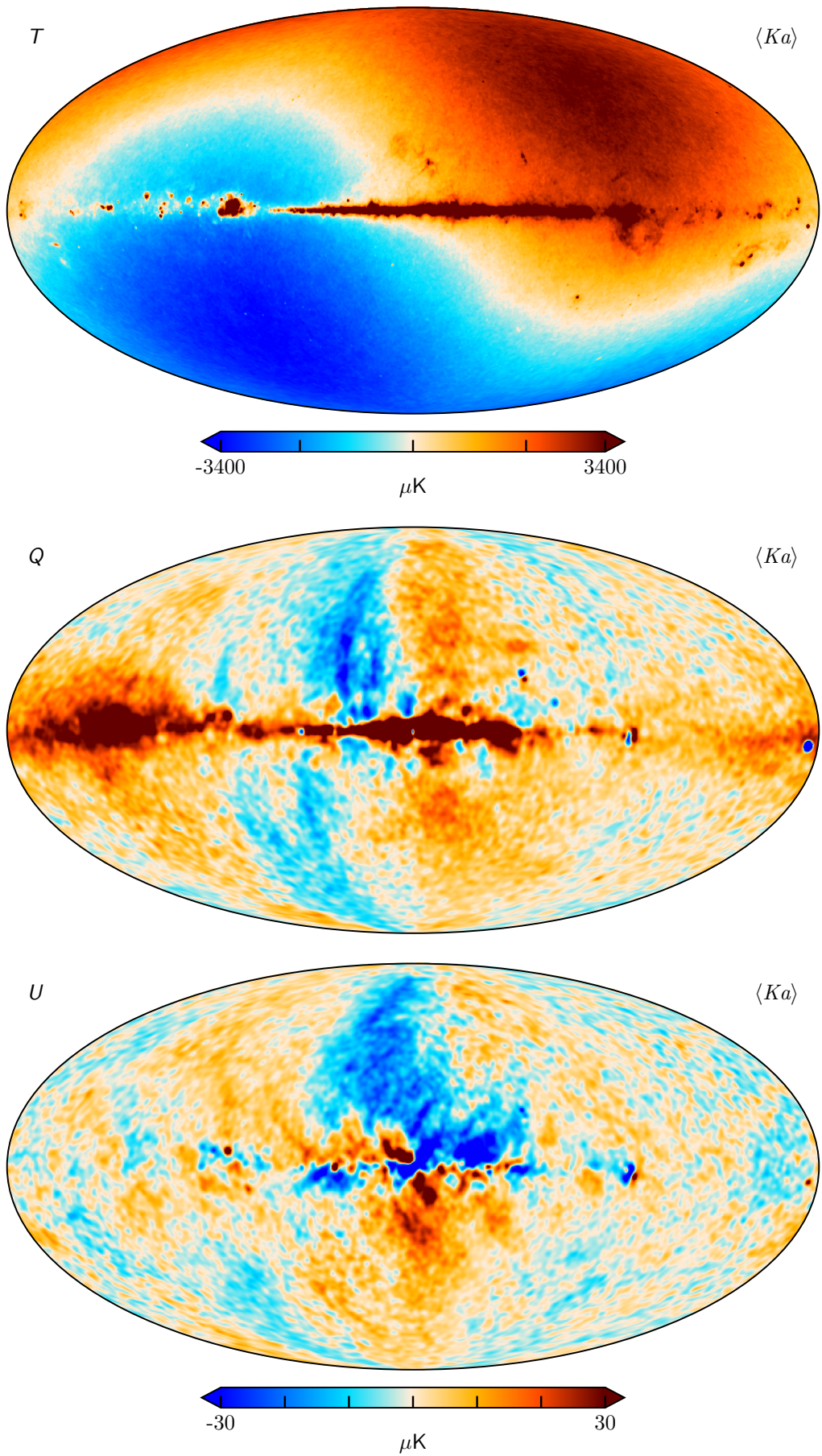
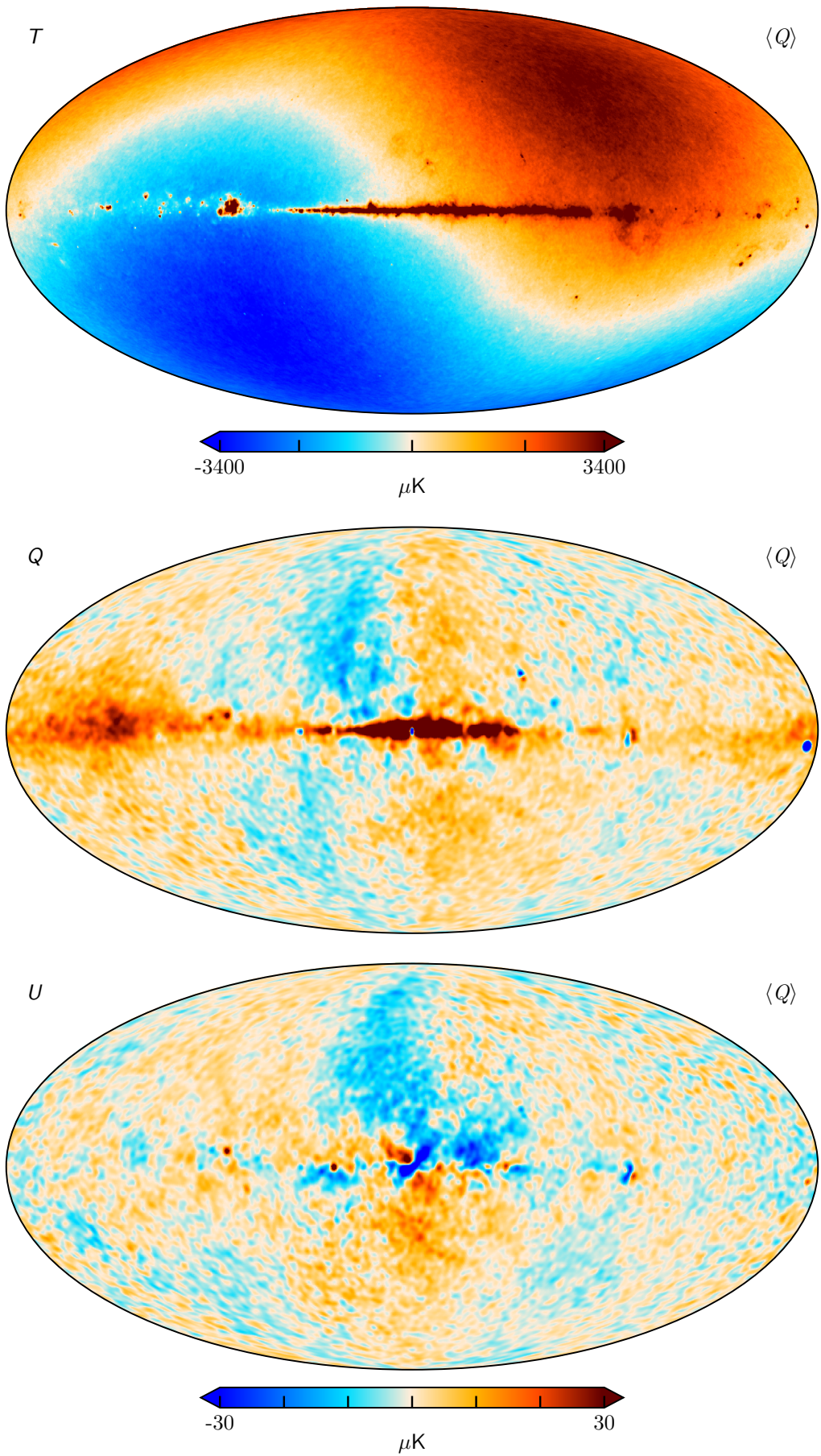
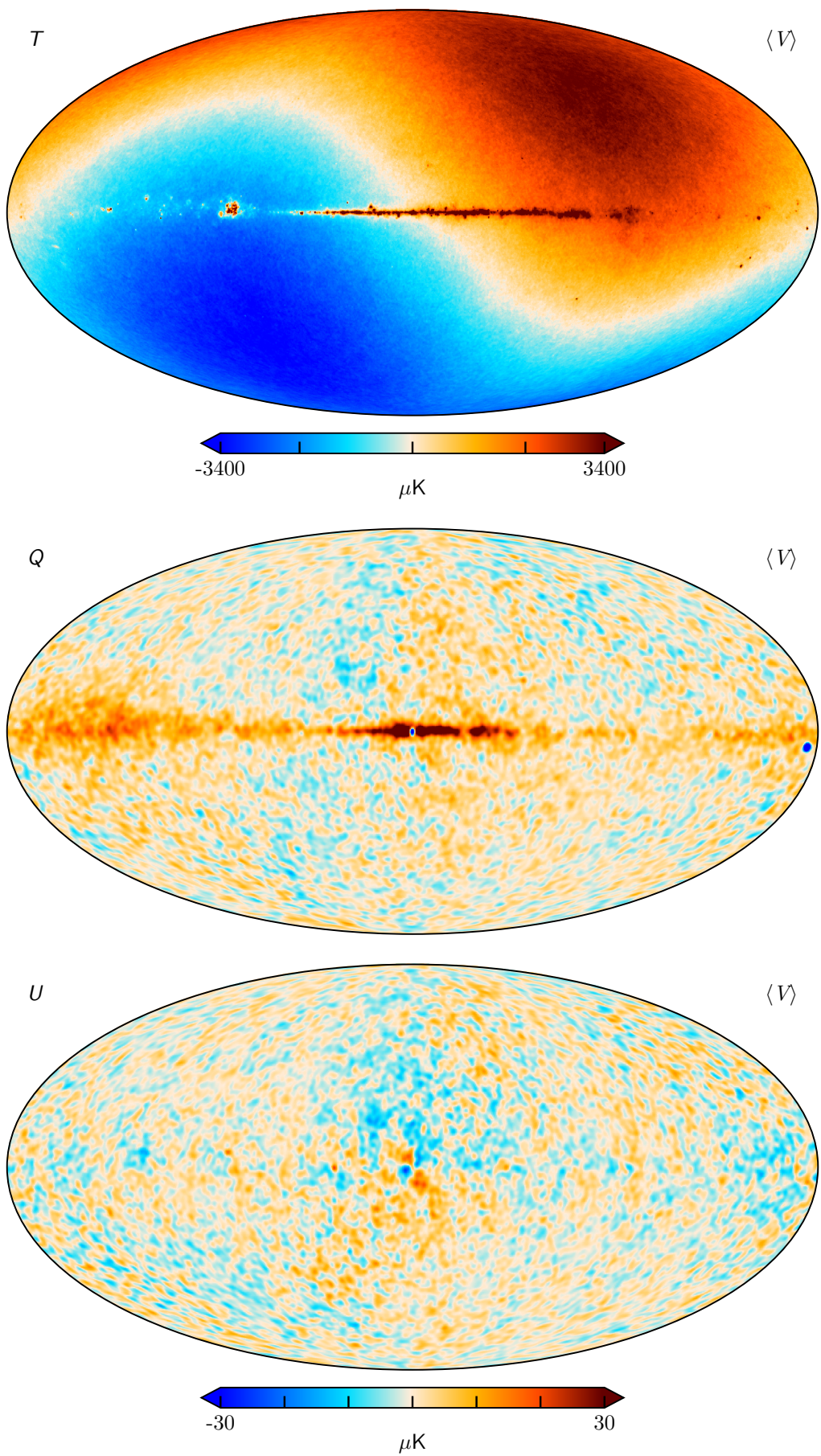
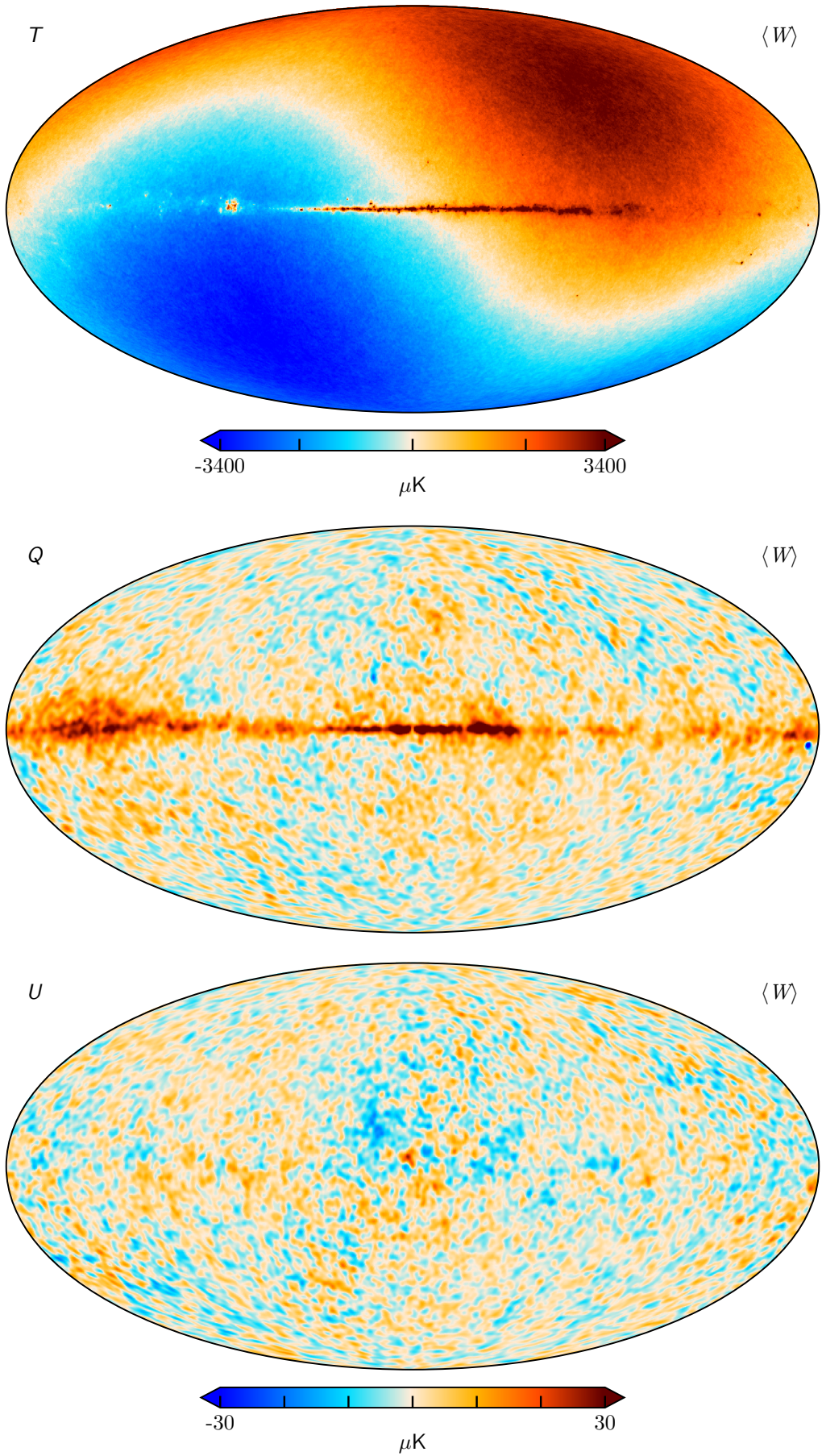


Fig. 13. Posterior mean K -band map produced with the COSMOGLOBE pipeline. Rows show Stokes T , Q , and U , respectively. The temperature map is shown at full resolution, while the polarization maps are smoothed with a 2° FWHM Gaussian beam.

**Fig. 14.** Same as Fig. 13, but for Ka -band.

**Fig. 15.** Same as Fig. 13, but for Q -band.

**Fig. 16.** Same as Fig. 13, but for V -band.

**Fig. 17.** Same as Fig. 13, but for W -band.

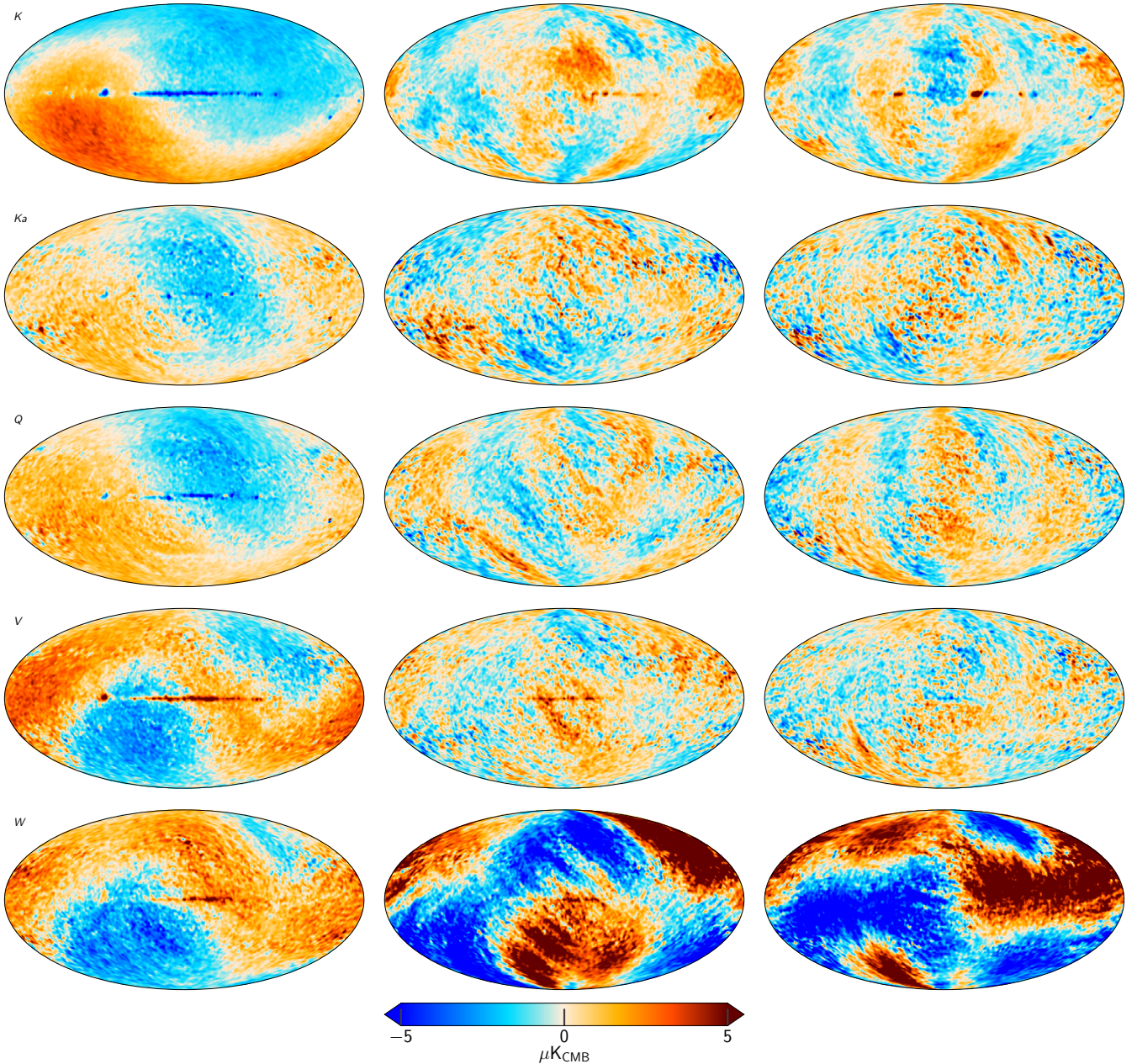


Fig. 18. Difference maps between the COSMOGLOBE and 9-year *WMAP* frequency maps. Columns show Stokes T , Q , and U parameter maps, while rows show K -, Ka -, Q -, V -, and W -band maps. The maps are all smoothed with a 2° FWHM Gaussian beam.

between the COSMOGLOBE and *WMAP* maps by eye when switching rapidly between them. However, it is important to note that the COSMOGLOBE frequency maps retain the Solar CMB dipole, following Planck Collaboration LVII (2020) and BeyondPlanck (2022), while it is removed in the *WMAP* official maps. Similarly, we see that the amplitude of the polarized maps decrease as expected from K – V -band following the expected synchrotron behavior, with a slight increase at W -band due to the contribution of thermal dust.

Next, in Fig. 18, we show corresponding difference maps between the official 9-year *WMAP* maps and the maps produced in this work. The color scale in this plot is linear and ranges over $\pm 5 \mu\text{K}$, and we see that the differences are thus quite small; typically smaller than 1 – $2 \mu\text{K}$ for most channels. The main exception to this is W -band polarization, for which the differences are generally larger than $5 \mu\text{K}$.

Going into greater detail and starting with total intensity, we see first that the K -band difference is dominated by a dipole with a $\sim 2.5 \mu\text{K}$ amplitude that is anti-aligned with the CMB Solar dipole. In addition, the Galactic plane is slightly blue. Both of these suggest that our total absolute K -band calibration is lower than the *WMAP9* value by about 0.1 %; given the major differences in methodology described in Sect. 2, the agreement is almost surprisingly good. A similar small dipole difference is also seen in Q -band.

For the remaining channels, and in particular for the V - and W -bands, the main intensity difference takes the form of a quadrupole with an amplitude of 2 – $3 \mu\text{K}$ aligned with the CMB dipole. Naively, one could suspect this to be due to different treatments of the relativistic quadrupole. However, as noted by Larson et al. (2015), the *WMAP9* maps retain the kinematic quadrupole, as does Commander3; in our framework, this sig-

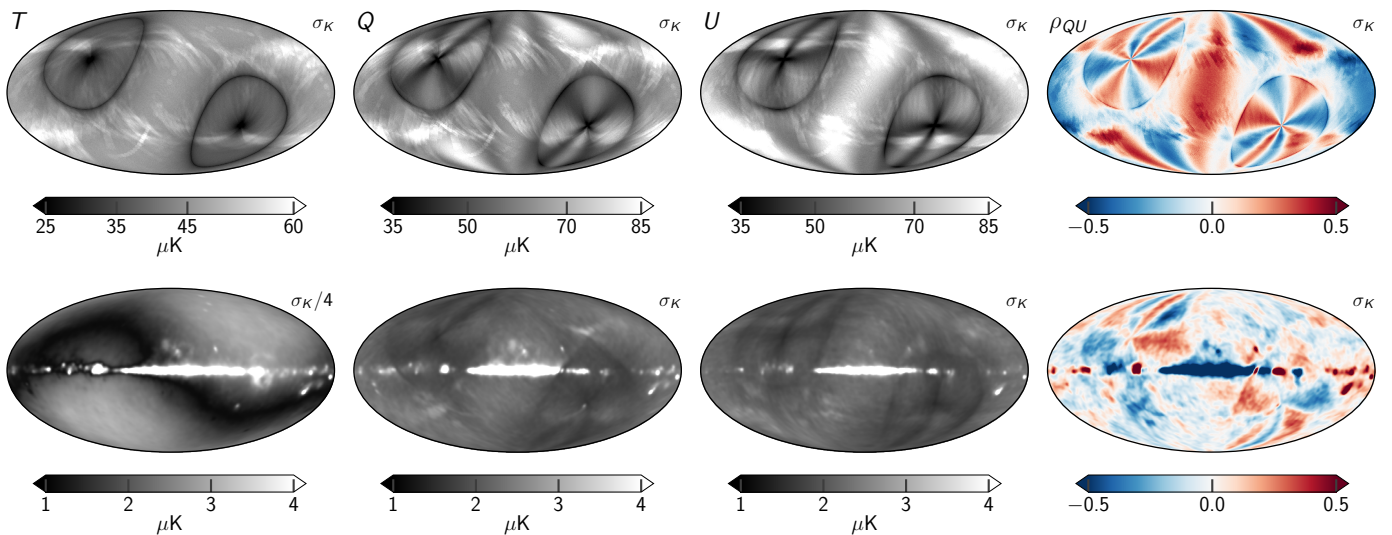


Fig. 19. Posterior variation maps for K -band. Columns show the Stokes parameters and the correlation coefficient between Q and U , while the rows show (top) the white noise rms per pixel and (bottom) the posterior standard deviation. The rms maps are unsmoothed, while the standard deviations have been smoothed to 7° .

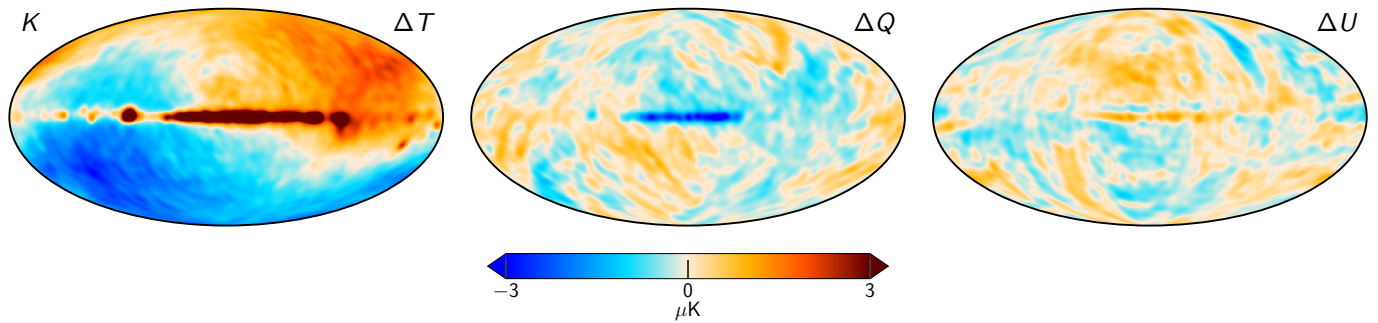


Fig. 20. Difference between two K -band Gibbs samples, smoothed to 7° .

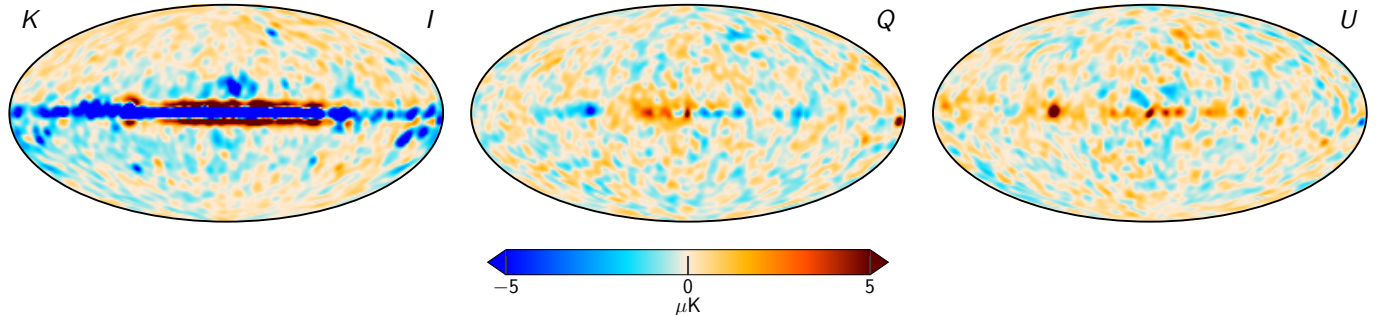


Fig. 21. TOD-level residual map for K -band, smoothed with a 5° FWHM Gaussian beam.

nal term is accounted for through the signal model defined in Eq. (10). This is notably different from the *Planck* maps, which do remove the relativistic quadrupole from the frequency maps (Planck Collaboration II 2020; Planck Collaboration III 2020). Additionally, even though the observed quadrupole has the expected shape, the frequency dependence is not consistent with the expected functional form $x \coth x$ where $x = h\nu/(2kT_{\text{CMB}})$ (Notari & Quartin 2015). For now, we speculate that these differences are rather due to second-order gain or baseline differences, possibly associated with the annual oscillatory structures seen in Fig. A.4.

In polarization, we note large scale differences in both Stokes Q and U . These differences do not match known Galactic component morphologies, but are more reminiscent of the poorly

measured transmission imbalance modes discussed by Jarosik et al. (2011), although the map-space morphologies are not identical. In general, such large mode differences are due to at least three main effects: 1) incomplete polarization angle coverage for a few large-scale modes; 2) errors in transmission imbalance coupled with the Solar dipole; and 3) interplay between the transmission imbalance, the far sidelobe, and the Solar dipole, as briefly described in Sect. 2.2. The scale of these effects is most pronounced in the W -band polarization results, where we see the largest differences between the two processing pipelines.

From these differences alone, it is not possible to determine whether the excess structures are present in the COSMOGLOBE or WMAP maps, or both. However, Appendix B provides a complete survey of the COSMOGLOBE frequency maps, and in particu-

lar Fig. B.1 compares these with the *WMAP9* maps. In this case, one clearly sees that the large-scale modes are predominantly present in the *WMAP* maps, rather than COSMOGLOBE.

Returning to the internal properties of the COSMOGLOBE posterior distribution, we show in the top panel of Fig. 19 the *K*-band white noise standard deviation per pixel in Stokes *T*, *Q* and *U*; the fourth column shows the correlation coefficient between the *Q* and *U* coefficients. The bottom panel shows the corresponding posterior standard deviation per pixel. It is important to note that the white noise is not a free parameter in the data model, and there is no white noise component in the Gibbs sampler described by Eqs. (18)–(25). That also implies that there is no marginalization over white noise in the resulting frequency map ensemble. Rather, the full marginal uncertainty per frequency map pixel must be obtained by added the two rows in Fig. 19 in quadrature. However, a vastly preferable approach to perform error propagation for higher level scientific analyses is to analyze each sample separately, taking into account only white noise for each sample, and then use the full sample ensemble as the final result. This is the only robust way of fully accounting for all correlations between the various effects.

The white noise pattern for *T* follows the usual pattern with highest sensitivity at the North and South ecliptic poles, as well as circles around the poles corresponding to times when the partner horn is observing the opposite ecliptic pole. There are also regions of higher noise level corresponding to planets crossing the ecliptic, and regions of higher emission $\approx 140^\circ$ away from the Galactic center, which correspond to the times when the partner horn lies within the processing mask.

The polarized RMS maps share all of these characteristics, but with an overall amplitude shift due to polarization measurements having half the effective number of observations per pixel. In addition, the poles have a characteristic “X”-like structure that is rotated 45° degrees between *Q* and *U*, corresponding to different polarization orientations. There are also characteristic large scale structures visible in Galactic coordinates, corresponding to polarization modes poorly constrained by the *WMAP* scan strategy.

While the maps in the top row of Fig. 19 are directly comparable to the corresponding *WMAP9* products, the posterior mean shown in the bottom row has no equivalent in the official *WMAP* release. These maps can be considered the “systematic” error contributions, as their variation depends on the sampled instrumental parameters, i.e., gain, imbalance parameters, correlated noise, and sidelobe correction. The temperature map contains a clear quadrupole signature. This is due to the variation in the absolute calibration g_0 , which changes the Solar dipole in the final map. In addition to the quadrupole, the Galactic plane also varies due to the gain solution being varied. As expected, the white noise patterns associated with the scan strategy also appear in the polarization maps, which have much lower signal-to-noise ratio than the temperature map.

Another useful quantity is the difference between two arbitrary samples, which we show in Fig. 20. In temperature, the most striking term is a dipole, corresponding to the absolute gain difference, and the Galactic plane. There are also additional weaker lines associated with the scanning strategy, correspond to different correlated noise and time variable gain realizations. In polarization, gain variations, bandpass uncertainties, and correlated noise dominate the differences between two samples, as quantified in Fig. 12. The polarization differences are aligned with *WMAP*’s scans, modulated by the polarization angle.

Finally, the quality of the model in map space can be evaluated quite well by looking at the calibrated residual map, i.e.,

mapping the time-ordered residual $\mathbf{r} \equiv (\mathbf{d} - \mathbf{n}^{\text{corr}})/\mathbf{g} - \mathbf{s}^{\text{tot}}$. We display this TOD residual for *K*-band in the bottom panel of Fig. 11 (2° FWHM) and Fig. 21 (5° FWHM). In temperature there is a large residual along the Galactic plane, which is to be expected both for both temperature and polarization, due to the complexity of the Galactic center. The temperature residual also contains a $\sim 3 \mu\text{K}$ dipole due to the prior sampling of g_0 – drawing a sample based on the sky model would track the dipole much more closely, whereas the prior sampling by definition does not use the sky model to draw g_0 . Other than the Solar dipole, Galactic plane, and point sources, both the temperature and polarization maps are visually consistent with white noise across the entire sky.

Again, we have for brevity primarily focused on *K*-band in this discussion. For completeness, however, similar plots for all DAs are shown in Appendix B. In particular, Fig. B.1 compares the COSMOGLOBE and *WMAP* DA polarization maps, Figs. B.2 and B.3 shows the white noise and posterior rms’s, Fig. B.4 shows sample differences, and Fig. B.5 shows TOD residual maps.

In Fig. 22 we compare angular power spectra computed from both COSMOGLOBE and *WMAP9* frequency maps. These spectra are derived using the NaMaster (Alonso et al. 2019)⁷ compute_full_master routine, while applying the extended *WMAP* temperature analysis mask which allows a sky fraction of 68.8 %. As the *TT* power spectrum is strongly signal-dominated for $\ell \lesssim 200$ for all DAs, it is particularly informative to consider ratios, and this is shown in the left column of Fig. 22. Here we see that the *TT* spectra derived from the two pipelines are consistent to sub-percent level at all but the very largest and smallest scales for all DAs. We speculate that the large scale differences are due to different CMB Solar dipoles – as noted above, the COSMOGLOBE maps retain the Solar CMB dipole, and an estimate of this must be subtracted before evaluating these spectra. In contrast, the *WMAP* maps have this contribution removed at the TOD level; small differences due to these different treatments are not unexpected. The small scale differences above $\ell \sim 200$ can be attributed to different data selections and low-level processing. For instance, the COSMOGLOBE maps exploit about 1 % less data than *WMAP9*; COSMOGLOBE fits one σ_0 parameter per scan, while *WMAP9* assumes it to be constant for each year; the *WMAP* gain model varies every 23 sec, while the COSMOGLOBE model assumes constant gain per scan etc.

The *EE* power spectra, displayed in the second column of Fig. 22, are mainly dominated by noise and polarized synchrotron emission. As expected, the large scale foreground-dominated multipoles decrease in amplitude according to the relative amplitude of the synchrotron spectrum. Overall, the COSMOGLOBE and *WMAP9* power spectra appear fairly consistent for the *K*–*Q* channels, while at *V*- and *W*-band there is noticeably more scatter at low multipoles in the *WMAP9* spectra than in the COSMOGLOBE spectra.

The *BB*-mode power spectra, displayed in the third column of Fig. 22, is expected to follow a similar pattern, but since foregrounds are generally reduced by a factor of ≈ 2 –4 (Bennett et al. 2013; Planck Collaboration IV 2018), this spectrum is less signal-dominated, and therefore more susceptible to instrumental systematics. For instance, the $C_{\ell=3}^{\text{BB}}$ mode has been identified as being particularly poorly constrained due to its symmetry aligning with $\gtrsim 10$ min signals in the TOD induced by the *WMAP* scan strategy (e.g., Jarosik et al. 2011). In this figure, it appears that these low- ℓ modes appear significantly better constrained in the COSMOGLOBE maps than in *WMAP9* for *V*- and

⁷ <https://github.com/LSSTDESC/NaMaster>

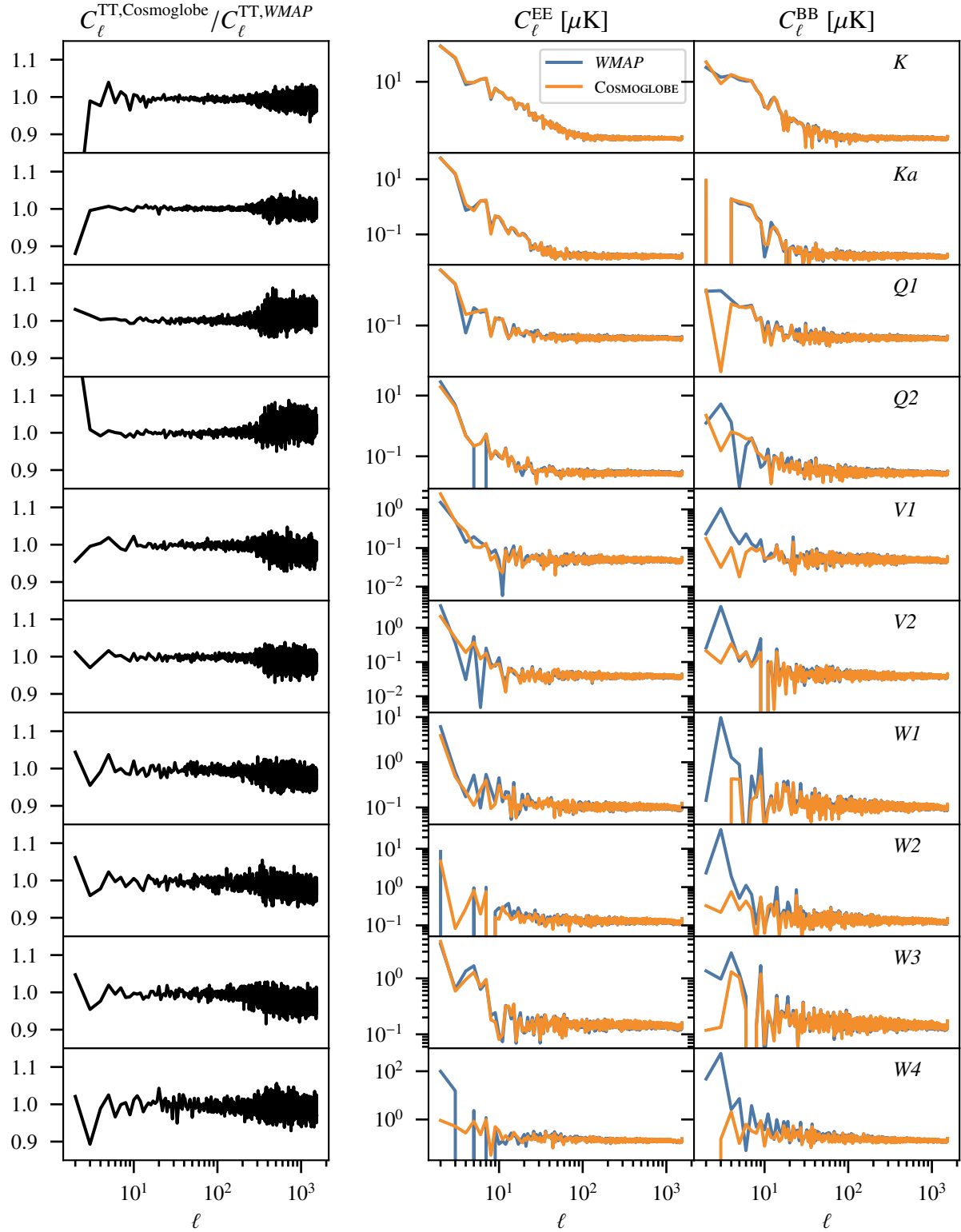


Fig. 22. Comparison of the C_ℓ^{TT} , C_ℓ^{EE} , and C_ℓ^{BB} from WMAP9 and COSMOGLOBE. Each row corresponds to a different DA, with frequency increasing from top to bottom. (left): ratio of C_ℓ^{TT} from COSMOGLOBE compared to WMAP9. (middle/right): $C_\ell^{\text{EE/BB}}$ power spectra with WMAP9 in blue and COSMOGLOBE in orange.

W-bands, and the overall large scale noise level is lower by one or two orders of magnitude.

5.2. Consistency tests through inter-channel difference maps

As described in Sect. 2.2, the Q - and V -bands each had two DAs, while the W -band had four DAs, and computing differences between the corresponding DA maps can highlight mismodeled

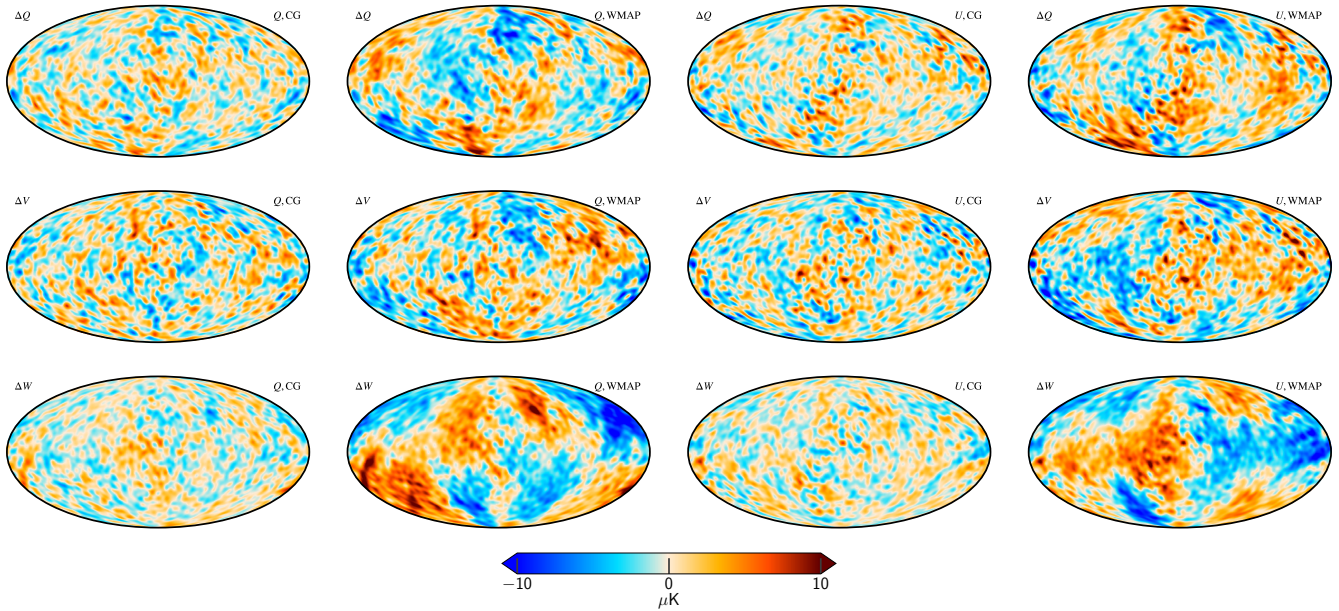


Fig. 23. Internal WMAP difference maps, smoothed by 10° . The two left columns are Stokes Q , and the two right columns are Stokes U , with the COSMOGLOBE and WMAP9 maps alternating between columns. The top to bottom rows are difference maps in increasing frequency.

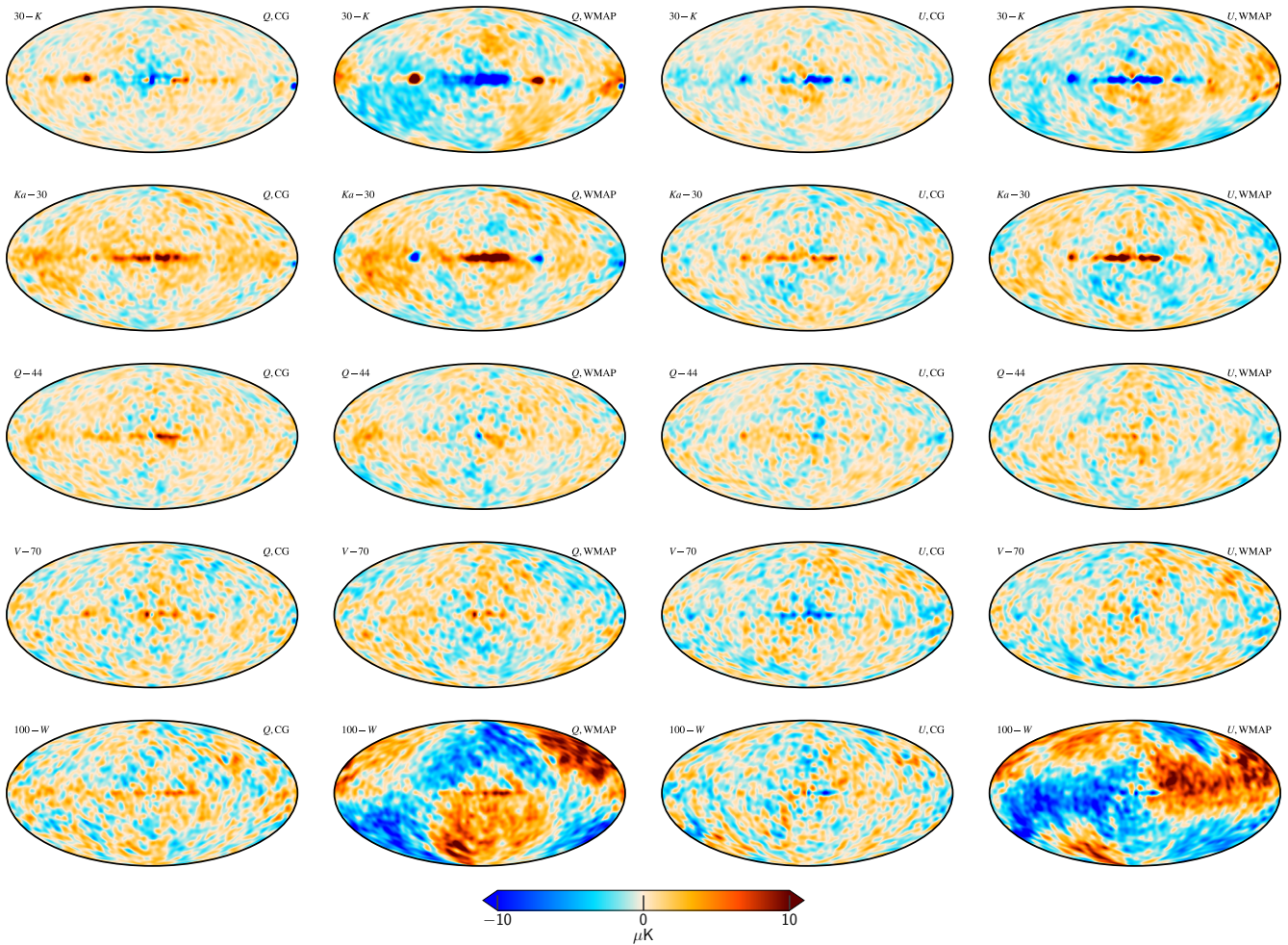


Fig. 24. Difference maps between similar WMAP and *Planck* frequency maps. The comparison plots go, by column: Stokes Q for the COSMOGLOBE-produced WMAP and *Planck* sky maps, Stokes Q for official WMAP and BEYONDPLANCK data products, Stokes U for the COSMOGLOBE sky maps, and Stokes U for the official data products. (*Top row*): WMAP LFI 30 GHz minus K -band, scaled by the synchrotron power-law. (*Top middle row*): WMAP Ka -band minus LFI 30 GHz, also scaled by the synchrotron power-law. (*Middle row*): WMAP Q -band compared to the LFI 44 GHz sky maps, scaled by the synchrotron power-law. (*Bottom middle row*): WMAP V -band minus LFI 70 GHz, with unit scalings for each band. (*Bottom row*): The *Planck* DR4 100 GHz map minus the WMAP W -band also with unit scalings for each band.

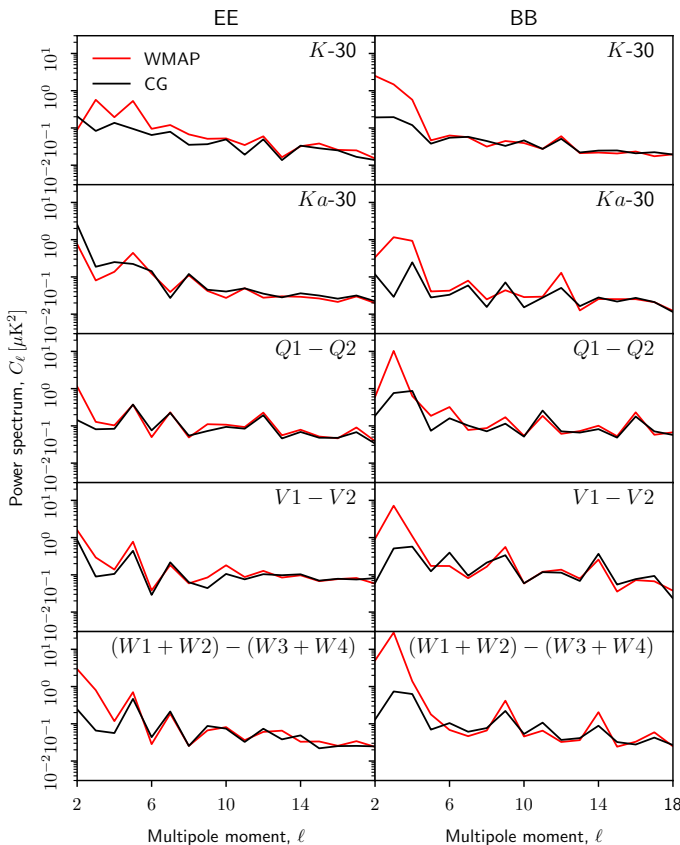


Fig. 25. Full sky half-difference spectra. The red lines are the power spectra of the *WMAP9* difference maps, while the black lines are the same for the reprocessed *COSMOGLOBE* maps.

systematics. While the *K*-band and *Ka*-band have different central frequencies, they are close enough that we can compare them by scaling *K*-band assuming a polarized synchrotron power law SED of $\beta_s = -3.1$. Similarly, internal differences between scaled *K*, *Ka*, and LFI 30 GHz maps provide an important null-test. In particular the *K*-30 difference has received significant attention ever since the *Planck* 2015 data release (Planck Collaboration I 2016), showing clear signatures of instrumental systematics. These were gradually reduced through improved *Planck* processing in the *Planck* 2018 (Planck Collaboration II 2020), PR4 (Planck Collaboration LVII 2020), and BEYONDPLANCK (Beyond-Planck 2022) data releases. Still, even after all these developments, large-scale residuals remained that was difficult to resolve through further LFI improvements (Gjerløw et al. 2022). In this section, we revisit this question for the *COSMOGLOBE* products.

We start however by inspecting internal *WMAP* half-difference maps of the form $(Q1 - Q2)/2$ etc. These are plotted in Fig. 23. Here we see that the *Q*-band and *V*-band half-difference maps from *COSMOGLOBE* have virtually no trace of poorly measured modes, and the differences appear to be well-traced by the rms maps. In contrast, the *WMAP* half-difference maps show clear evidence of large-scale residuals. The largest visual improvement is in the *W*-band, where the *COSMOGLOBE* case is almost entirely consistent with instrumental noise, as opposed to the *WMAP9* difference that is dominated by large-scale residuals.

Next, Fig. 24 shows comparisons between the *WMAP* *K*- and *Ka*-bands and the LFI 30 GHz channel, between the *WMAP* *Q*-band and LFI 44 GHz, and finally between *WMAP* *V*-band and LFI 70 GHz. When comparing *WMAP9* maps with *Planck* LFI,

Table 5. Transmission imbalance template amplitudes for each *WMAP* radiometer as estimated by fitting the official templates to low-resolution difference maps between *COSMOGLOBE* and *WMAP*. The templates are provided in mK, and the template amplitudes are therefore dimensionless. The fourth column lists the relative decrease in standard deviation, $\sqrt{\sigma_{\text{raw}}^2 - \sigma_{\text{corr}}^2}/\sigma_{\text{raw}}$, after subtracting the best-fit templates in percent.

DA	a_1	a_2	$\Delta\sigma[\%]$
K1	-27.5	-50.6	30
Ka1	-1.4	-1.9	25
Q1	-30.0	-71.6	11
Q2	-7.1	-1.5	20
V1	-32.8	-53.4	6
V2	8.8	-4.1	16
W1	-2.8	4.6	8
W2	-6.9	-3.5	11
W3	29.1	53.4	12
W4	15.5	-6.8	52

we use BEYONDPLANCK products, which represent the cleanest version of *Planck* LFI published to date. For the *COSMOGLOBE* map comparison, both *WMAP* and *Planck* maps were produced by this joint analysis. Additionally, we compare the mean *W*-band maps with the *PlanckHFI* DR4 100 GHz channel. It is worth noting that this 100 GHz map has had no input from Commander3 so this difference map is an independent comparison between two datasets and processing methods.

Starting with the *COSMOGLOBE* maps, we see in the first and third columns of Fig. 24 that the magnitude of the differences are small in both Stokes *Q* and *U*. Overall, across all five frequency map comparisons we see small levels of variation, with structure contained to the Galactic plane. Notably, however, there is a larger sky signal within the *Ka* – 30 Stokes *Q* comparison. This large-scale difference also exists in the *Q* – 44 Stokes *Q*, but it did not appear in the internal *Q* half-difference map.

Columns two and four of Fig. 24 show corresponding differences between the official *WMAP9* and BEYONDPLANCK LFI frequency maps. Similar to the *COSMOGLOBE* sky map comparisons, we see differences in the Galactic center, and to a lesser degree along the Galactic plane due to the slight differences in the frequency coverage. When comparing the official *WMAP* maps, particularly for *K*-band, we see structures sweeping across large angular scales across the sky, likely due to the poorly measured modes in *K*-band.

Of particular note is the 100 – *W* difference map. The *COSMOGLOBE* difference maps here have a similar level of white noise and Galactic contamination as the *V* – 70 maps, whereas the *WMAP9* differences are driven by obvious transmission imbalance modes, each with an opposite sign and magnitude. The difference between 100 GHz and *W* demonstrates that the good agreement between the *WMAP* and *Planck* LFI is not simply due to fitting low-level parameters in a joint analysis framework – by obtaining *W*-band maps that are consistent with an independent 100 GHz polarization map, we have shown that the *WMAP* is not simply the result of adding more free parameters to the fit, but a genuine improvement in data processing.

Finally, as noted by Jarosik et al. (2011) the low- ℓ *W*-band polarization data were excluded entirely from the cosmological analysis due to excess variance in the $\ell \leq 7$ multipoles. To test the *COSMOGLOBE* maps’ performance at these scales, we take the power spectrum of the full-sky difference maps using the standard *anafast* routine in Fig. 25. With very few exceptions, the

WMAP9 power spectra have much more power at $\ell \leq 7$ than the COSMOGLOBE maps in both the E -modes and B -modes. Of particular note is the $\ell = 3$ B -mode, which has consistently been identified as poorly measured in the WMAP scan strategy, and has been reduced in every difference spectrum. Based on these power spectra alone, there does not appear to be a strong justification for exclude the reprocessed W -band polarization data in future cosmological analyses.

Based on these calculations, we conclude that the modes that are nearly degenerate by the WMAP scanning strategy, and have represented a major challenge for the official WMAP processing for more than a decade, appear to have been properly regularized by the global COSMOGLOBE processing. The frequency maps do not show any evidence of either poorly constrained transmission imbalance modes or other large-scale artefacts, and they are more self-consistent than the WMAP9 frequency maps.

5.3. Efficiency of template-based transmission imbalance uncertainty propagation

Before concluding this section, we revisit the issue of transmission imbalance error propagation in the official WMAP approach. As discussed by [Jarosik et al. \(2007\)](#), and seen in Fig. 7 in this paper, x_{im} is associated with significant measurement uncertainties, and these uncertainties translate directly into correlated large-scale polarization residuals. To account for these uncertainties, the WMAP pipeline produced a spatial templates by calculating a frequency map for which both x_{im} values were increased by 10 % from their nominal values in a given DA, and subtracting this from the baseline map. A second template was generated by increasing one value by 10 % and decreasing the other by 10 %. The modes corresponding to the resulting spatial templates were then accordingly downweighted through the low-resolution noise covariance matrix using the Woodbury formula.

This approach is effectively equivalent to assuming that the major impact of transmission imbalance may be described in terms of a bi-linear vector space, and that this vector space is statistically independent from other errors contributions, such as the correlated noise and gain. This is obviously an approximation, and given the new maps presented in this paper it is possible to derive at least a rough estimate of how well this approximation works.

Specifically, considering the large improvement in half-difference maps seen in Fig. 23, and the morphology of the full frequency difference maps seen in Fig. B.1, it for the purposes of this section reasonable to assume that most of the large-scale polarization differences in Fig. 18 are due to WMAP9 rather than COSMOGLOBE. We therefore fit the pair of WMAP transmission imbalance templates for each DA to the difference map between WMAP9 and COSMOGLOBE, and we subtract this from the difference map. The best-fit template amplitudes are listed in the second and third column of Table 5 for each DA. In this table, we see that the coefficients within each DA tend to be quite similar, both in magnitude and sign. This is due to the fact that the two individual templates also tend to be highly correlated in terms of spatial structure but with opposite sign. As such, there are strong degeneracies between the two resulting coefficients, and only the sum over both templates carries physical meaning.

Figure 5 summarizes the results from these calculations in map domain. Each row correspond to one DA, while the left and right half-sections of the figure correspond to Stokes Q and U , respectively. (One common parameter is fitted per template for both Stokes parameters, but they are for convenience visualized

separately.) Within each section, the left column shows the raw difference, the middle column shows the sum of the best-fit templates, and the right column shows the residual obtained after subtracting the best-fit templates from the raw difference.

Comparing the left and middle columns in each section, we see that – at least at a visual level – the WMAP templates do indeed trace the residuals to a high degree for many channels, e.g., K , $Q1$, $V2$ etc. For some channels, such as $Ka1$ and $Q2$, the agreement is less convincing. However, as seen in the right-most column, even for the well-fitting channels the templates are unable to explain all of the difference.

To roughly estimate how much of the full difference may be described by the WMAP templates, we compute the relative decrease in standard deviation between the full difference map (left columns) and the template-corrected map (right columns) of the form $\sqrt{\sigma_{\text{raw}}^2 - \sigma_{\text{corr}}^2}/\sigma_{\text{raw}}$; in the case that the template correction happened to account for the full difference, this quantity would be unity, while in the case in which it did not account for anything, it would be 0.

The results from this calculation are summarized in the fourth column in Table 5. Here we see that the two linear templates are able to account for between 6 and 52 % of the full large-scale difference between COSMOGLOBE and WMAP; the remaining power must either be due to implicit but unmodelled nonlinear couplings between x_{im} and other parameters (such as the gain) in the WMAP pipeline that are accounted for through the Markov chain sampling in COSMOGLOBE; other large-scale systematic effects in WMAP that are unrelated to transmission imbalance; or not-yet-identified systematic uncertainties in COSMOGLOBE. Overall, it seems likely that the template-based correction of the low-resolution covariance matrices used in the cosmological WMAP likelihood does not provide a complete description of the full large-scale uncertainties. This could potentially be relevant for the differing estimates of the optical depth of reionization between WMAP9 ([Hinshaw et al. 2013](#)) and *Planck* ([Planck Collaboration V 2020](#)), and resolving this point is clearly a high-priority target for a future second COSMOGLOBE data release.

6. Preliminary astrophysical results

The main scientific goal of the current paper is to derive and publish new low-systematic state-of-the-art WMAP frequency sky maps through end-to-end Bayesian analysis. Ideally, these maps should be accompanied with a fully converged posterior distribution that allows derivation of all relevant scientific applications, including low- ℓ polarization. However, as discussed in Sect. 3.3, producing a sufficient number of samples for estimating the optical depth of reionization will require about nine months of continuous runtime. At the same time, any scientific applications that do not require such a large number of samples will benefit greatly already from the currently available data.

In this section, we present a number of typical applications for which this is the case. In particular, in Sect. 6.1 we present Galactic foreground maps derived in the current analysis, and in Sect. 6.2 we present WMAP+LFI CMB results, including an updated dipole estimate, a temperature power spectrum, and a reassessment of various low- ℓ anomalies. In Sect. 6.3 we quantify the goodness-of-fit of the current COSMOGLOBE sky model in terms of frequency residual maps and χ^2 statistics, before concluding with a comparison of the relative signal-to-noise ratio of WMAP and LFI to each physical component in Sect. 6.4.



Fig. 26. Efficiency assessment of the *WMAP* approach for transmission imbalance error propagation. The left and right sections of the figure correspond to Stokes Q and U parameters, respectively, while rows show different DAs. Within each section, the left panel shows the raw difference between the *WMAP9* and COSMOGLOBE DA maps, while the middle panel shows the best-fit *WMAP* transmission imbalance template combination; the right panel shows the difference between the two. Only one template amplitude is fit for both Q and U .

6.1. Galactic foregrounds

As described in Sect. 2.4, and defined by Eqs. (10)–(15), the Galactic sky model we adopt in this analysis is very similar to that of BeyondPlanck (2022). Explicitly, it includes synchrotron, free-free, AME, and thermal dust emission in intensity, and synchrotron and thermal dust emission in polarization, and we fit the individual amplitude of each component per pixel. However, there are two notable changes. First, we adopt an exponential SED model for AME rather than an SpDust-based SED, and this is motivated by the observation that the SpDust models appears to underestimate the AME amplitude at frequencies be-

tween 40 and 60 GHz. Second, as discussed in Sect. 2.5, we impose stronger (data-informed) priors on the SED parameters. The motivation for this is to reduce degeneracies between the foreground model and overall gains, which otherwise can lead to very long Markov chain correlation lengths. In the future, these priors should be removed after adding additional data that breaks these degeneracies directly, in particular from *Planck* HFI, QUIJOTE, and C-BASS. As shown in Sect. 6.3, no significant foreground correlated artefacts arise from these priors (as would be the case if the priors were poorly chosen), and so these priors have a small impact on the *WMAP* frequency maps themselves, which are the main scientific targets in this paper. On the other

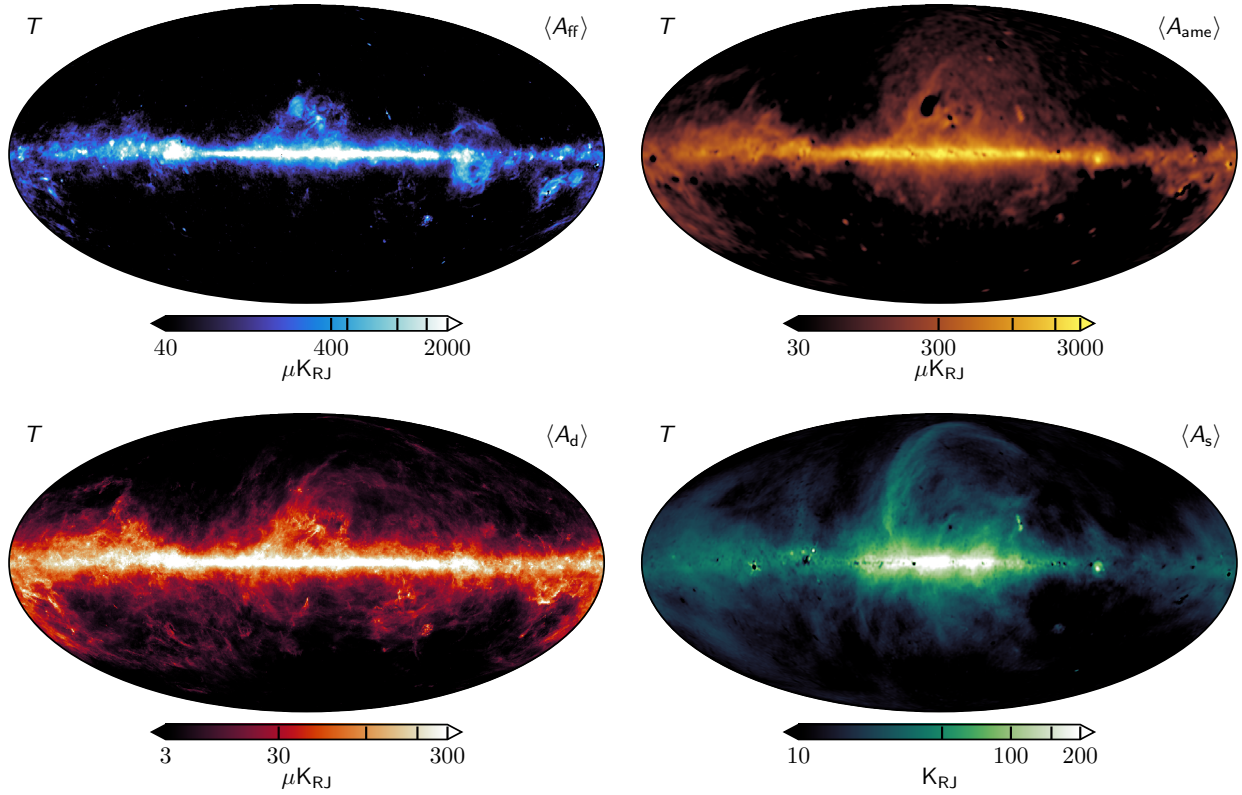


Fig. 27. Foreground intensity maps, evaluated at their respective reference frequencies. (Top left:) Free-free emission at 40 GHz. (Top right:) Anomalous microwave emission evaluated at 22 GHz. (Bottom left:) Thermal dust emission at 70 GHz. (Bottom right:) Synchrotron emission evaluated at 408 MHz.

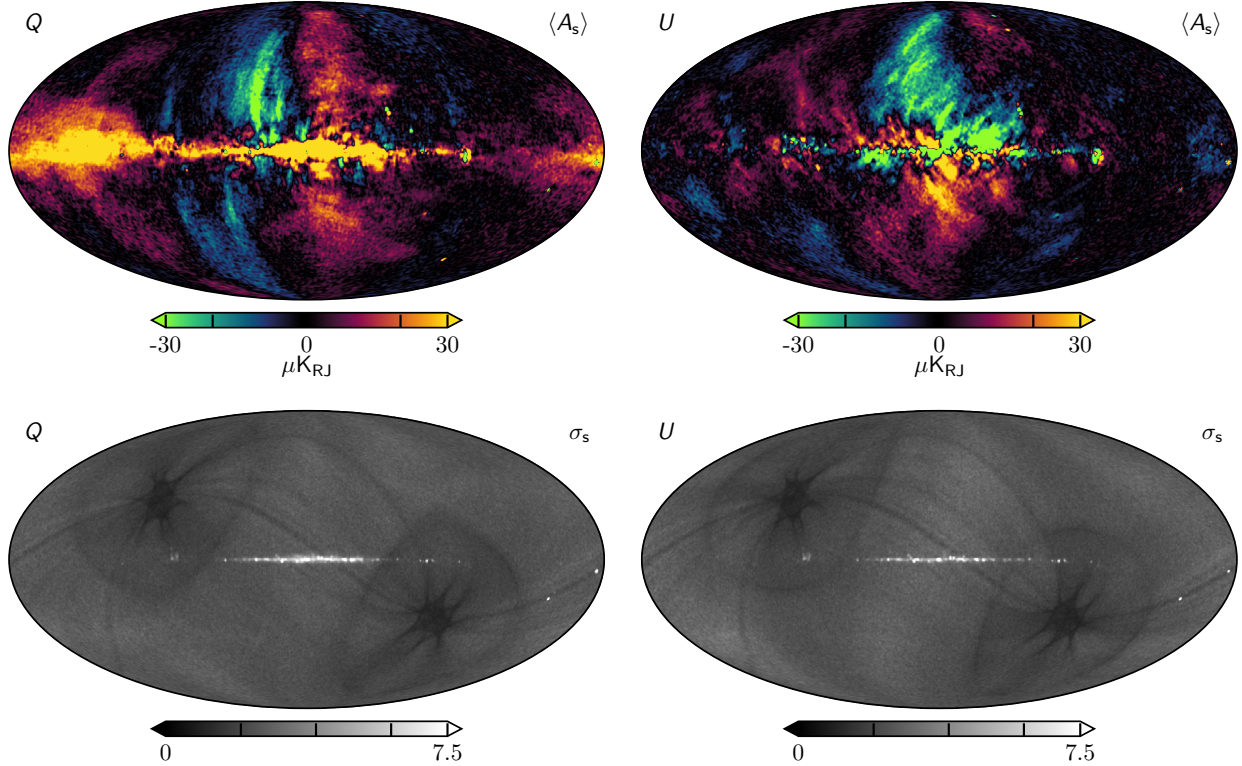


Fig. 28. Polarized synchrotron maps and their standard deviations evaluated at 30 GHz.

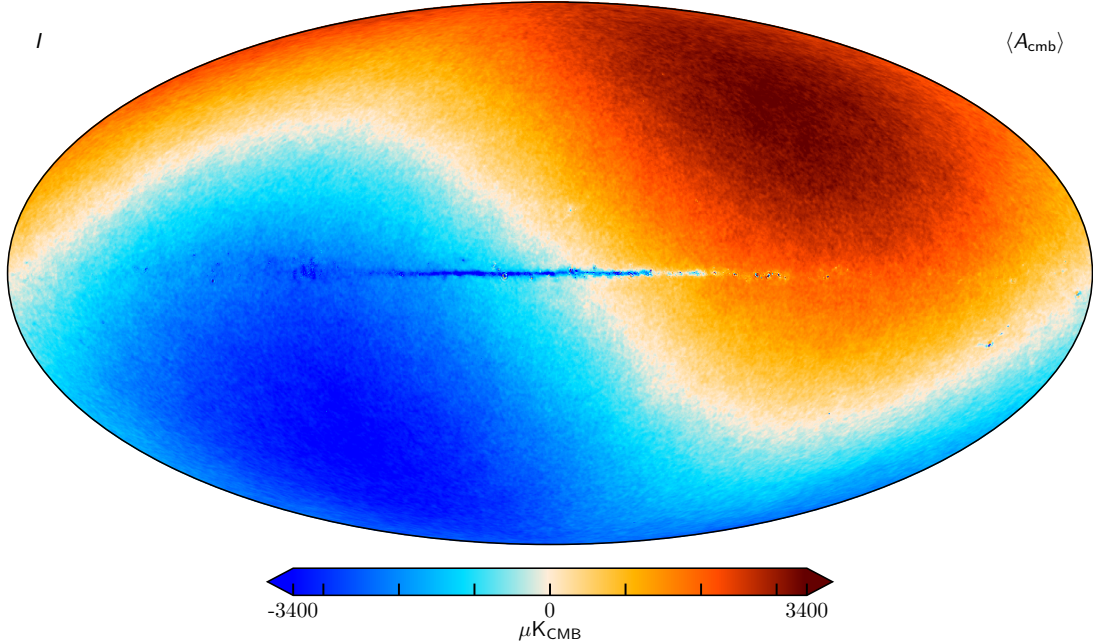


Fig. 29. Posterior mean CMB COSMOGLOBE temperature map, smoothed to an angular resolution of 14' FWHM.

Table 6. Comparison of Solar dipole measurements from *COBE*, *WMAP*, and *Planck*.

EXPERIMENT	AMPLITUDE [μK_{CMB}]	GALACTIC COORDINATES		REFERENCE
		<i>l</i> [deg]	<i>b</i> [deg]	
<i>COBE</i> ^{a,b}	3358 ± 23	264.31 ± 0.16	48.05 ± 0.09	Lineweaver et al. (1996)
<i>WMAP</i> ^c	3355 ± 8	263.99 ± 0.14	48.26 ± 0.03	Hinshaw et al. (2009)
LFI 2015 ^b	3365.5 ± 3.0	264.01 ± 0.05	48.26 ± 0.02	Planck Collaboration II (2016)
HFI 2015 ^d	3364.29 ± 1.1	263.914 ± 0.013	48.265 ± 0.002	Planck Collaboration VIII (2016)
LFI 2018 ^b	3364.4 ± 3.1	263.998 ± 0.051	48.265 ± 0.015	Planck Collaboration II (2020)
HFI 2018 ^d	3362.08 ± 0.99	264.021 ± 0.011	48.253 ± 0.005	Planck Collaboration III (2020)
Bware	3361.90 ± 0.40	263.959 ± 0.019	48.260 ± 0.008	Delouis et al. (2021)
<i>Planck</i> PR4 ^{a,c}	3366.6 ± 2.6	263.986 ± 0.035	48.247 ± 0.023	Planck Collaboration Int. LVII (2020)
BEYONDPLANCK ^e	3362.7 ± 1.4	264.11 ± 0.07	48.279 ± 0.026	Colombo et al. (2022)
COSMOGLOBE ^e	3366.2 ± 1.4	264.08 ± 0.07	48.273 ± 0.024	This work

^a Statistical and systematic uncertainty estimates are added in quadrature.

^b Computed with a naive dipole estimator that does not account for higher-order CMB fluctuations.

^c Computed with a Wiener-filter estimator that estimates, and marginalizes over, higher-order CMB fluctuations jointly with the dipole.

^d Higher-order fluctuations as estimated by subtracting a dipole-adjusted CMB-fluctuation map from frequency maps prior to dipole evaluation.

^e Estimated with a sky fraction of 68 %. Error bars include only statistical uncertainties, as defined by the global COSMOGLOBE posterior framework, and they thus account for instrumental noise, gain fluctuations, parametric foreground variations etc.

hand, this does imply that the SED parameters that are sampled as part of the Gibbs chain are non-informative. Rather, spectral parameters must be estimated through external analyses from the frequency maps, and this is for instance done for polarized synchrotron emission in a companion paper by ?.

In this section, we therefore focus only on the foreground amplitude parameters. Specifically, Fig. 27 shows posterior mean intensity maps for all four components, while Fig. 28 shows the posterior mean and standard deviation for the polarized synchrotron component. Difference maps with respect to BEYONDPLANCK (Andersen et al. 2022; Svalheim et al. 2022b) are shown in Figs. ??.

Starting with the free-free intensity component shown in the top left panel of Fig. 27, we observe good agreement with previous full sky component separation studies (Planck Collaboration X 2016; Andersen et al. 2022). We note that compared to the Planck Collaboration X (2016) analysis, there is less diffuse structure in the free-free component, which is driven by the imposition of a prior at high Galactic latitudes (Andersen et al. 2022). However, in high emission regions, such as the Galactic plane and the Gum Nebula, we see strong agreement.

For the AME, shown in the top right panel, we see a slightly differing morphology compared to both Planck Collaboration X (2016) and Andersen et al. (2022). The most notable difference is the lack of extended diffuse structure in this work, with a

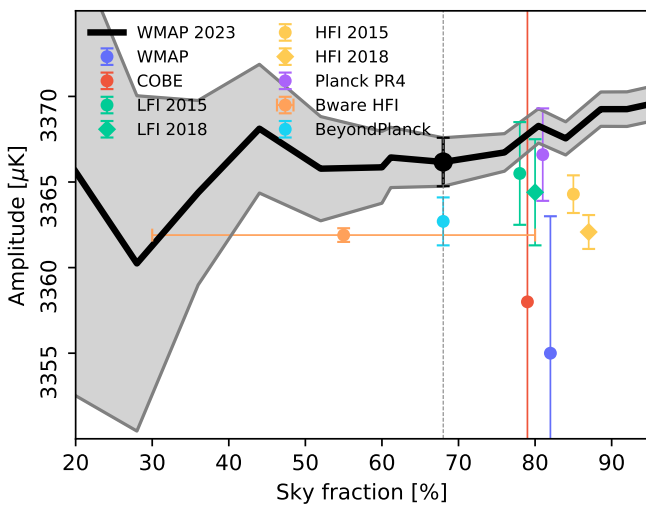


Fig. 30. CMB dipole amplitude as a function of sky fraction. The gray band indicates the 68 % posterior confidence region.

marginal shift in the overall direction of the component’s dipole. These differences are due to the different SED model, as well as the degeneracy between the K -band gain and the AME dipole, as described at length in Sect. 7.3. Both this analysis and Andersen et al. (2022) differ from the Planck Collaboration X (2016) AME solution by showing less extended diffuse structure, and most visibly notable is the ρ -Ophiuchi complex, which appears as a hole in the AME component in this work. For further details regarding the AME SED, we refer the interested reader to Watts et al. (2023).

Next, regarding synchrotron emission in total intensity, the reprocessed fullsky Haslam map (Remazeilles et al. 2015) at 408 MHz is used as an anchor for the full sky synchrotron emission in both *Planck* 2015, BEYONDPLANCK, and COSMOGLOBE. As such, the estimate shown in the bottom right panel of Fig. 27 shares very similar morphology to both these previous analyses, although there are some slight deviations around point sources. Similar observations apply to the thermal dust model, which is strongly dominated by the *Planck* 857 GHz, which is common to all these mentioned analyses.

Finally, for the polarized synchrotron amplitude, shown in Fig. 28, we also find good agreement with previous BEYONDPLANCK results (Svalheim et al. 2022b). However, the morphology of the standard deviation map shows a stronger imprint of the *WMAP* scanning strategy than in BEYONDPLANCK, and this is because the K -band data were omitted from that analysis. In this updated work, the two experiments have more comparable signal-to-noise ratios to polarized synchrotron emission, and which experiment is stronger depends now on position on the sky. As a result of finally combining all *WMAP* and LFI data, this updated map represents the most sensitive full-sky polarized synchrotron map published to date.

6.2. CMB results

Cosmological parameter estimation is left for future work, in large part because the two chains of length 250 are too short to reliably estimate cosmological parameters in this framework. For comparison, Paradiso et al. (2022) demonstrated that at least 4000 Gibbs samples were required before the reionization optical depth τ value had converged. Similarly, for BEYONDPLANCK

in the temperature case, the Gelman-Rubin statistic is just above $R = 1.01$ for $\ell \lesssim 600$ then continues to increase, indicating marginally acceptable convergence across all multipoles. Therefore, the results for the CMB presented here serve mainly as consistency checks. Given these caveats, we present preliminary CMB analysis in Sects. 6.2.1–6.2.2.

6.2.1. Solar dipole

As argued by Thommesen et al. (2020), estimating the Solar dipole is one of the more difficult parameters to accurately constrain. This is in part due to the effect of mode-coupling when masking the Galactic plane, but also due to the Solar dipole in the calibration step. In essence, the Solar dipole’s amplitude couples strongly to the calibration parameters. Misestimation of the calibration can propagate to an incorrect CMB dipole, and vice-versa.

The results of our Solar dipole estimate are displayed in Table 6 and Fig. 30. We find that the dipole direction is consistent with Colombo et al. (2022)’s result, but is $11\,\mu\text{K}$ higher than the result from Hinshaw et al. (2009). Assuming a $3400\,\mu\text{K}$ Solar dipole amplitude, an absolute calibration error of 0.3 % is sufficient to induce an $11\,\mu\text{K}$ error. In fact, the 0.2 % absolute calibration error reported by Bennett et al. (2013) can induce a $6.7\,\mu\text{K}$ Solar dipole amplitude error, dominating the error budget for the final reported Solar dipole.

It is also noteworthy that the BEYONDPLANCK Solar dipole differs from the COSMOGLOBE Solar dipole with a higher significance even than the *WMAP*9 result, despite using a nearly identical framework and almost identical datasets. First, we note that the *Planck* PR4 analysis (Planck Collaboration LVII 2020) showed a similarly apparently paradoxical discrepancy. On its face, the LFI 2018 and HFI 2018 Solar dipole values would average according to their uncertainties to $\sim 3362.3\,\mu\text{K}$. In this analysis, Planck Collaboration LVII (2020) identify relative calibration uncertainty between 100 and 143 GHz as the dominant source of uncertainty.

In the COSMOGLOBE analysis, we find that K -band has the highest signal-to-noise among all low frequency components, while being absolutely calibrated using a prior distribution. Therefore, it is likely that the chosen prior mean directly impacts the final Solar dipole amplitude, as it sets the amplitude of all low frequency components.

6.2.2. Angular temperature power spectrum

Figure 32 shows the angular temperature power spectrum derived from the CMB samples from the main Gibbs chain, obtained using a Blackwell-Rao estimator (Chu et al. 2005; Colombo et al. 2022). We compare with the official *WMAP* (Hinshaw et al. 2013) and *Planck* (Planck Collaboration V 2020) power spectra, as well as the BEYONDPLANCK (Colombo et al. 2022) spectrum. For reference, the best-fit *Planck* 2018 Λ CDM spectrum is plotted along side them. The middle panel shows the deviation from the *Planck* Λ CDM solution, in units of σ_ℓ from each individual pipeline, while the bottom panel shows the fractional difference with respect to the *Planck* Λ CDM spectrum.

The spectrum has been computed following the same Gaussianized Blackwell-Rao (GBR) (Rudjord et al. 2009) analysis described by (Colombo et al. 2022). We performed a CMB temperature resampling by imposing a prior on the spatial correlations of the CMB, and masking the Galactic plane with the BE-

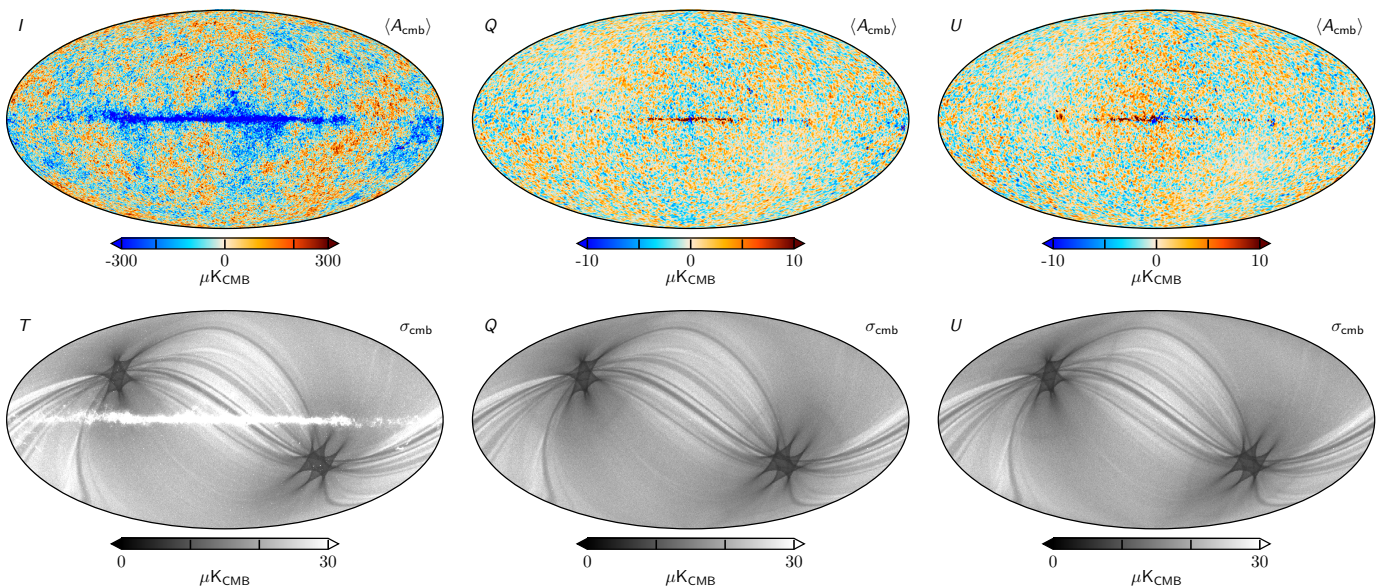


Fig. 31. Posterior mean CMB Cosmoglobe maps and their standard deviation.

YONDPLANCK temperature mask. The GBR estimator is computed using 500 CMB samples.

At $\ell \lesssim 500$, each of these datasets are signal-dominated, and each of the spectra agree at nearly every multipole. Notable exceptions include specifically the quadrupole, which we will discuss in Sect. 6.2.3, and $50 \lesssim \ell \lesssim 100$. In the latter, the Cosmoglobe multipoles are consistently $\geq 5\%$ higher than the Λ CDM solution.

At $\ell \gtrsim 500$, the WMAP9 solution becomes noise dominated, and there is much larger variation between the multipoles. While *Planck* and BEYONDPLANCK mostly agree with the Cosmoglobe solution, the convergence properties of the power spectrum are much worse, and would require an order of magnitude more samples to converge (Colombo et al. 2022). We therefore caution against overinterpreting the specific values from the Cosmoglobe power spectrum in this regime.

6.2.3. Low- ℓ anomalies

Even though the CMB is well described by Λ CDM, there are several anomalies, especially at low multipoles, that seem to be in tension with Λ CDM. As a rule, the existence of these anomalies is not debated, but rather their significance within Λ CDM. Indeed, as argued by Bennett et al. (2011), the existence of these anomalies may simply be described by the look-elsewhere effect. The relevant question is not “How unlikely is Λ CDM given this effect?” but rather “How unlikely is this effect given Λ CDM?”.

In standard analysis of CMB anomalies, one computes the traditional maximum-likelihood maps of the CMB and generate a single value for each of the anomaly statistics. One then compares these values to simulations of the Λ CDM in a frequentist approach to see how rare it is for a random realization of the CMB to exhibit the anomalies.

In our case, we have a set of CMB maps output from the Gibbs chain, which we use to create histograms of these statistics. As such, we have full control over systematic uncertainties of the low- ℓ anomalies which is difficult in traditional approaches. This allows us to answer the question of whether the

anomalies actually are in our CMB, or if previous measurements of the CMB simply have not accounted for all systematic effects.

This section will look at some of statistics of well-known the low- ℓ anomalies and compare our findings with the previous results in the BEYONDPLANCK analysis in Colombo et al. (2022). This will tell us how much more information is gained about these anomalies by including the WMAP dataset in addition to *Planck* LFI.

It has been noted since COBE-DMR that the quadrupole amplitude of our CMB is lower than expected from Λ CDM (Bennett et al. 1992). This has later been confirmed by WMAP (Hinshaw et al. 2003) and *Planck* (Planck Collaboration Int. XV 2014), but with large discrepancies in mean value and error bars.

The WMAP team found in the 7-year analysis a best-fit value of $201 \mu\text{K}^2$ (Larson et al. 2011) which dropped to $151 \mu\text{K}^2$ in the 9-year analysis (Hinshaw et al. 2013). The naive Fisher uncertainty on σ_2 was reported by Hinshaw et al. (2013) to be $9 \mu\text{K}^2$ which only accounted for a noise-only estimate. This error bar corresponds to a roughly 5σ discrepancy.

Planck later found in 2013 and 2018 σ_2 to be 299 and $226 \mu\text{K}^2$, respectively, with a naive Fisher uncertainty yielded a 8σ discrepancies (Planck Collaboration V 2020). This shows that measuring σ_2 is difficult and that instrumental white-noise is not the dominant source of uncertainty.

With the set of Cosmoglobe maps of the CMB we can quantify the marginal posterior distribution $P(\sigma_2 | \mathbf{d})$, and we show posterior distribution represented as a Gaussian with $\sigma_2 = 133 \pm 70 \mu\text{K}^2$ in Fig. 33. Despite the fact that Cosmoglobe also incorporates the LFI dataset, this is an 8-fold of the WMAP Fisher uncertainty. This proves why one needs to take instrumental and astrophysical parameters into account when measuring σ_2 . Fig. 33 compares the Cosmoglobe results with BEYONDPLANCK which found $\sigma_2 = 229 \pm 97 \mu\text{K}^2$, showing that the inclusion of WMAP significantly lowers the measured value of σ_2 . We also show 10^5 realizations of σ_2 given Planck 2018 best-fit $C_2^{\Lambda\text{CDM}} = 1064.6 \mu\text{K}^2$.

To get a better understanding of how anomalous σ_2 is, we can ask what the probability of C_2 be large given our set of measured σ_2 . This can be done by applying the Blackwell-Rao esti-

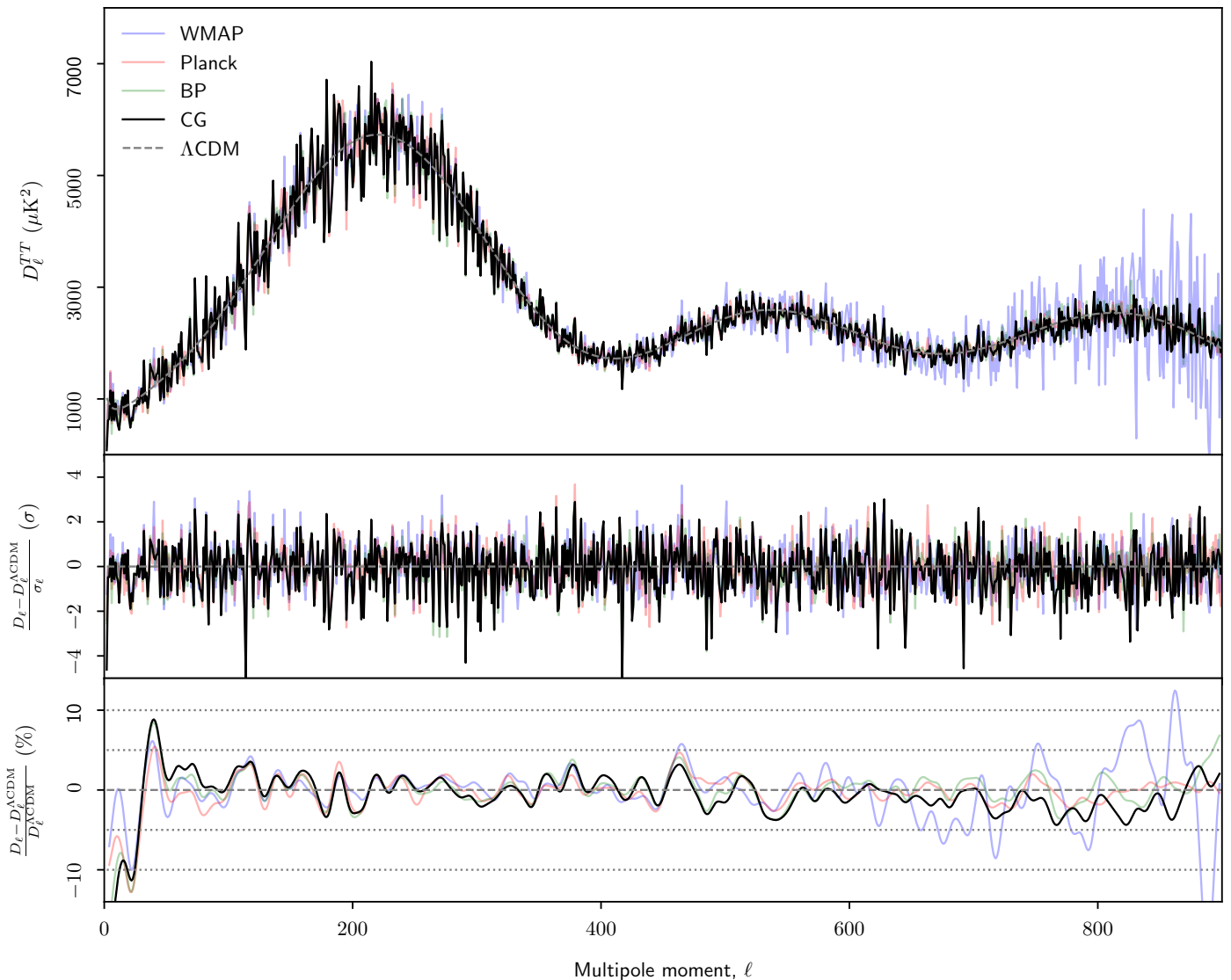


Fig. 32. (Top:) Angular CMB temperature power spectrum, D_ℓ^{TT} , as derived by COSMOGLOBE (black), BEYONDPLANCK (green), *Planck* (red), and *WMAP9* (blue). The best-fit *Planck* 2018 Λ CDM spectrum is showed in dashed gray. (Middle:) Residual power spectrum relative to Λ CDM, measured relative to the quoted error bars, $(D_\ell - D_\ell^{\Lambda\text{CDM}})/\sigma_\ell$. For pipelines that report asymmetric error bars, σ_ℓ is taken to be the average of the upper and lower error bar. (Bottom:) Fractional difference with respect to the *Planck* Λ CDM spectrum. In this panel, each curve has been boxcar averaged with a window of $\Delta\ell = 100$ to suppress random fluctuations.

mator described by Chu et al. (2005). We map out the marginal posterior distribution $P(C_2 | \sigma_2)$ as a function of C_2 and mark where $C_2^{\Lambda\text{CDM}} = 1064.6 \mu\text{K}^2$ by a grey vertical line. We show this in Fig. 34 find that the probability for C_2 to exceed $C_2^{\Lambda\text{CDM}}$ to be 11.3 % for COSMOGLOBE (LFI + *WMAP*) and 21.7 % for BEYONDPLANCK (LFI) shown as shaded areas.

6.3. χ^2 and map space residuals

The quality of the component separation procedure is evaluated through a reduced- χ^2 map, shown in Fig. 38, as well as through the map space residuals Fig. B.6. Figure 38 shows a sum of all three Stokes parameters, and we can see, morphologically, that the poorly fit parts of the sky are driven by structures associated with features in total intensity. The poorly fit pixels are generally constrained to the Galactic plane, mostly at the Galactic center, though we note some poor fits in regions such as the Orion region, ρ Ophiucus, and Large Magellanic Cloud. Future work to

find a more complete model of AME will likely help clean up this picture.

6.4. WMAP-versus-LFI signal-to-noise ratio comparison

7. Outstanding issues

As shown in the previous sections, there are very few residuals, artifacts, or systematics within this jointly processed dataset, hereafter referred to as COSMOGLOBE data release 1 (CG1). However, the global nature of this analysis allows us to identify issues in the data processing that will otherwise have gone unnoticed. In this section, we enumerate the issues we have encountered in CG1, and which we plan to improve upon in future data releases.

7.1. Noise modeling

As demonstrated in Sect. 4.4, the χ^2 per TOD scan was discrepant up to the 10σ level. The main driver of this model failure

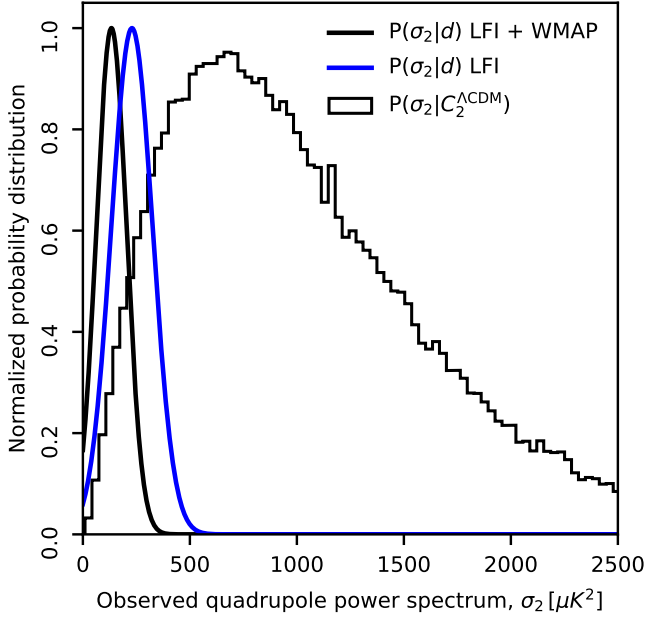


Fig. 33. Histogram of 100 000 realizations of potential realizations σ_2 given $C_2^{\Lambda\text{CDM}} = 1064.7 \mu\text{K}^2$ compared with the measured power spectrum σ_2 of our universe for COSMOGLOBE (black) and BEYONDPLANCK (blue).

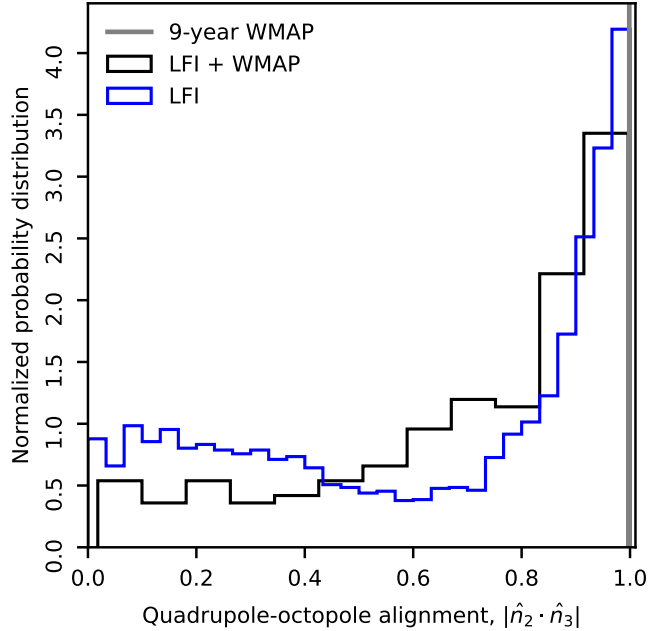


Fig. 35. The quadrupole-octopole alignment of COSMOGLOBE compared with BEYONDPLANCK and 9-year WMAP.

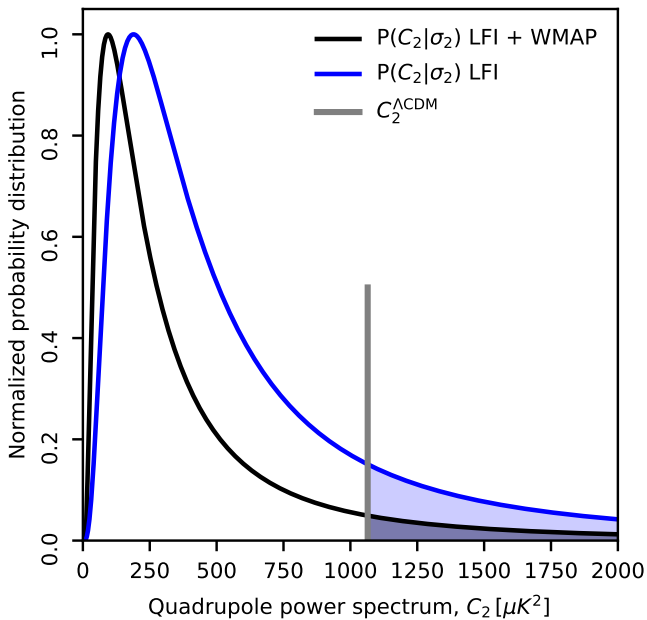


Fig. 34. Marginal probability distribution of the ensemble-averaged C_2 given the data, $P(C_2 | d)$, as measured by COSMOGLOBE (black) and BEYONDPLANCK (blue).

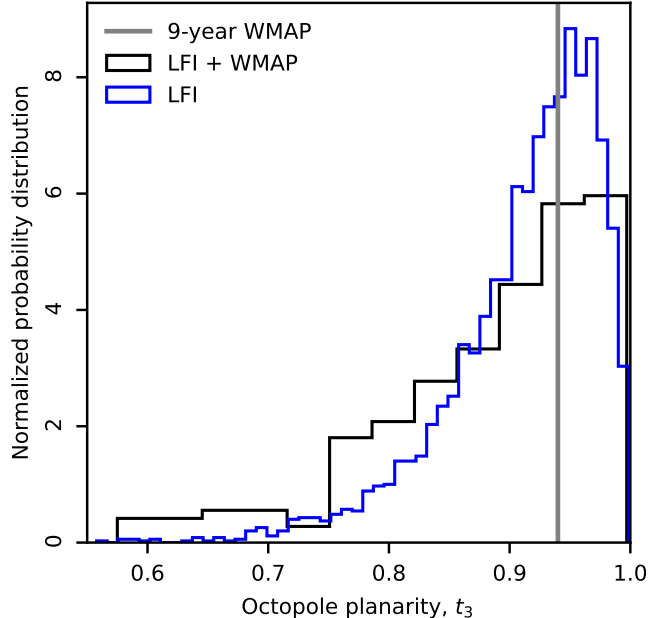


Fig. 36. The octopole planarity statistics t_3 compared with the BEYONDPLANCK analysis (blue).

intermediate frequencies 2–6 Hz at the expense of a good fit at the highest frequencies.

The particular case of *W413*'s PSD is a noise spectrum that could easily be modeled as a spectrum that is continuing to drop beyond the sampling rate, not dissimilar to the two-pole Bessel filter implemented in *WMAP*'s electronics (Jarosik et al. 2003b). In practice, the white noise can be identified with the flat portion of the spectrum well above f_{knee} , but in the case of these noise spectra, there is no such flat portion, challenging the very existence of “white noise” for this particular radiometer. Addi-

is in the noise modeling, and in particular the incompleteness of a power law correlated noise model. In practice, this is due to the algorithmic choice to not fit the white noise level as a parameter on the same footing as all other noise parameters. Inspecting Fig. 9 shows that the high-frequency noise is essentially fixed to the noise PSD at the sampling frequency. If σ_0 were a free parameter in this particular parametric fit, it would be driven by the

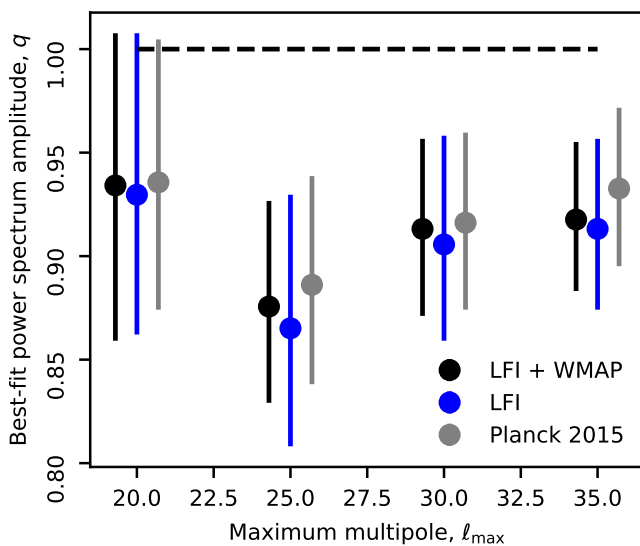


Fig. 37. Best-fit amplitude, q , of the low multipole power spectrum $C_\ell = qC_\ell^{\Lambda\text{CDM}}$, $2 \leq \ell \leq \ell_{\text{max}}$ compared to *Planck* 2015 (grey) and BeyondPlanck (blue).

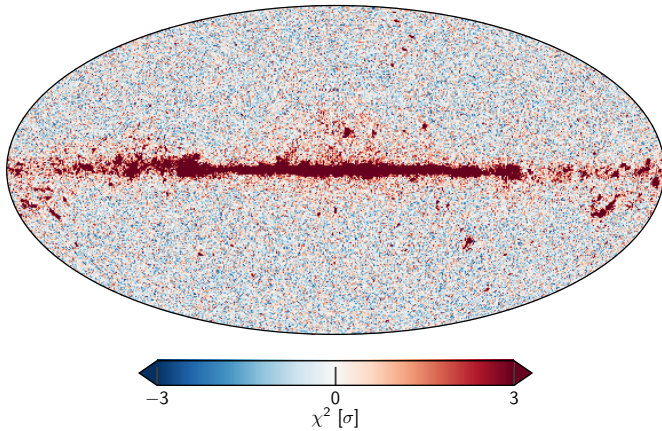


Fig. 38. Reduced- χ^2 , using $n_{\text{dof}} = 300$, which comes from fitting to the regions outside of the K -band processing mask.

tionally, a Bessel filter tail could affect the signal band as well, requiring more detailed modeling of the noise.

In practice, the decomposition of instrumental noise into a “white” component and a correlated component is very useful, and provides a stringent test for the final data products. Indeed, the particular model failure was so subtle that such a description of noise being split into scale-dependent and scale-independent would have made it nearly impossible to detect such an issue. For the case of *WMAP* data, there is a natural need to improve the noise PSD modeling, especially when a successful parameterization was found by the *WMAP* team in time space. In practice, this will likely be useful for the analysis of other CMB experiments, and will be of broad use in the future.

7.2. V- and W-band quadrupole residual

As mentioned in Sect. ??, there is a $2 \mu\text{K}$ quadrupolar residual in the V -band and W -band residuals that is aligned with the ecliptic pole, and roughly perpendicular to the Solar dipole. As this quadrupole does not exist in lower DAs, and V - and W -bands

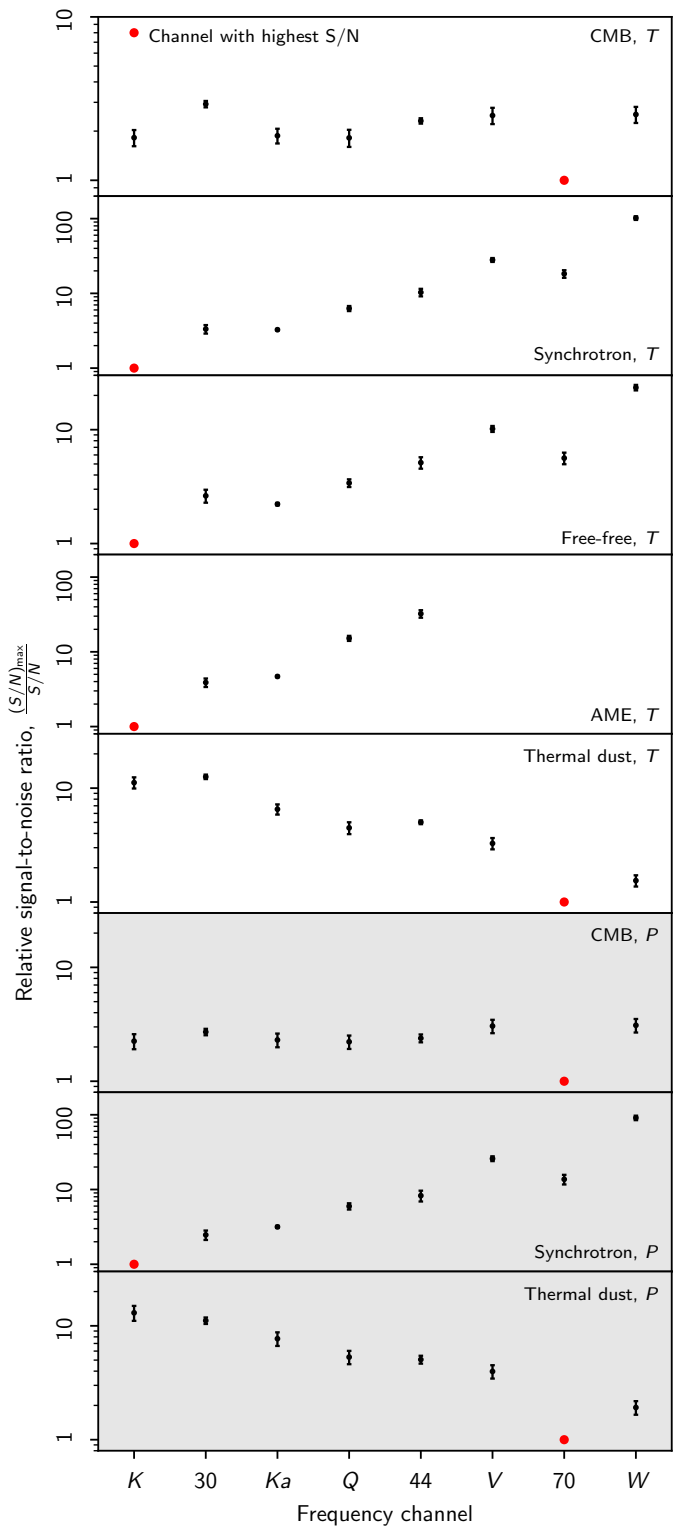


Fig. 39. Relative signal-to-noise ratios for *WMAP* and LFI channels and various components.

have gains that are consistent with *WMAP*’s at the 1 % level, it is more likely that there is a subtle error in the data processing.

In an early stage of this analysis, a large quadrupolar signal was induced due to an error in the orbital dipole calculation. Essentially, a single satellite velocity was assumed for an entire scan, which proved to be a poor approximation over ~ 3 -day pe-

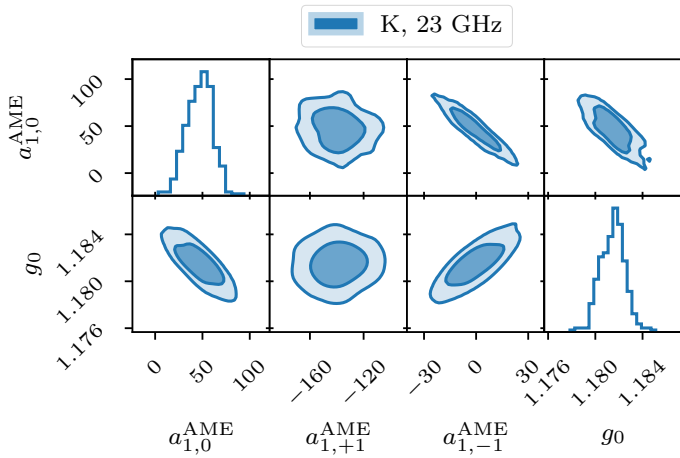


Fig. 40. Correlation between K -band's absolute calibration g_0 [du mK^{-1}] and AME dipole's spherical harmonic coefficients [μK_{RJ}].

riod. A linear interpolation between scans fixed this issue, and a cubic interpolation provided a negligible improvement.

This points generally to long-timescale effects causing quadrupolar signals. A similar issue, an $8\,\mu\text{K}$ dipole, was discovered by [Jarosik et al. \(2007\)](#), and determined to be due to an inadequacy in the gain model. As mentioned earlier, we assume a linear baseline trend throughout a given scan, and allow correlated noise residuals to pick up longer scale fluctuations. Compared to the *WMAP* team's approach of fitting cubic polynomials every hour, there is much more room for unmodeled temporal variation in zero-level. As the gain, correlated noise, and baseline are all deeply correlated, a subtle error in the baseline determination could easily induce a small quadrupolar signal.

7.3. Degeneracy between K -band calibration and AME dipole

As discussed in Sect. 2.5, there is a strong degeneracy between K -band's absolute calibration and the AME dipole that requires external information to break. In this work, we implemented a prior on the absolute calibration based on the effect it had on the best-fit AME dipole. In the posterior distribution, a slice of which is shown in Fig. 40, we can specifically compare K -band's absolute calibration with the AME dipole values. Here the degeneracy between g_0 and $a_{1,\pm 1}^{\text{AME}}$ is quite apparent. Because there is no causal connection between K -band's absolute gain and the AME dipole, a prior was necessary for the analysis in this work to return sensible results.

In the official *WMAP* pipeline, the degeneracy was effectively broken by using a preliminary K -band sky map and removing it from the timestream. In practice, both solutions are the result of scientific intuition solving an algorithmic issue. The COSMOGLOBE approach of using a prior on g_0 comes from the strong prior that Galactic emission should not have a dipole aligned with the CMB's Solar dipole. The *WMAP* team's approach of using a previous iteration's map as a sky model comes from the strong prior that errors in the first iteration of the sky map are uncorrelated with the orbital dipole in the timestream.

While the COSMOGLOBE K -band gain solution is driven by our prior belief in the size of the AME dipole, the overall instrumental solution generates maps that are consistent with our sky model at the $1\,\mu\text{K}$ level at high Galactic latitudes. Conversely, the *WMAP9* solution does not rely on any knowledge of the sky,

but as a result induces poorly measured modes with a $2.5\,\mu\text{K}$ amplitude.

Regardless of the details, an accurate model of the sky as observed by K -band is a necessary condition to obtaining an accurate measurement of the gain. The difficulty of obtaining an accurate AME model is of course compounded by the fact that the AME is brighter in K -band than any of the *WMAP* or *Planck* bands. This may be mitigated in the near future, following a joint *WMAP*+LFI+QUIJOTE analysis, but this of course depends on the signal-to-noise of AME in QUIJOTE's frequencies, and is further hindered by QUIJOTE's partial sky coverage.

A future analysis involving the most robust parts of the *WMAP9* and COSMOGLOBE analysis also has the potential to solve the g_0 -ALM degeneracy. In particular, the COSMOGLOBE analysis did not directly use the housekeeping data to estimate the gain model. There is no a priori reason that the parameters in Eq. (47) cannot be included in the Gibbs chain. This would of course require detailed knowledge of the *WMAP* satellite's hardware only held by the core *WMAP* team. We hope that a joint effort between the *WMAP* team and COSMOGLOBE will help to solve this outstanding issue.

7.4. Other minor effects

The issues listed above are known problems in the analysis that will be fixed in the future. Below, we discuss parts of the analyses that we know exist, but have not yet made an attempt to correct because they have not posed direct problems yet.

7.4.1. Time-variable bandpass modeling

The *WMAP* team discovered year-to-year variations in the Galactic plane of the K , Ka , Q , and V maps ([Bennett et al. 2013](#), Appendix A). They determined that the central frequency drifted by 0.13 %, 0.12 %, 0.11 %, and 0.06 %, respectively, with a maximum jump of $\sim 0.01\%$. This was not incorporated in the *WMAP9* mapmaking, as each year of data were processed separately, so that each map could be considered to have a single effective frequency.

The COSMOGLOBE mapmaking procedure has incorporated no correction for this effect. In principle, this could be problematic, as the relative gain solution is obtained by comparing to a bandpass-integrated map of the sky for each DA. However, we have not noticed a sign of this in our analyses, in large part because so much of the sky signal is dominated by the Solar dipole, whose amplitude is not affected by bandpass shifts.

This effect could potentially be modeled using the housekeeping data, as [Bennett et al. \(2013\)](#) posit that the instrument's physical temperature changes may have induced changes in the onboard electronics causing the bandpass shift. In this way we could model the bandpass shift and modify the sky model as a function of scan. Ideally, a parametric model for the bandpass shift would be implemented and then sampled for as part of the Gibbs chain. Practically, this effect is subdominant to all other effects we have described in this work, and will not be a priority for the foreseeable future. That said, time variation in the effective bandpass could induce spurious polarization signals in future experiments attempting to measure the tensor-to-scalar ratio r . In this context, a full understanding of the temporal dependence on *WMAP*'s bandpass would be invaluable as preparation for the data analysis of future experiments.

7.4.2. Polarized sidelobe modeling

As shown by Barnes et al. (2003) and Watts et al. (2022), unpolarized sky signals can generate spurious polarized signals, through radiometer mismatch and transmission imbalance, respectively. Barnes et al. (2003) also reported the results from lab-based measurements, in which the differential polarized pickup from horns A and B were quantified. Polarized sidelobes could in principle channel a polarized sky signal into the final maps, but Barnes et al. (2003) reported that the radiometer mismatch signal dominated the sky across all regions except the Galactic center.

Practically, the polarized sidelobe response has never been published, thus making the relevant calculation impossible to carry out without the relevant laboratory measurements and results. The current location of these data, or even their continued existence, has not yet been determined. As the *WMAP* team has not mentioned polarized sidelobe pickup of the polarized sky since Barnes et al. (2003) and the location of the polarized pickup maps is unknown, we believe that further research regarding this subject would outweigh its potential benefits.

8. Conclusions

In this paper, we have produced an analysis of the *WMAP* data from TOD to power spectra, as well as the first joint end-to-end experiment analysis as part of the COSMOGLOBE project. In addition to reproducing the temperature analysis, the polarization maps produced by COSMOGLOBE have no detectable poorly measured modes. Based on properties of the data in TOD space, map space, and power spectrum space, we recommend that scientists studying the microwave sky below 90 GHz use COSMOGLOBE’s *WMAP* maps rather than the *WMAP9* maps.

Much of the improvement in the final maps came from using a global framework, conditioning timestreams on a predicted sky model. The gain model obtained through this approach was within 1 % of the *WMAP9* calibration, despite both approaches using a completely independent calibration method. In addition, the parametric noise model we used obtained knee frequencies consistent with the values reported in the *WMAP* first-year analysis, and tracks temporal variations in the noise properties on shorter timescales than consider by the *WMAP* team. In addition, the transmission imbalance parameters are consistent within the *WMAP9* error budget, but we find up to 8σ discrepancies in the mean value. Finally, we are able to track the goodness of fit per scan for each individual radiometer, and find that the raw χ^2 is within 0.3 % of n_{TOD} throughout the entire mission.

In the map domain, we produce Stokes T , Q , and U maps, with the expected bandpass mismatch removed in the timestream. The temperature maps are consistent between *WMAP9* and COSMOGLOBE at the $2.5 \mu\text{K}$ level, mainly in the form of dipoles due to absolute gain differences and quadrupoles likely due to baseline and gain treatment. In polarization, the difference of up to $\sim 10 \mu\text{K}$ is due to the poorly measured modes identified by the *WMAP* team. Through internal difference maps, we show that these modes arise only from the *WMAP9* maps, and are absent from all COSMOGLOBE maps. In power spectrum space, we find that the *WMAP9* and COSMOGLOBE temperature power spectra agree at the $\lesssim 5\%$ level at all angular scales, while the E -mode and B -mode power spectra from COSMOGLOBE are much better behaved for nearly every multipole.

When we compare to *Planck* LFI data, the polarization maps agree well when we compare to the nearest frequency bands, and the large scale anomalous differences that have plagued the LFI

and *WMAP* comparisons have been reduced to below the level of white noise and Galactic modeling. The progression fo comparisons between *K*-band and *Planck* 30 GHz in Fig. 41 shows that the large scale agreement has been reduced by over an order of magnitude, to the extent that no special treatment is required to compare these datasets.

Finally, we directly address the question of whether the transmission imbalance templates are accurately projected out of the final *WMAP9* maps by fitting the delivered templates to the $N_{\text{side}} = 16$ difference maps. We find that at most half of the large-scale difference between COSMOGLOBE and *WMAP9* can be described by fitting these templates. As these poorly measured modes exist only in the *WMAP9* maps, it is likely that these templates, used in the *WMAP9* cosmological likelihood, did not correctly account for these modes in the final *WMAP9* cosmological analysis.

Our astrophysical results are largely consistent with the previous BEYONDPLANCK, *Planck*, and *WMAP9* results. Two notable exceptions to this are in the amplitude of the Solar dipole and the temperature quadrupole. In particular, the Solar dipole’s amplitude of $3366.2 \pm 1.4 \mu\text{K}$ is higher than both the BEYONDPLANCK and *WMAP9* values, agreeing mostly with the *Planck* DR4 value. At the same time, the quadrupole amplitude $\sigma_2 = 133 \pm 70 \mu\text{K}^2$, consistent with the ΛCDM prediction at the 11.3 % level, compared with the 21.7 % level of BEYONDPLANCK.

The sky model, as quantified by the χ^2 per $N_{\text{side}} = 128$ pixel, is consistent with noise across the sky in all regions except for those with large emission, such as the Galactic plane and prominent radio point sources. While this does point to a need to improve parametric modeling of the Galactic sky, the discrepancy of these regions is fully consistent with all modern analyses, and will continue to be a subject of active research for the foreseeable future. In particular, the failure of the sky model to match the data in this regions is specifically used to identify regions in which we cannot calibrate the gain, and so explicitly are prevented from affecting the calibration solution.

This paper is the first time that the LFI polarization data have successfully reproduced an estimate of the sky as measured by the *WMAP* data. Each row of Fig. 41 can be considered a different attempt for *Planck* LFI to reproduce *WMAP*, by comparing the rescaled *K*-band of *WMAP* to the *Planck* 30 GHz map. The large-scale residuals have been reduced by at least an order of magnitude, with the largest residual along the Galactic plane, where the simple $\beta_s = -3.1$ scaling is inadequate.

The agreement between the LFI and *WMAP* maps is a success of the modern scientific method. By using both public data and public pipelines, we have been able to create a coherent model of the sky and the instruments that observed the sky. As best as possible given the white noise levels and angular resolutions, the maps produced here are faithful representations of the sky that should require no special treatment to interpret correctly.

Most importantly, the results presented here would not have been possible without a joint analysis in some framework. As stated implicitly in Sect. 1, virtually every CMB experiment is indirectly using an external prior of $T_0 = 2.72548 \text{ K} \pm 0.57 \text{ mK}$ (Fixsen 2009) – put another way, all CMB maps are produced by calibrating against the internal blackbody aboard COBE-FIRAS. The results presented here are a logical extension of this approach. The joint analysis of two data sets forces us understand differences within the analysis pipeline rather than performing a post hoc argument for whether one dataset is analyzed correctly or the other. We argue that only through resolving the differences between conflicting datasets can the full scientific throughput of existing datasets be obtained.

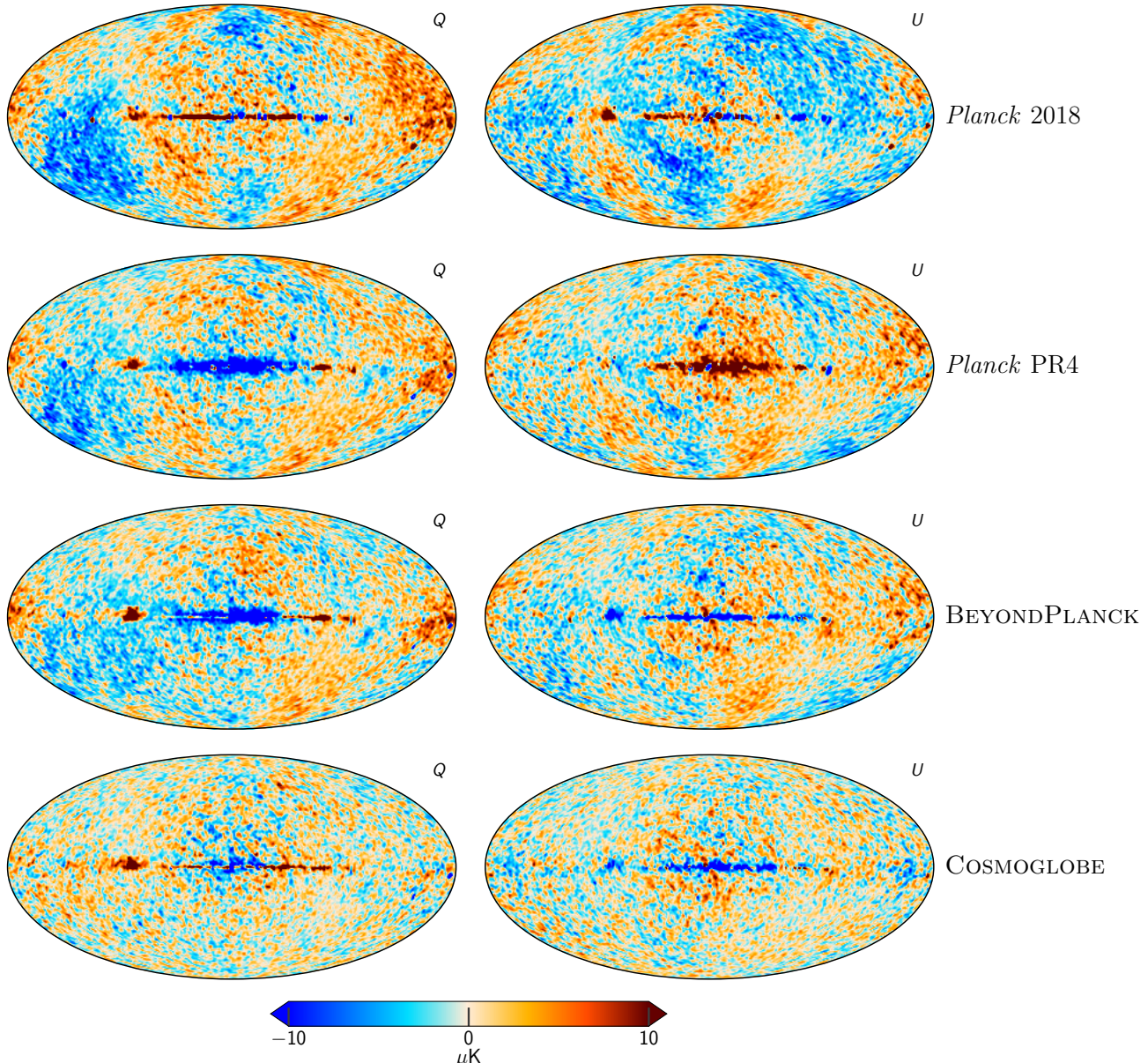


Fig. 41. Difference maps between the *Planck* 30 GHz and *WMAP* K-band maps. The columns are (1) *Planck* 2018 v. *WMAP*9, (2) *Planck* PR4 v. *WMAP*9, (3) BEYONDPLANCK v. *WMAP*9, and (4) COSMOGLOBE *Planck* 30 GHz and *WMAP* K-band both produced in this paper. All maps have been smoothed to a common resolution of 2° FWHM, and the K-band map has been scaled by 0.495 to account for different central frequencies, assuming a synchrotron spectral index $\beta_s = -3.1$.

Acknowledgements. We thank the entire *Planck* and *WMAP* teams for invaluable support and discussions, and for their dedicated efforts through several decades without which this work would not be possible. The current work has received funding from the European Union’s Horizon 2020 research and innovation programme under grant agreement numbers 776282 (COMPET-4; BEYONDPLANCK), 772253 (ERC; bRIS2COSMOLOGY), and 819478 (ERC; COSMOGLOBE). In addition, the collaboration acknowledges support from ESA; ASI and INAF (Italy); NASA and DoE (USA); RCN (Norway; grant nos. 263011, 274990); and PRACE (EU). We acknowledge the use of the Legacy Archive for Microwave Background Data Analysis (LAMBDA), part of the High Energy Astrophysics Science Archive Center (HEASARC). HEASARC/LAMBDA is a service of the Astrophysics Science Division at the NASA Goddard Space Flight Center. Some of the results in this paper have been derived using the `healpy` and `HEALPix`⁸ packages (Górski et al. 2005; Zonca et al. 2019). This work made use of Astropy⁹: a community-developed core Python package and an ecosystem of tools and resources for astronomy (Astropy Collaboration et al. 2013, 2018, 2022).

References

- Ali-Haïmoud, Y. 2010, Astrophysics Source Code Library [ascl:1010.016]
- Ali-Haïmoud, Y., Hirata, C. M., & Dickinson, C. 2009, MNRAS, 395, 1055
- Alonso, D., Sanchez, J., Slosar, A., & LSST Dark Energy Science Collaboration. 2019, MNRAS, 484, 4127
- Andersen et al. 2022, A&A, in press [arXiv:2201.08188]
- Astropy Collaboration, Price-Whelan, A. M., Lim, P. L., et al. 2022, apj, 935, 167
- Astropy Collaboration, Price-Whelan, A. M., Sipőcz, B. M., et al. 2018, AJ, 156, 123
- Astropy Collaboration, Robitaille, T. P., Tollerud, E. J., et al. 2013, A&A, 558, A33
- Barnes, C., Hill, R. S., Hinshaw, G., et al. 2003, ApJS, 148, 51
- Barrett, R., Berry, M. W., Chan, T. F., et al. 1994, Templates for the Solution of Linear Systems (Society for Industrial and Applied Mathematics)
- Basyrov et al. 2022, A&A, submitted [arXiv:2208.14293]
- Bennett, C. L., Bay, M., Halpern, M., et al. 2003a, ApJ, 583, 1
- Bennett, C. L., Halpern, M., Hinshaw, G., et al. 2003b, ApJS, 148, 1
- Bennett, C. L., Hill, R. S., Hinshaw, G., et al. 2011, ApJS, 192, 17

⁸ <http://healpix.sf.net>

⁹ <http://www.astropy.org>

- Bennett, C. L., Larson, D., Weiland, J. L., et al. 2013, ApJS, 208, 20
 Bennett, C. L., Smoot, G. F., Hinshaw, G., et al. 1992, ApJ, 396, L7
 BeyondPlanck. 2022, A&A, submitted [arXiv:2011.05609]
 Chu, M., Eriksen, H. K., Knox, L., et al. 2005, Phys. Rev. D, 71, 103002
 Colombo et al. 2022, A&A, submitted [arXiv:2208.14276]
 Delouis, J. M., Puget, J. L., & Vibert, L. 2021, A&A, 650, A82
 Dicke, R. H., Peebles, P. J. E., Roll, P. G., & Wilkinson, D. T. 1965, ApJ, 142, 414
 Dickinson, C., Davies, R. D., & Davis, R. J. 2003, MNRAS, 341, 369
 Fixsen, D. J. 2009, ApJ, 707, 916
 Frigo, M. & Johnson, S. G. 2005, Proceedings of the IEEE, 93, 216, special issue on “Program Generation, Optimization, and Platform Adaptation”
 Galloway et al. 2022a, A&A, in press [arXiv:2201.03509]
 Galloway et al. 2022b, A&A, in press [arXiv:2201.03478]
 Gjerløw et al. 2022, A&A, submitted [arXiv:2011.08082]
 Górski, K. M., Hivon, E., Banday, A. J., et al. 2005, ApJ, 622, 759
 Greason, M. R., Limon, M., Wollack, E., et al. 2012, Nine-Year Explanatory Supplement, 5th edn. Greenbelt, MD: NASA/GSFC
 Hensley, B., Murphy, E., & Staguhn, J. 2015, MNRAS, 449, 809
 Hill, R. S., Weiland, J. L., Odegard, N., et al. 2009, ApJS, 180, 246
 Hinshaw, G., Barnes, C., Bennett, C. L., et al. 2003, ApJS, 148, 63
 Hinshaw, G., Larson, D., Komatsu, E., et al. 2013, ApJS, 208, 19
 Hinshaw, G., Nolta, M. R., Bennett, C. L., et al. 2007, ApJS, 170, 288
 Hinshaw, G., Weiland, J. L., Hill, R. S., et al. 2009, ApJS, 180, 225
 Hu, W., Fukugita, M., Zaldarriaga, M., & Tegmark, M. 2001, ApJ, 549, 669
 Ihle et al. 2022, A&A, in press [arXiv:2011.06650]
 Jarosik, N., Barnes, C., Bennett, C. L., et al. 2003a, ApJS, 148, 29
 Jarosik, N., Barnes, C., Greason, M. R., et al. 2007, ApJS, 170, 263
 Jarosik, N., Bennett, C. L., Dunkley, J., et al. 2011, ApJS, 192, 14
 Jarosik, N., Bennett, C. L., Halpern, M., et al. 2003b, ApJS, 145, 413
 Lange, A. E., Ade, P. A., Bock, J. J., et al. 2001, Phys. Rev. D, 63, 042001
 Larson, D., Dunkley, J., Hinshaw, G., et al. 2011, ApJS, 192, 16
 Larson, D., Weiland, J. L., Hinshaw, G., & Bennett, C. L. 2015, ApJ, 801, 9
 Lineweaver, C. H., Tenorio, L., Smoot, G. F., et al. 1996, ApJ, 470, 38
 Mather, J. C., Cheng, E. S., Cottingham, D. A., et al. 1994, ApJ, 420, 439
 Mather, J. C., Fixsen, D. J., Shafer, R. A., Mosier, C., & Wilkinson, D. T. 1999, ApJ, 512, 511
 Notari, A. & Quartin, M. 2015, Journal of Cosmology and Astroparticle Physics, 2015, 047–047
 Page, L., Jackson, C., Barnes, C., et al. 2003, ApJ, 585, 566
 Paradiso et al. 2022, A&A, submitted [arXiv:2205.10104]
 Penzias, A. A. & Wilson, R. W. 1965, ApJ, 142, 419
 Planck Collaboration I. 2016, A&A, 594, A1
 Planck Collaboration II. 2016, A&A, 594, A2
 Planck Collaboration VIII. 2016, A&A, 594, A8
 Planck Collaboration IX. 2016, A&A, 594, A9
 Planck Collaboration X. 2016, A&A, 594, A10
 Planck Collaboration I. 2020, A&A, 641, A1
 Planck Collaboration II. 2020, A&A, 641, A2
 Planck Collaboration III. 2020, A&A, 641, A3
 Planck Collaboration IV. 2018, A&A, 641, A4
 Planck Collaboration V. 2020, A&A, 641, A5
 Planck Collaboration Int. XV. 2014, A&A, 565, A103
 Planck Collaboration Int. XLVI. 2016, A&A, 596, A107
 Planck Collaboration Int. LVII. 2020, A&A, 643, A42
 Planck Collaboration LVII. 2020, A&A, 643, A42
 Press, W. H., Teukolsky, S. A., Vetterling, W. T., & Flannery, B. P. 2007, Numerical Recipes 3rd Edition: The Art of Scientific Computing, 3rd edn. (USA: Cambridge University Press)
 Remazeilles, M., Dickinson, C., Banday, A. J., Bigot-Sazy, M.-A., & Ghosh, T. 2015, MNRAS, 451, 4311
 Rubiño-Martín, J. A., Guidi, F., Génova-Santos, R. T., et al. 2023, MNRAS, 519, 3383
 Rudjord, Ø., Groeneboom, N. E., Eriksen, H. K., et al. 2009, ApJ, 692, 1669
 Shewchuk, J. R. 1994, An Introduction to the Conjugate Gradient Method Without the Agonizing Pain, Edition 1 $\frac{1}{4}$, <http://www.cs.cmu.edu/~quake-papers/painless-conjugate-gradient.pdf>
 Silsbee, K., Ali-Haïmoud, Y., & Hirata, C. M. 2011, MNRAS, 411, 2750
 Smoot, G. F., Bennett, C. L., Kogut, A., et al. 1992, ApJ, 396, L1
 Stevenson, M. A. 2014, The Astrophysical Journal, 781, 113
 Svalheim et al. 2022a, A&A, in press [arXiv:2201.03417]
 Svalheim et al. 2022b, A&A, in press [arXiv:2011.08503]
 Thommesen, H., Andersen, K. J., Aurlien, R., et al. 2020, A&A, 643, A179
 van der Vorst, H. A. 1992, SIAM Journal on Scientific and Statistical Computing, 13, 631
 Watts et al. 2022, A&A, in press [arXiv:2202.11979]
 Watts et al. 2023, A&A, in preparation [arXiv:20xx.xxxxx]
 Weiland, J. L., Odegard, N., Hill, R. S., et al. 2011, ApJS, 192, 19
 Zonca, A., Singer, L., Lenz, D., et al. 2019, Journal of Open Source Software, 4, 1298

Appendix A: Survey of instrumental parameters

In this Appendix, we provide for reference purposes a complete survey of the posterior mean estimates for all time-dependent instrumental parameters. In each figure, columns correspond to individual diodes, while rows correspond to DA. Figure A.1 shows the zeroth order baseline (plotted as the difference between the full time-variable baseline and its own time average), while Fig. A.2 shows the corresponding baseline slopes. Figure A.3 shows the full time-dependent gain, and Fig. A.4 shows the fractional gain difference between COSMOGLOBE and WMAP in units of percent. Figures A.5–A.7 shows the noise model parameters, σ_0 , f_{knee} , and α , respectively. Finally, Fig. A.8 shows the TOD-level reduced normalized χ^2 in units of standard deviation. Black lines show COSMOGLOBE results, while solid red lines show (where available) official WMAP results derived by linear regression between the raw and calibrated WMAP TODs. Orange and red dotted lines show WMAP first-year in-flight and GSFC laboratory measurements, respectively. For further discussion regarding these plots, see Sect. 4.

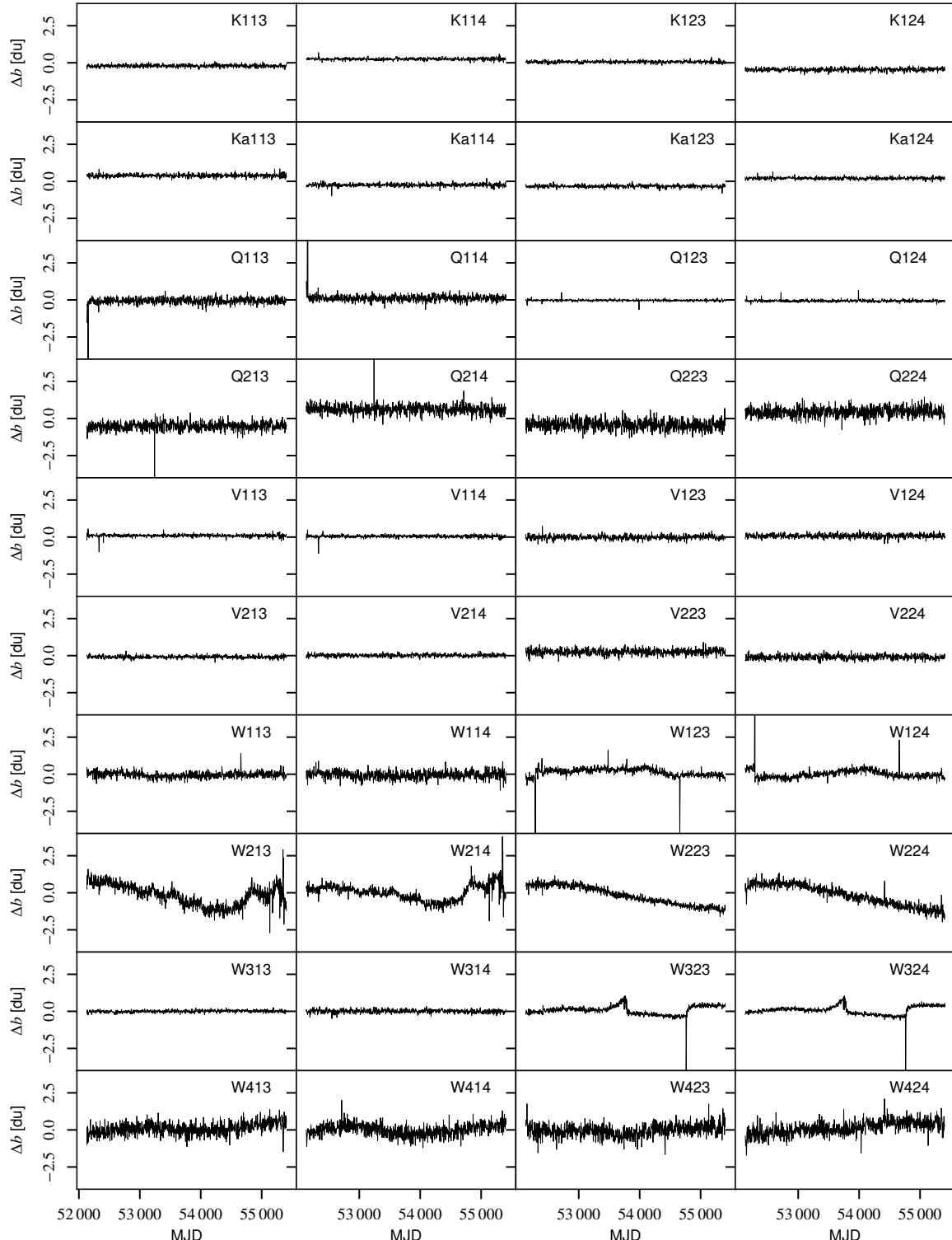


Fig. A.1. Difference in zero-level baseline between COSMOGLOBE and WMAP9, $b_0^{\text{CG}} - b_0^{\text{WMAP}}$.

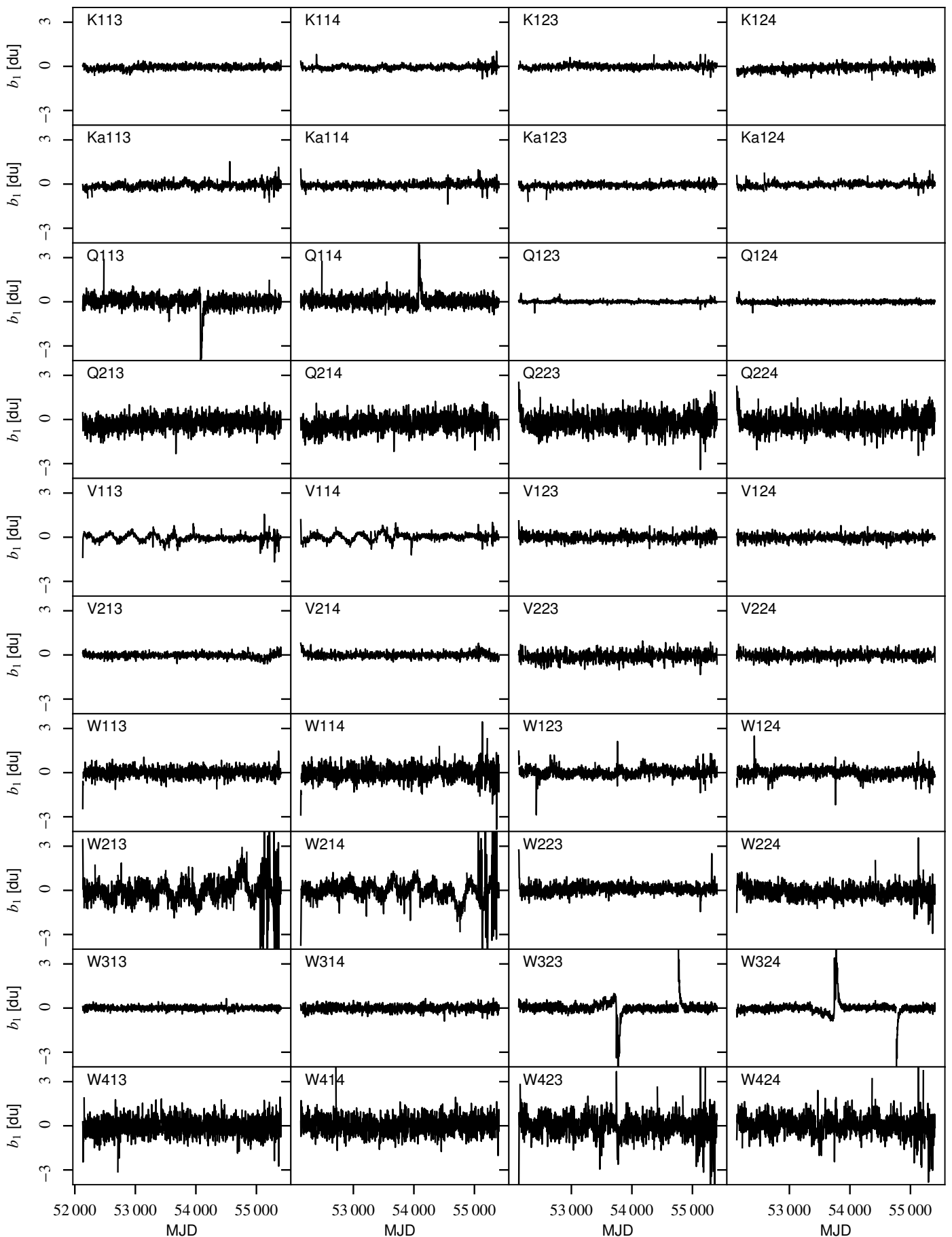


Fig. A.2. COSMOGLOBE first-order baseline correction (i.e., slope) for each diode.

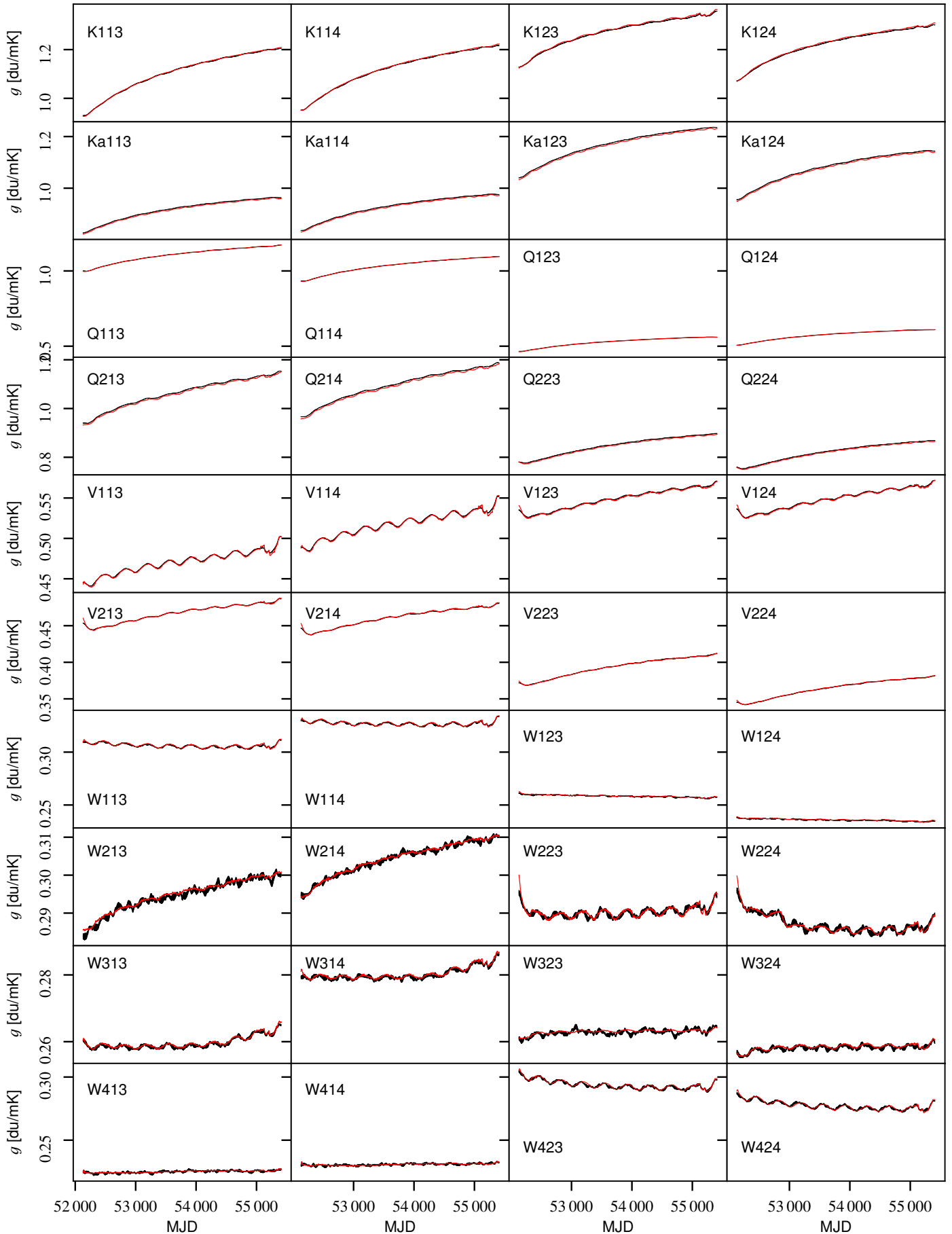


Fig. A.3. Time-variable gain model for each diode for CosMOGLOBE (black) and WMAP9 (red).

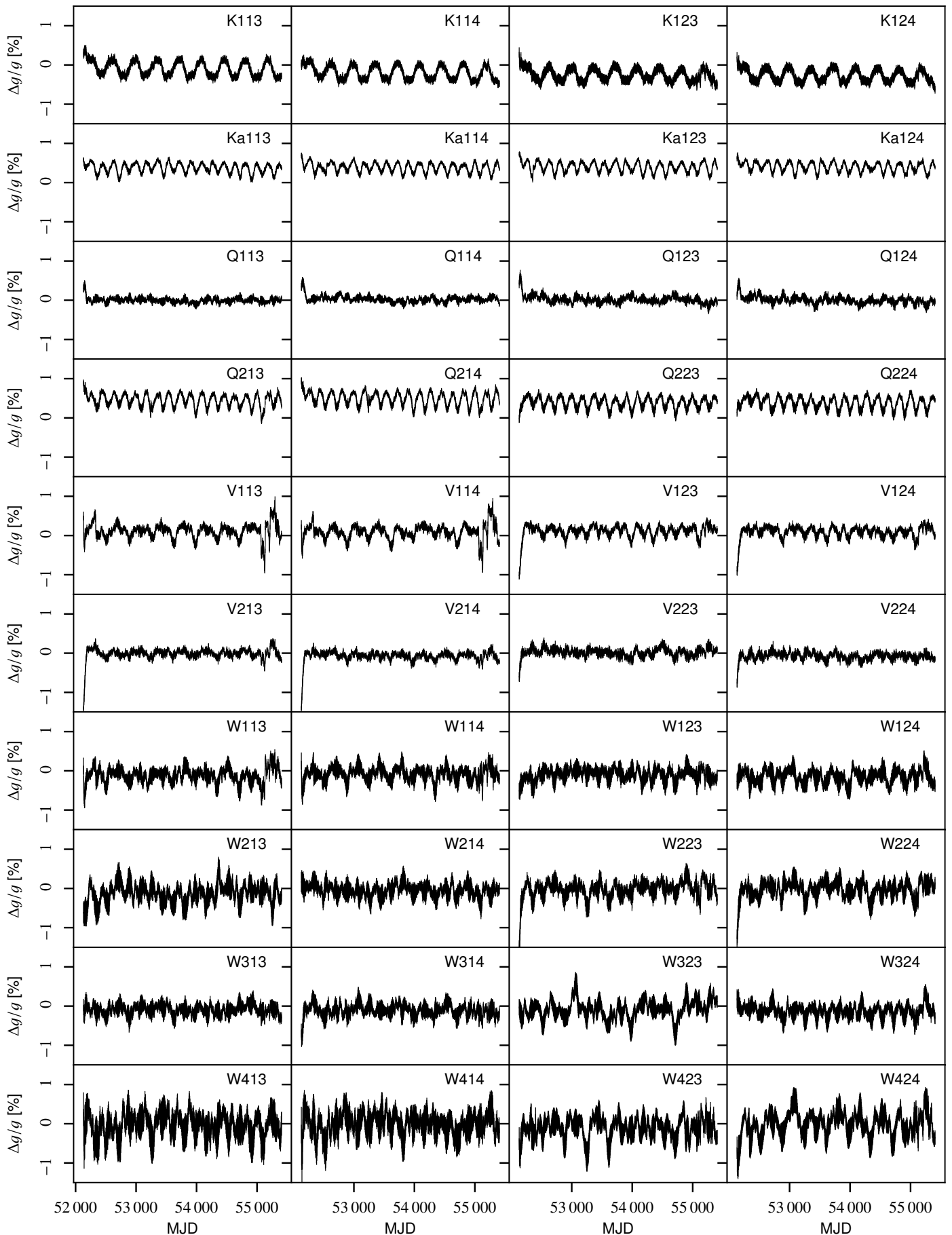


Fig. A.4. Relative gain difference between COSMOGLOBE and WMAP9, $(g^{\text{CG}} - g^{\text{WMAP}})/g^{\text{WMAP}}$.

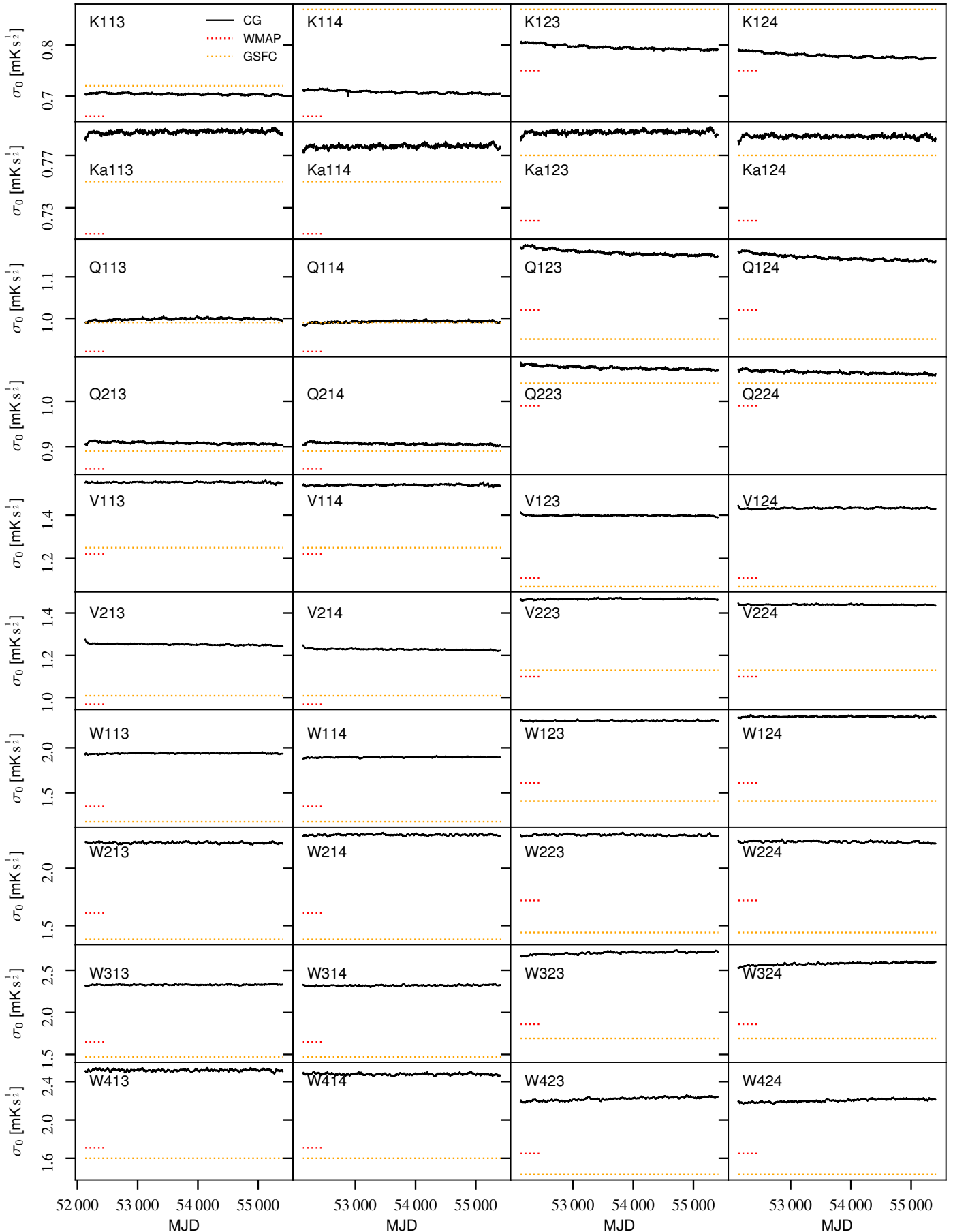


Fig. A.5. White noise rms per TOD sample, σ_0 . Black lines show Cosmoglobe estimates, while dotted orange and red lines show WMAP first-year in-flight and GSFC laboratory measurements.

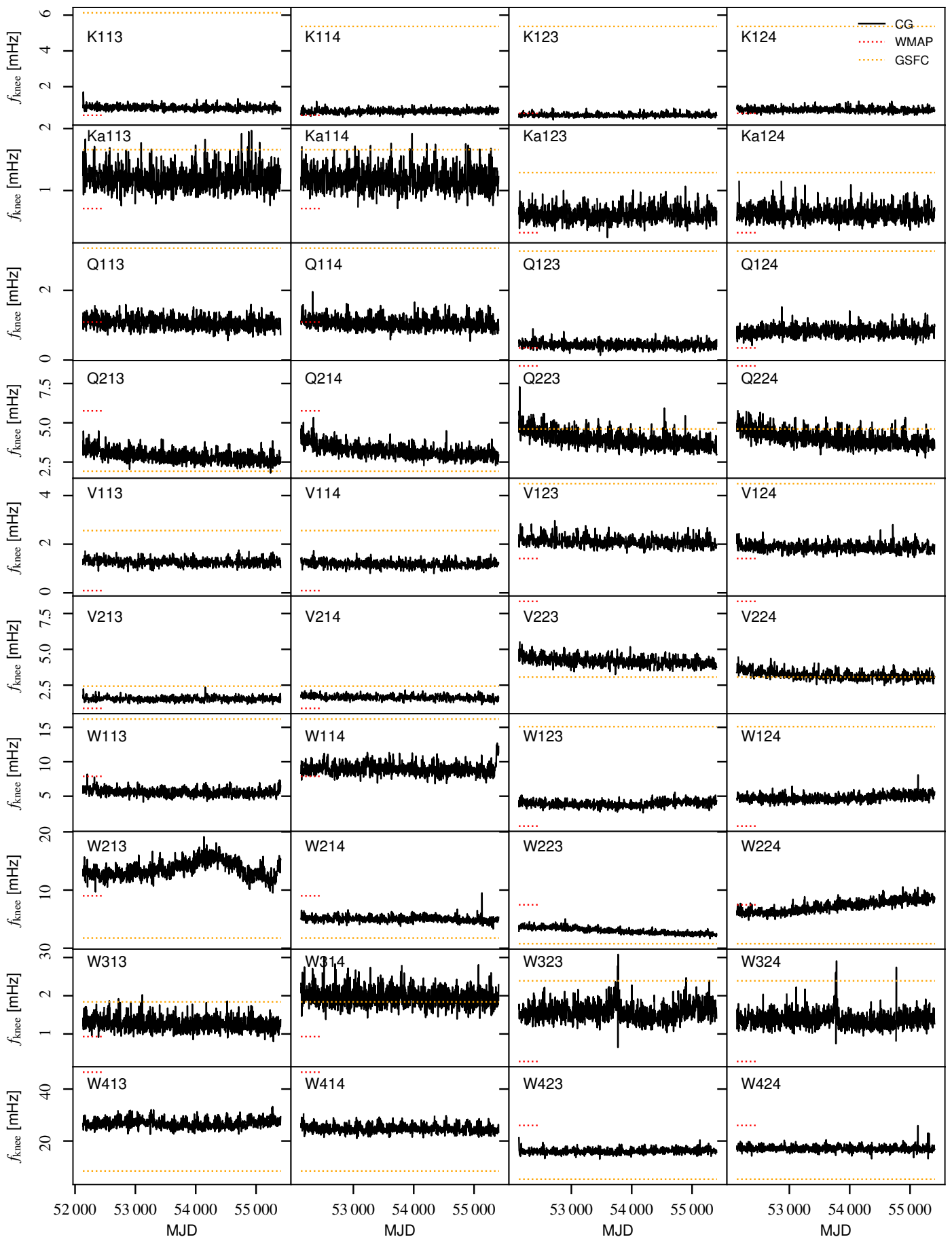


Fig. A.6. Correlated noise knee frequency, f_k , for each diode. Black lines show COSMOGLOBE estimates, while dotted orange and red lines show WMAP first-year in-flight and GSFC laboratory measurements.

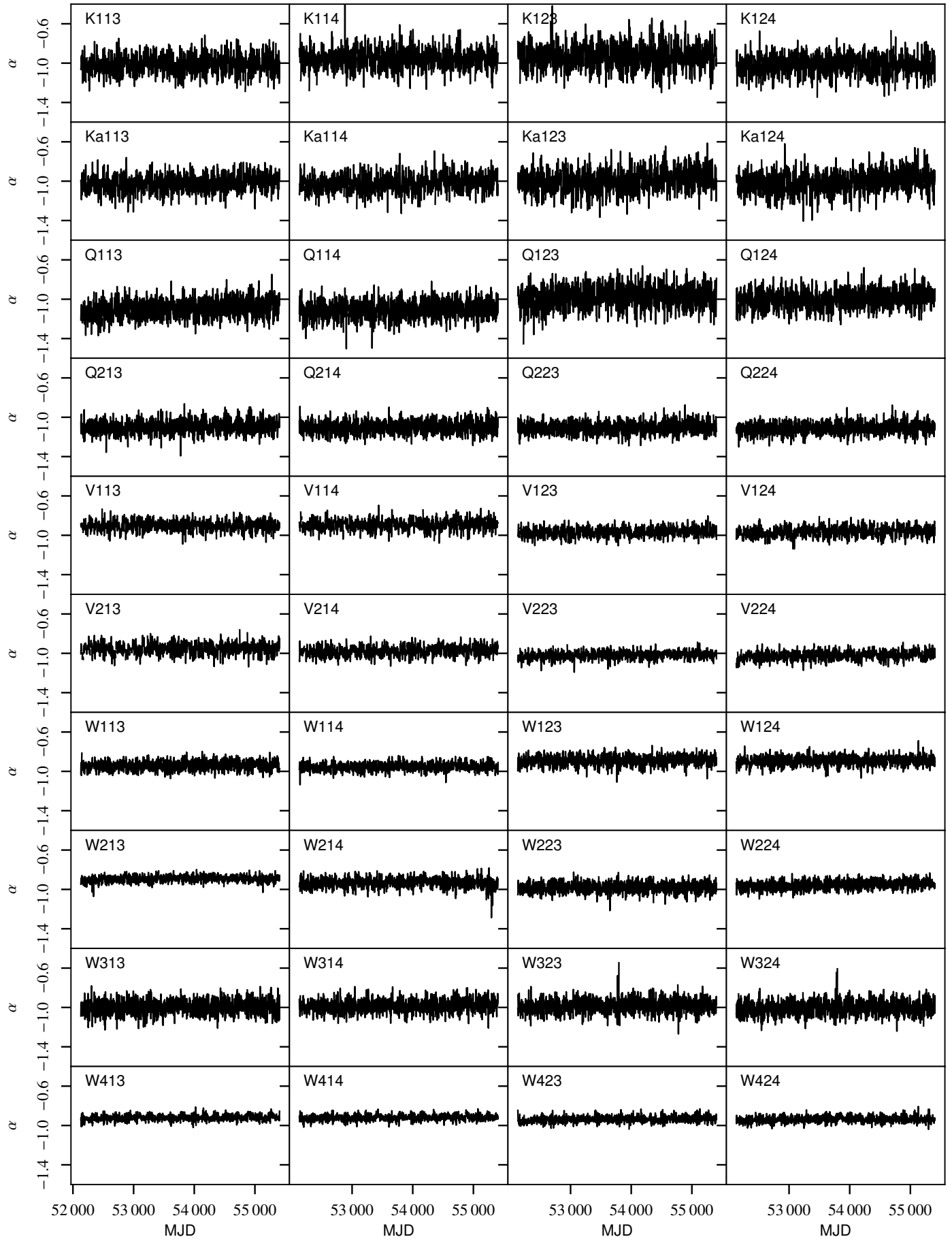


Fig. A.7. Correlated noise slope, α , for each diode. Black lines show COSMOGLOBE estimates, while dotted orange and red lines show WMAP first-year in-flight and GSFC laboratory measurements.

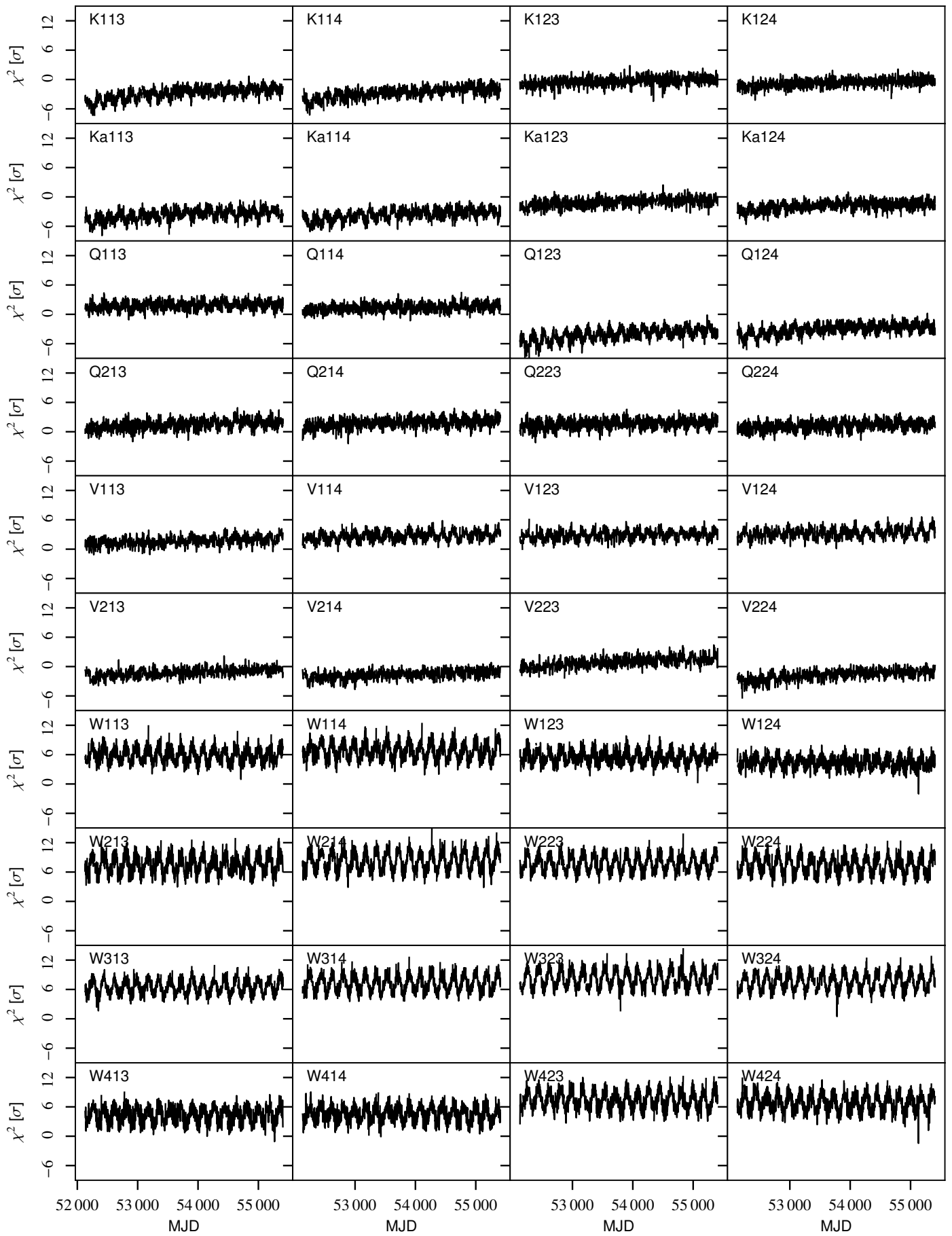


Fig. A.8. TOD-level reduced normalized χ^2 as defined by Eq. (17).

Appendix B: WMAP frequency map survey

In this appendix, we provide a frequency map survey for all ten DAs. Figure B.1 shows the full DA polarization maps as derived both by COSMOGLOBE and *WMAP9*, as well as their differences. Figures B.2 and B.3 shows COSMOGLOBE white noise and posterior rms for each DA and Stokes parameter, as well as the cross-correlation between Stokes Q and U . Figure B.4 shows differences between two Gibbs samples, and Fig. B.5 shows the TOD-level residual, obtained by projecting the TOD residual into a sky map. Finally, Fig. B.6 shows the map-level residual, obtained by subtracting the astrophysical sky model from the corresponding DA map.

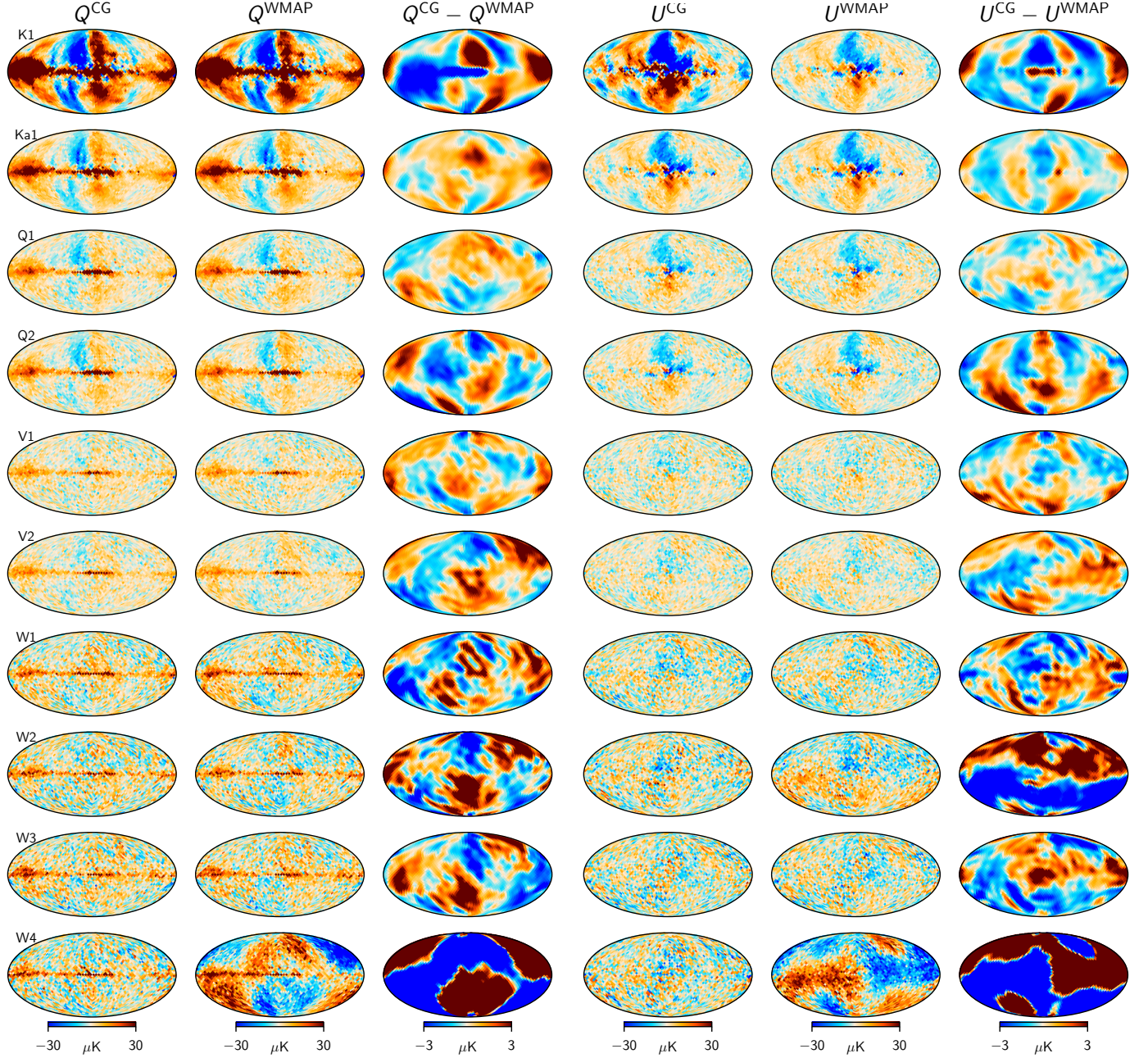


Fig. B.1. Comparison of COSMOGLOBE and *WMAP9* polarization DA maps. Left and right sections show Stokes Q and U , respectively, while rows show DAs. Within each section, the left and middle columns show the COSMOGLOBE and *WMAP9* maps, while the right column shows their difference. All full-signal maps are shown at a HEALPix resolution of $N_{\text{side}} = 16$, and the difference maps have additionally been smoothed with a 10° FWHM beam.

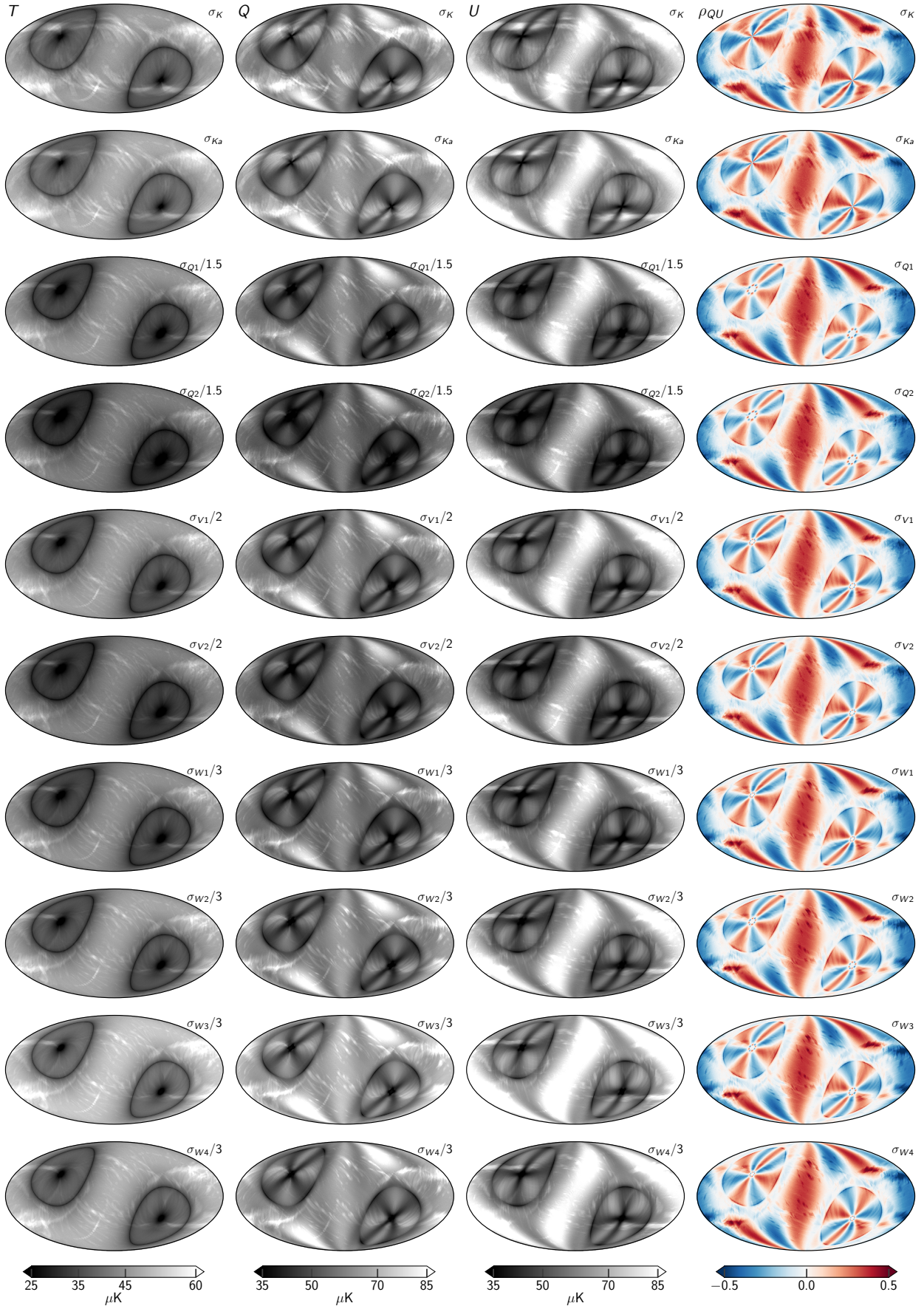


Fig. B.2. COSMOGLOBE white noise rms per pixel, σ_p , for each DA and Stokes parameters. The rightmost column shows the cross-correlation between Stokes Q and U due to the WMAP scanning strategy.

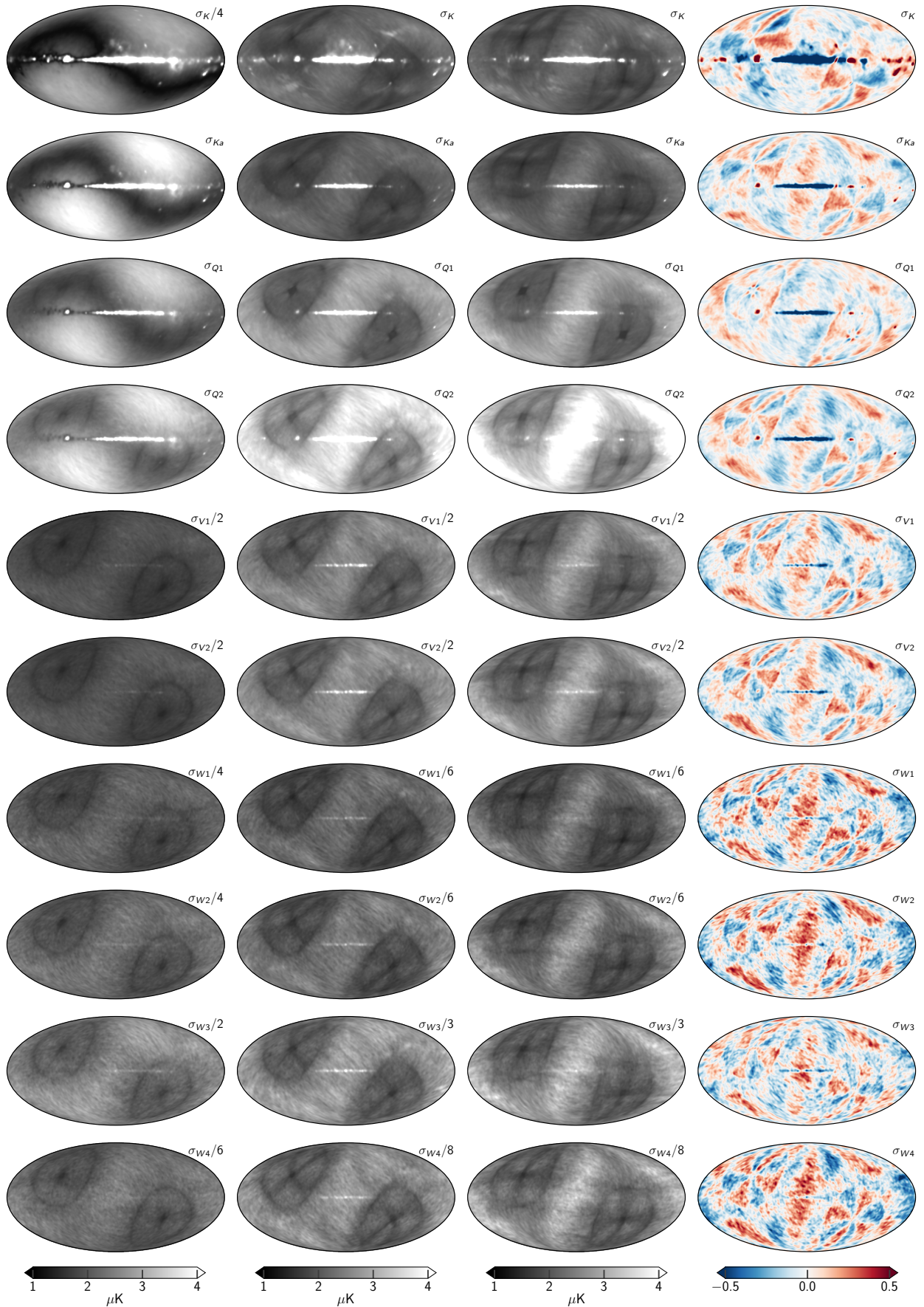
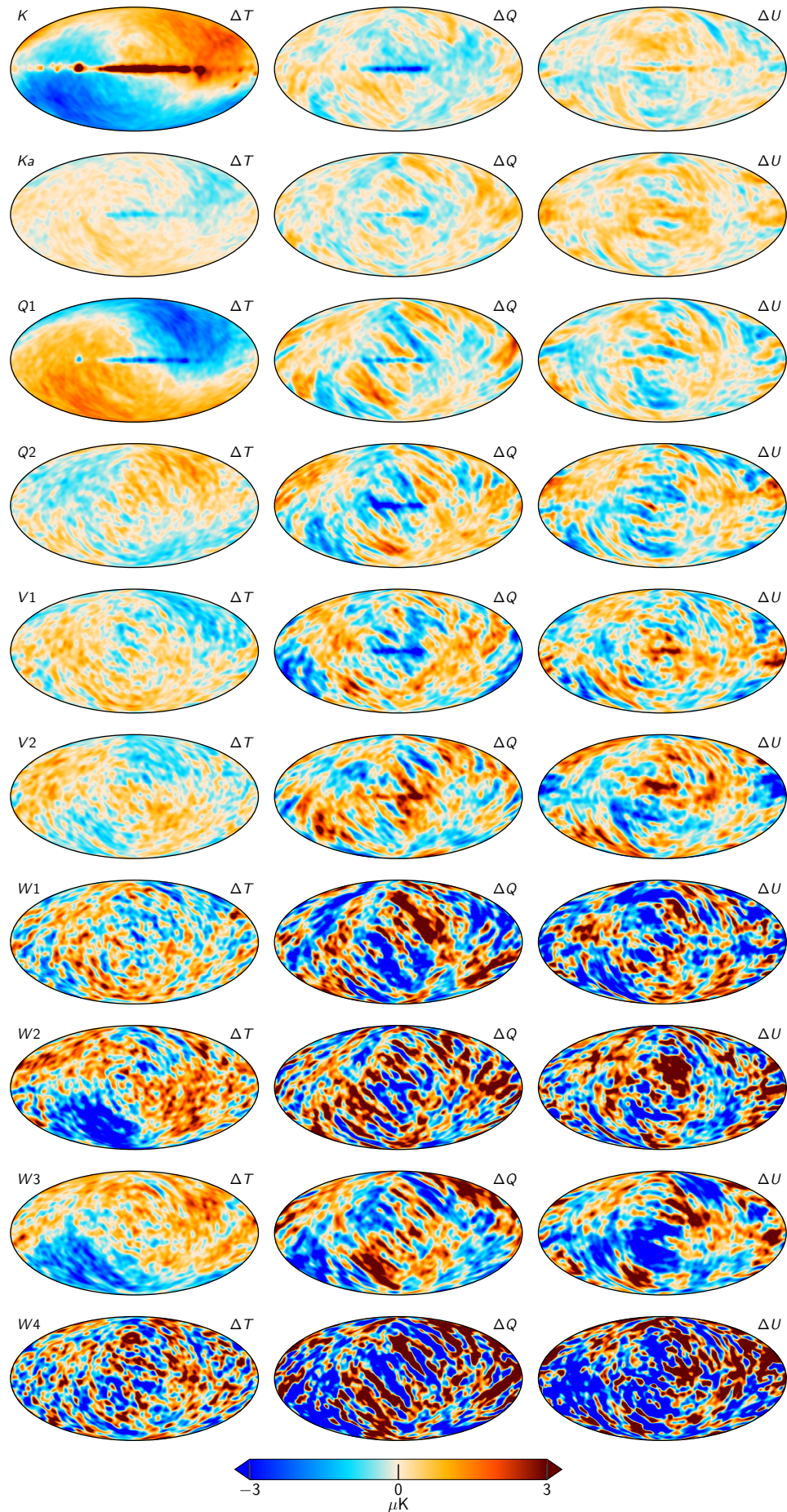


Fig. B.3. COSMOGLOBE posterior standard deviation for each DA and Stokes parameter, evaluated at an angular resolution of X° FWHM. The rightmost column shows the correlation coefficient between Stokes Q and U .

**Fig. B.4.** Differences between two COSMOGLOBE frequency map samples.

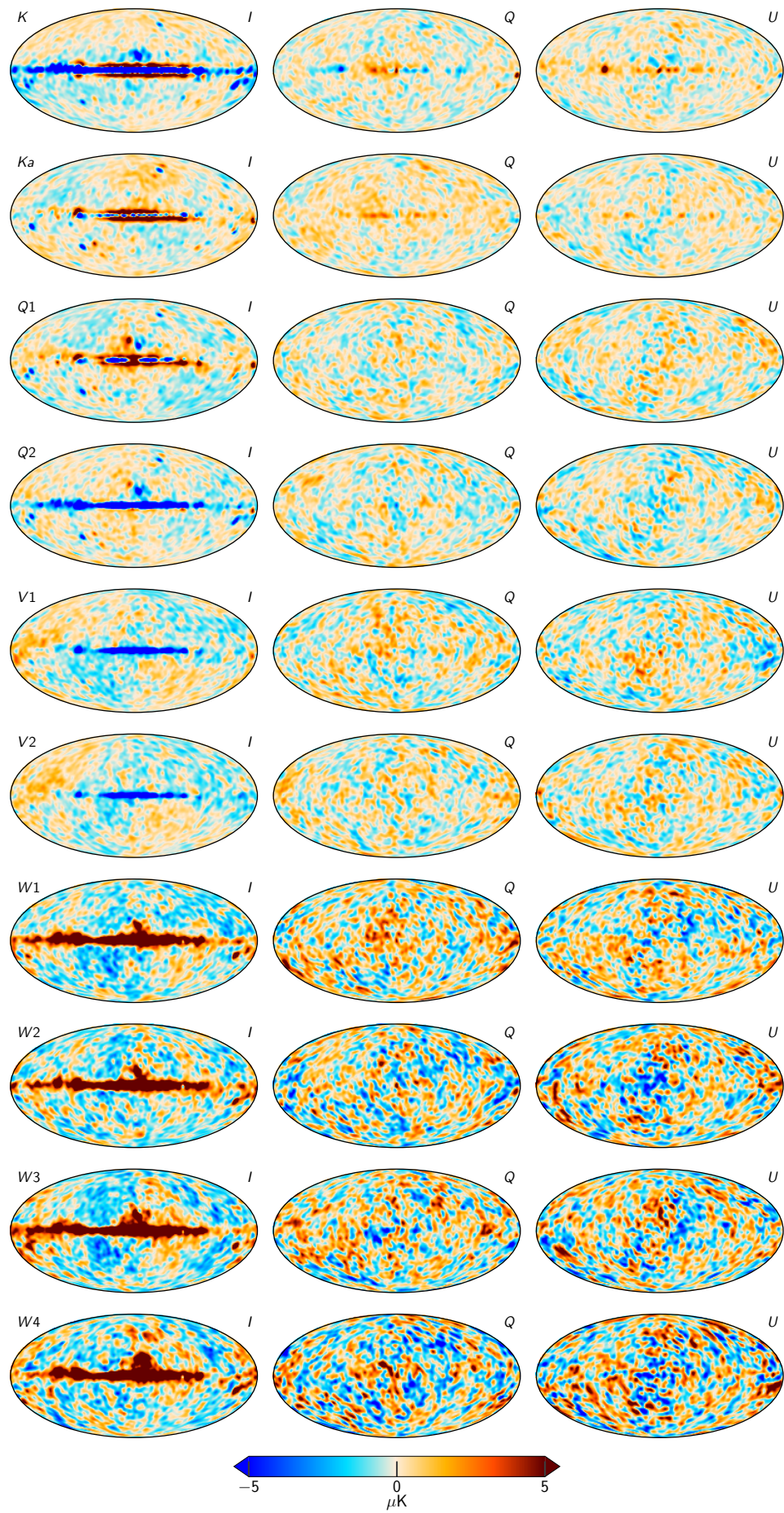
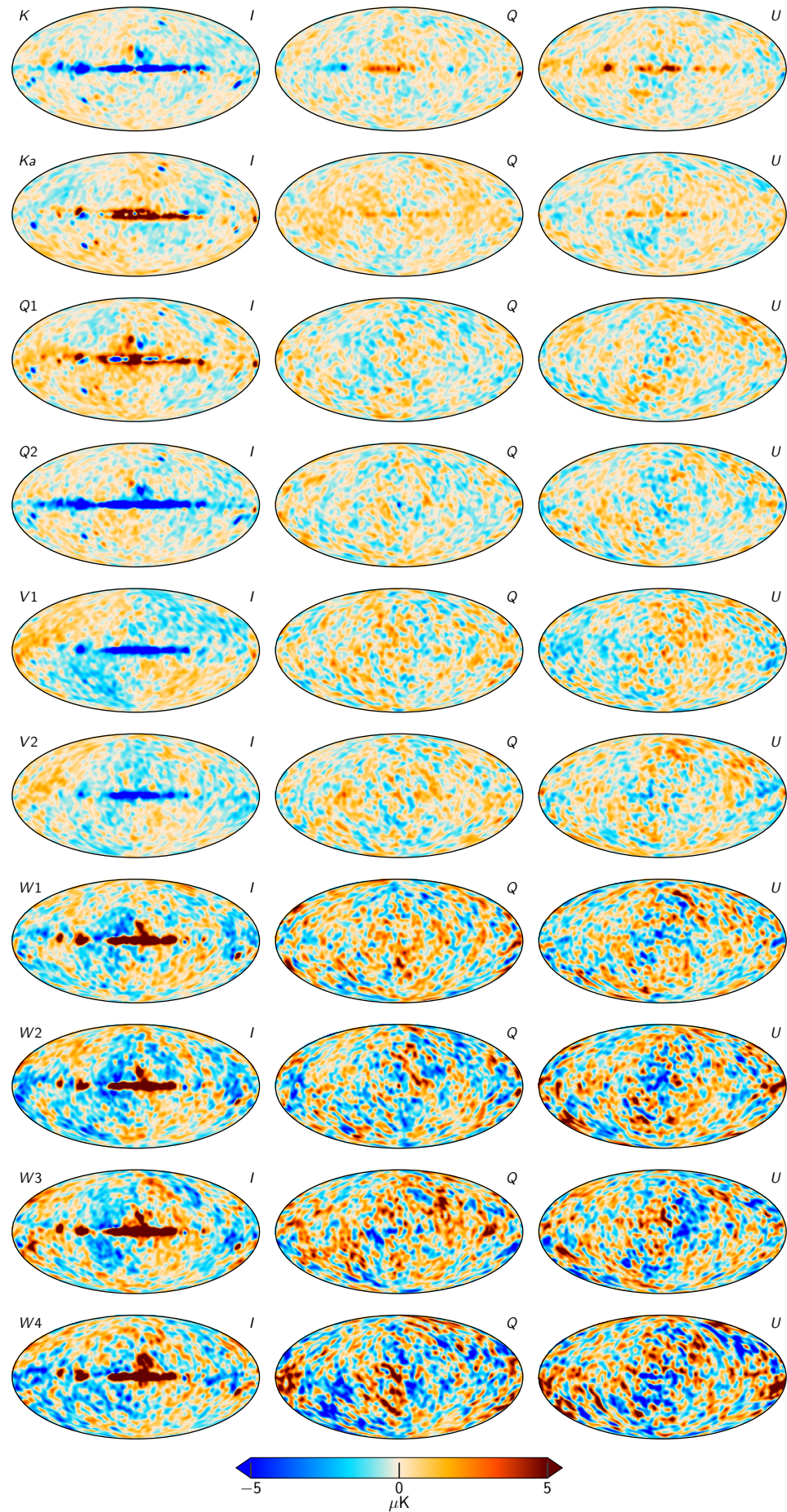


Fig. B.5. TOD-level residual maps for each DA, smoothed with a 5° FWHM Gaussian beam.
Article number, page 58 of 59

**Fig. B.6.** Map-level residual maps for each DA, smoothed by 5° .